The Study of Astrophysical Magnetized Flows

THESIS SUBMITTED TO THE UNIVERSITY OF DELHI
FOR THE DEGREE OF
DOCTOR OF PHILOSOPHY

by

Kuldeep Singh

Aryabhatta Research Institute of observational sciencES (ARIES)
Manora Peak, Nainital - 263002,
Uttarakhand
AND
Department of Physics and Astrophysics
University of Delhi, New Delhi - 110007, India

Under the supervision of
Patrick Das Gupta
AND
co-supervision of
Indranil Chattopadhyay

Department of Physics and Astrophysics
UNIVERSITY OF DELHI
New Delhi

June 2021

Dedicated to my parents...

DECLARATION

I, Kuldeep Singh, declare that this thesis entitled, **'The Study of Astrophysical Magnetized Flows'** is an authentic record of the research carried out by me under the supervision of Prof. Patrick Das Gupta, Phyics and Astrophysics Department, University of Delhi, Delhi and co-supervision of Indranil Chattopadhyay, ARIES, Nainital. I confirm that the work is original and hasn't been submitted for award of any degree in this University or any other Institute. The assistance received from various sources is clearly stated. All the used material from literature is clearly acknowledged at respective places.

Kuldeep Singh
PhD Candidate

Patrick Das Gupta
Supervisor,
University of Delhi, New Delhi 110 007, India

Indranil Chattopadhyay
Co-Supervisor,
ARIES, Nainital, 263002, India

Head, Department of Physics and Astrophysics
University of Delhi, New Delhi 110 007, India

Department of Physics & Astrophysics
University of Delhi
Delhi - 110 007, India

Date : _____

Certificate of Originality

The research work embodied in this thesis entitled "**The Study of Astrophysical Magnetized Flows**" has been carried out by me at the **Department of Physics & Astrophysics**, University of Delhi, New Delhi, India. The manuscript has been subjected to plagiarism check by **Urkund** software. The work submitted for consideration of award of Ph.D. is original.

Kuldeep Singh
Name and signature of the Candidate

Student Approval Form

Name of the Author	*Kuldeep Singh*
Department	*Physics and Astrophysics*
Degree	*Doctor of Philosophy*
University	*University of Delhi, New Delhi, India*
Guide	*Prof. Patrick Das Gupta (Supervisor) & Indranil Chattopadhyay (Co-Supervisor)*
Thesis Title	*The Study of Astrophysical Magnetized Flows*
Year of Award	

Agreement

1. I hereby certify that if appropriate, I have obtained and attached hereto a written permission/statement from the owner(s) of each third party copyrighted matter to be included in my thesis/dissertation, allowing distribution as specified below.
2. I hereby grant to the university and its agents the non-exclusive license to archive and make accessible, under the conditions specified below, my thesis/dissertation, in whole or in part in all forms of media, now or hereafter known. I retain all other ownership rights to the copyright of the thesis/dissertation. I also retain the right to use in future works (such as articles or books) all or part of this thesis, dissertation, or project report.

Conditions:

1. Release the entire work for access worldwide	
2. Release the entire work for 'My University' only for 1 Year 2 Years 3 Years and after this time release the work for access worldwide.	
3. Release the entire work for 'My University' only while at the same time releasing the following parts of the work	

(e.g. because other parts relate to publications) for worldwide access. a) Bibliographic details and Synopsis only b) Bibliographic details, synopsis and the following chapters only. c) Preview/Table of Contents/24 page only.	
4. View Only (No Downloads) (worldwide)	

Signature of the Scholar

Signature and seal of the Guide

Place: _____

Date: _____

PUBLICATIONS

A. In peer reviewed journals

1. *"Study of Magnetized accretion flow with cooling processes"*

   Kuldeep Singh, Indranil Chattopadhyay

   Journal of Astrophysics and Astronomy, 39:10, (2018) [**Impact factor: 0.849**]

2. *"Study of magnetized accretion flow with variable* Γ *equation of state"*

   Kuldeep Singh, Indranil Chattopadhyay

   MNRAS, 476, 4123, (2018); arXiv: 1802.05677 [**Impact factor: 5.231**]

3. *"Effect of composition on magnetized outflows"*

   Kuldeep Singh, Indranil Chattopadhyay

   MNRAS, 486, 3506, (2019); arXiv: 1904.06077 [**Impact factor: 5.231**]

4. *"Study of relativistic magnetized outflows with relativistic equation of state"*

   Kuldeep Singh, Indranil Chattopadhyay

   MNRAS, 488, 5713, (2019); arXiv: 1907.12547 [**Impact factor: 5.231**]

ABSTRACT

A detailed study of magnetized astrophysical flows has been carried out in the magnetohydrodynamic and special relativistic magnetohydrodynamic regime. We have considered the thermodynamics of the flow to be described with a fixed as well as, a variable adiabatic index equation of state (EoS). As examples of MHD flow, we have studied (i) funnel accretion onto neutron stars and white dwarfs, (ii) magnetized equatorial outflows from around a compact magnetized star, and (iii) magnetized relativistic outflows about the axis of symmetry from compact objects like black holes.

Possibly for the first time, we obtained semi-analytical magnetized accretion solutions onto compact objects with a hard surfaces such as neutron stars which satisfies the inner boundary condition, where the accreting matter gently settles onto the surface of the star. We also compared these solutions in Newtonian & pseudo-Newtonian regime. We assumed that neutron star has a strong dipole magnetic field whose dipole moment is aligned along the rotation axis of the star. We have included cooling processes like bremsstrahlung and cyclotron. Depending on the Bernoulli parameter of the flow and the rotation period of the star, we obtain various solutions which may possess a single sonic point or multiple sonic points. We have also studied the dependence of accretion solutions on plasma compositions. All types of accretion solutions undergo a very strong primary shock which forms near the star surface. The strength of the primary shock increases with the rotation period of the star, but the

shock location is weakly dependent on the period. Due to the presence of multiple sonic points, we can find a secondary shock within a very small region of the parameter space but this shock is weak and the shock location, the shock strength, and the compression ratio depends significantly on the rotation period of the star and the total energy of the flow. We also calculate the total luminosity of the magnetized accretion solution which is in good agreement with observations. We have also studied a case of white dwarf where our results match with the observations. We have found that cyclotron cooling and bremsstrahlung cooling are necessary to obtain a consistent accretion solution *i.e.,* a solution which connects the flow from the accretion disk to the star surface.

We studied the effect of plasma composition on the equatorial wind outflow with variable adiabatic index EoS. We have found that terminal velocity depends upon the plasma composition. Lepton dominated winds with higher values of Bernoulli parameter have high terminal speeds. We have also studied solutions for different energies, angular momenta and in different gravity *i.e.,* Newtonian & pseudo-Newtonian potential. For the same values of the Bernoulli parameter (energy) and the total angular momentum, a wind in strong gravity is more accelerated, compared to wind in Newtonian gravity. We showed that flow variables like the radial, azimuthal velocity components, temperature, etc all depend on the composition of the flow.

We continue our outflow study in case of collimated outflows or jets in special relativistic magnetohydrodynamic regime with variable adiabatic index EoS. We found that plasma composition mainly

affects the velocity and the temperature of the jet but the collimation of jet and fast critical point location appears to have no dependence on plasma composition. We explore all outflow solutions and found that the solution depends on the current distribution parameter, the magnetization parameter, the inclination angle of field lines with respect to the disk plane, and Alfvèn point radius. Fast point location can be related to collimation shock location because the super-fast flow is causally disconnected from the flow which is behind.

ACKNOWLEDGEMENT

I would like to sincerely thank Prof. Patrick Das Gupta who is a very humble human being and always been there to support me and help me to get through official and non-official challenges confronted during PhD. I would like to express my sincere gratitude to Dr. Indranil Chattopadhyay for providing me an opportunity to work on his visionary perspectives. I deeply appreciate his valuable scientific discussions, remarks and exhortation. I am particularly influenced by his motivating attitude and immense knowledge. I am also thankful to all the scientists at ARIES for always supporting me. I dedicate this thesis to my family for their overwhelming care and support throughout my life.

I would like to thank Shilpa, Pankaj and Gautam for their succour, encouragements, and aid to conquer the difficult circumstances. I also thank Raj, Mukesh and Rajiv for immensely fruitful discussions. I would like to express my deep appreciation towards Arti, Sunil and Ram for helping me to go through official procedures involved during thesis submission. I also thank administration department of ARIES and the University of Delhi for supportive approach.

Finally, I acknowledge the financial support provided by the Department of Science and Technology (DST), New Delhi, India.

– Kuldeep Singh

Contents

Abbreviations

AGN	**A**ctive **G**alactic **N**ucleus
BH	**B**lack **H**ole
CR EoS	**C**hattopadhyay & **R**yu **E**quation **o**f **S**tate
EoM	**E**quations **o**f **M**otion
EoS	**E**quation **o**f **S**tate
Eq	**E**quation
GRB	**G**amma-**R**ay **B**urst
HD	**H**ydro-**D**ynamic
ISM	**I**nter-**S**tellar **M**edium
IGM	**I**nter-**G**alactic **M**edium
L.H.S	**L**eft **H**and **S**ide
MCP	**M**ultiple-**C**ritical-**P**oints
MHD	**M**agneto-**H**ydro-**D**ynamic
NP	**N**ewtonian **P**otential
NS	**N**eutron **S**tar
PWP	**P**aczyński-**W**iita **P**otential
R.H.S	**R**eft **H**and **S**ide
SMHD	**S**pecial-**R**elativistic **M**agneto-**H**ydro-**D**ynamic
WD	**W**hite **D**warf
XRB	**X**-**R**ay **B**inary
YSO	**Y**oung-**S**tellar **O**bject

Symbols

G	Gravitational constant
c	Speed of light
κ_{B}	Boltzmann constant
m_{e^-}	Mass of electron
m_{p^+}	Mass of proton
p	Isotropic gas pressure
ρ	Mass density
c_{S}	Sound speed
h	Specific enthalpy
$\bar{e}$	Energy density
T	Temperature
Θ	Dimensionless temperature ($\equiv \kappa_{\mathrm{B}} T / m_{\mathrm{e}^-} c^2$)
n	Number density
n_{e^-}	Number density of electron
n_{p^+}	Number density of proton
ξ	Composition parameter ($\equiv n_{\mathrm{e}^-} / n_{\mathrm{p}^+}$)
η	Electron to proton mass ratio ($\equiv m_{\mathrm{e}^-} / m_{\mathrm{p}^+}$)
Γ	Adiabatic index
N	Polytropic index
E	Total energy
$\mathcal{B}$	Bernoulli parameter
L	Total angular momentum
Ω	Angular velocity
P	Rotation period of star
v_{p}	Polodial velocity
v_ϕ	Azimuthal velocity
r	Radial distance
r_{c}	Critical point radius

$r_{\rm co}$	Co-rotation radius ($\equiv (GM_\circ/\Omega^2)^{1/3}$)
$r_{\rm sh}$	Shock location
$r_{\rm g}$	Schwarzschild radius ($\equiv 2GM_*/c^2$)
$B_{\rm p}$	Polodial magnetic field
B_ϕ	Azimuthal magnetic field
$A_{\rm p}$	Polodial area
Φ	Gravitational potential
$\Phi_{\rm NP}$	Newtonian potential ($\equiv -GM_*/r$)
$\Phi_{\rm PWP}$	Paczyński & Wiita ($\equiv -GM_*/(r-r_{\rm g})$)
Q	Cooling
$\mathcal{L}$	Luminosity

Chapter 1

Introduction

1.1 Overview

Astronomical observations have shown that space is filled with plasma *e.g.,* interstellar medium (ISM), intergalactic medium (IGM), etc. Stellar winds, accretion discs, and jets are also in plasma form. Space is also filled with magnetic fields. Astrophysical objects have magnetic field in a very broad range like the average surface magnetic field of the sun of values, ~ 1G (Babcock, 1963), the region near a black hole $\sim 10^{4-6}$G (Rothstein & Lovelace, 2008; Daly, 2019), white dwarf has surface magnetic field $\sim 10^{6-8}$G (Schmidt *et al.*, 2003; Ferrario & Wickramasinghe, 2005) while for neutron star it is as high as $\sim 10^{8-12}$G (Pan *et al.*, 2013). ISM has magnetic field $\sim 1\mu$G $-$ 100μG (Beck, 2009), and IGM has very weak magnetic field, minimum estimated is $\sim 10^{-18}$G (Arlen *et al.*, 2014; Dermer *et al.*, 2011). Hence, we can conclude that plasma is embedded in magnetic field of astrophysical objects. If the magnetic energy density is high or comparable to matter energy density, then magnetic field significantly affects the plasma dynamics. It has been observationally seen that large scale magnetic field not only provides energy and momentum to the flow but also guides or collimates the flow. To study the dynamics of astrophysical flows (stellar wind, jet, and accretion) around a compact object, it is important to include the effects of the magnetic field.

In this thesis, (1) we study the physics of magnetized plasma in accretion flow onto neutron star and white dwarf, (2) equatorial outflows from near a magnetized compact star, and (3) collimated magnetized outflow as a model for astrophysical jets. In all these scenarios, the temperature varies by few orders of magnitude, such that the fixed adiabatic index equation of state is untenable. So we use the relativistic equation of state for the fluid.

We employ magnetohydrodynamic (MHD) equations of motion to study accretion and outflows around compact objects. However, these objects present a different set of challenges. For accretion flow which channels onto the neutron star or white dwarf, the challenge is to obtain a correct solution from the inner region of the accretion disc onto the star's surface, such that the matter gently settles onto it. While for equatorial outflows along open field lines, the solution has to pass through all the available critical points. For collimated outflows about the axis of symmetry or jets, the challenge is not only to obtain a solution passing through all the critical points but also to solve the transfield equation in order to obtain the streamline.

In this thesis, we have addressed these issues in detail and in a more self-consistent manner. We have also studied the effect of various types of equations of state and composition of the plasma on the solution.

1.2 Theoretical Developments in Astrophysical Flows

We will first discuss the general theoretical development in magnetohydrodynamics (MHDs), then later we will chronologically proceed with the development in hydrodynamic (HD) and MHD regime of wind/outflow/jet and accretion models.

The first study of ideal and non-ideal axisymmetric MHD flow was carried out by Chandrasekhar (1956). The flow was assumed to be incompressible and inviscid. Assuming the same type of flow, Heinemann & Olbert (1978) focused only on ideal axisymmetric steady MHD regime and showed that magnetic stream function has second-order quasi-linear partial differential equation. Tsinganos (1981, 1982) studied magnetohydrodynamic equilibrium and the conservation laws in detail for axisymmetric MHD steady flow and general magnetic field distribution. Further, Mobarry & Lovelace (1986) studied the conservation laws for axisymmetric general relativistic magnetohydrodynamic (GRMHD) steady flow in Schwarzschild geometry.

Below we will discuss in brief the theoretical developments in case of wind, accretion, and jet respectively:

- **Accretion**: It is a process in which a massive object gravitationally attracts the surrounding matter. In 1952, Bondi gave the first accretion model for spherical flows onto a central object in the hydrodynamic regime and his model also had solution for outflows (*e.g.,* winds). However, it was realised that matter accreted should have some angular momentum. Thus, instead of matter getting accreted

spherically it should form a disc around the central object. Viscosity helped in removing angular momentum outwards thus allowing the matter to reach the inner boundary (Shakura & Sunyaev, 1973; Novikov & Thorne, 1973). These discs could explain the observed luminosities of X-ray binaries. Unlike for spherical accretion where matter being radially falling cannot radiate efficiently. In addition, viscous dissipation causes heating. It was assumed in these models that the viscous heating is efficiently radiated away which gives rise to multiple black body spectrum from accretion disc. However, there is a possibility that some viscous heat might get advected inward during the accretion process which led to the development of the model of advection-dominated accretion flows (ADAF) (Abramowicz *et al.*, 1988; Narayan *et al.*, 1997). But all the accretion disc models discussed above neglected transonicity. Matter far away is subsonic and near the compact object is supersonic. So accretion flows should pass a sonic point, therefore transonic solutions are the physical solutions for accretion flows (Novikov & Thorne, 1973). In 1980, Liang & Thompson gave transonic solution for thin accretion disc in general-relativistic regime and studied the applications for black hole. Later, Fukue (1987) studied the transonic solutions and shock transitions for accretion disc in case of compact objects and Chakrabarti (1989) also studied shocks and multiplicity of shocks in case of black hole accretion and winds. Transonic solutions for black hole accretion highly depend on the composition of the flow (Chattopadhyay & Chakrabarti, 2011) and dissipation processes *e.g.,* viscosity and cooling (Kumar & Chattopadhyay, 2014).

The above mentioned model works well if the accreting object is a black hole or a star having weak magnetic field. However, for a magnetized star which has strong magnetic field, like neutron star or white dwarf, accretion occurs in the form of a disc up to a certain radius, where gas pressure and matter energy density is balanced by magnetic energy density, after which the accretion process is controlled by star's magnetic field and the matter is channelled through the magnetic field lines onto the star's surface. This is known as magnetized accretion flow or funnel flow. Pringle *et al.* (1972); Lamb *et al.* (1973) and Ghosh & Lamb (1977, 1979) studied these kind of flows and investigated the transition region which forms near the inner edge of the accretion disc. Later, Lovelace *et al.* (1986) presented steady state, axisymmetric MHD equations of motion to study flows around magnetized stars which have dipole like magnetic fields. Camenzind (1990) and Paatz

et al. (1996) tried to explain accretion and outflows in case of YSOs and T-Tauri stars with MHD theory.

During magnetized accretion, the gravity of the star increases the flow velocity of the matter. Such that when this fast moving matter hits the star's surface it forms a shock. Energy of the shock is radiated away through cooling processes and matter gently settles down onto the star's surface (Li *et al.*, 1996). Some attempts were made to explain magnetized accretion flow onto neutron star by considering dipole like magnetic field (Li *et al.*, 1999). The strong magnetic field of the neutron star also simplifies the MHD equations for funnel flow (Koldoba *et al.*, 2002) and hence analysis of shocks (Karino & Kino, 2008).

- **Wind**: Stellar wind and disc wind is composed of plasma which is blown out due to either thermal gradient force, centrifugal force (due to rotation), radiation force, and magnetic force. The first hydrodynamic spherical wind model was given by Parker (1958) applied this model for solar winds. He showed that the solar wind is just expanding corona. This model was limited because the magnetic field was ignored but it gave us a basic understanding of stellar winds. However, along with thermal force and centrifugal force, magnetic force also affects the dynamics of stellar wind or wind from accretion discs. So, even if the corona temperature is low, magnetically controlled centrifugal forces can drive stellar winds (Mestel, 1967, 1968), in case of AGNs and rapidly rotating compact objects (Camenzind, 1986a,b). A self-consistent MHD stellar wind model was given by Weber & Davis in 1967. They predicted the correct solar wind speed at the earth's orbit, and showed that magnetic field not only accelerates the wind but also carries away or removes the angular momentum from the star. If there is an outflow from a star or accretion disc along open magnetic field lines away from the equatorial plane then magnetic hoop stress can collimate the flow along the rotation axis of the star or accretion disc (Sakurai, 1985, 1987). Therefore, some part of the non-equatorial wind collimates producing outflows.

  Winds from compact objects can be thermally relativistic (due to strong gravity) at the base, which then drive the wind to relativistic velocities. Temperatures, hence, vary from relativistic to non-relativistic regime. This means that the effective adiabatic index of the system does not remain constant (in HD regime Meliani *et al.*, 2004). WD model (in MHD regime Weber & Davis, 1967) assumed

fixed adiabatic index. It could be extended by using variable adiabatic index equation of state (EoS) to properly study equatorial outflows in strong gravity.

- **Jet**: It is a 'collimated' outflow along the rotation axis of the central object or accretion disc. If it has high speed close to the speed of light then it is known as a relativistic jet.

  Generally, BHs are known as super eaters, they consume the matter which ventures too close to them. However, it is possible to extract energy and angular momentum from BH if strong magnetic field (due to currents flowing in accretion disc) is threading a highly rotating BH. Then electric field can be produced and high strength of the magnetic field can produce electron-positron pairs (Blandford & Znajek, 1977). These pairs are then accelerated along the rotation axis and produce particle jets. But jets have also been seen to originate from regions around YSOs, neutron stars and slowly rotating BHs. Thus, they could be launched from accretion discs, where energy and angular momentum can be extracted from the disc itself. Matter is pushed (due to thermal gradient, radiation pressure, or centrifugal force) along the open magnetic field lines from the accretion disc where the magnetic field collimates the flow and carries it to higher heights. If jets are launched from the accretion disc, then naturally it would have structure like an onion because different radii of accretion disc will have different temperatures and angular velocities. Therefore, it is possible to study jets with self-similar assumption. In 1982, Blandford & Payne gave the first MHD jet model with the assumption of cold flows and studied self-similar solutions of jet from the accretion disc. We know that jets have relativistic speeds $e.g.,$ Lorentz factor ~ 10 in AGNs and ~ 100 in GRBs, so Li *et al.* (1992) extended the Blandford & Payne (1982) model of cold outflows to special relativistic magnetohydrodynamic (SMHD) cold flow. These models ignored the thermal energy because at large heights thermal energy becomes negligible (due to the expansion of jet) but it will be significant near the accretion disc. In 2003, Vlahakis *et al.* (2003a,b) studied the jet solution from sub-Alvénic (near accretion disc when the flow velocity is less than local Alfvén wave speed) to super-Alfvénic (far from accretion disc when the flow velocity is greater than local Alfvén wave speed) regime by considering the thermal terms with fixed adiabatic index ($\Gamma = 4/3$) EoS. Polko *et al.* (2010) used Vlahakis *et al.* (2003a) model with adiabatic index, $\Gamma = 5/3$ and different

current distribution. They showed that the flow can be trans-Alfvénic and trans-fast (far from accretion disc when flow velocity is greater than local fast wave speed). Therefore, the thermodynamics of plasma is very important and also the methodology in which we handle it.

In most of the above mentioned studies of astrophysical flows, fixed adiabatic EoS has been used. However, as we know that there is almost two to four orders of magnitude change in temperature distribution in accretion, winds or jets, especially when the central object is compact. So it is essential to use an EoS which has temperature dependent adiabatic index. Also, the composition of the flow is important. Since for a flow to be thermally relativistic $\kappa_{\rm B}T_i > m_ic^2$ and to be non-relativistic $\kappa_{\rm B}T_i < m_ic^2$. Not only temperature but also composition matters. There is a relativistic perfect EoS which was given by Chandrasekhar (1938), but it has Bessel functions of the second kind which are difficult to handle in the computational domain. Another approximate but accurate EoS for multi-species flow was given by Chattopadhyay & Ryu (2009) (also known as CR EoS) which has temperature dependent adiabatic index and a composition parameter which controls proton-electron-positron proportions in plasma. To avoid the complications of general relativity but still take into account the effect of strong gravity, Paczyński & Wiita (1980) proposed a pseudo-Newtonian potential which although simple, mimics the effects of the Schwarzschild metric.

1.3 Motivation

In hydrodynamics (HDs), there is one signal speed which is the sound speed. Therefore, HD spherical accretion or outflow has one critical point (also called as sonic point in HDs due to sound speed). A critical point is, where the flow velocity is equal to the local sound speed and velocity slope attains a $0/0$ form (which can be solved using L'Hospital's rule). When a flow has angular momentum then there is a possibility of formation of multiple critical points (maximum three in HD flows).

However, in case of magnetized plasma we have an entirely different story, there are three signal speeds which are the slow, Alfvén, and fast speed. Therefore, in these kinds of flows, we have multiple kinds of critical points (maximum five, we will see in Chapter 4), *e.g.,* slow critical point (flow velocity is equal to local slow wave speed), Aflvén point (flow velocity is equal to local Alfvén wave speed), and fast point (flow velocity is equal to local fast wave speed). Thus, a transonic solution for magnetized flow can pass through

one or multiple critical points and hence there is a possibility of formation of 'multiple shocks of different kinds'. But multiple critical points increase the complexity to solve MHD equations. Another point is, as we have mentioned in section 1.1, magnetic field affects the dynamics of magnetized flow but magnetized flow also affects the magnetic field. Therefore in MHD, while solving equations of motion for matter, we need also to solve Maxwell's equations to calculate field configuration (we will see in Chapter 2).

In this thesis, our main motivation is to study the effects of magnetic field on the dynamics of magnetized flows, and thermodynamics of magnetized flows *i.e.,* effect of different EoS and plasma composition.

We start with the problem of magnetized accretion flow or funnel flow onto neutron star and white dwarf. Funnel flow starts from the inner radius of the accretion disc, then follows the magnetic field lines because the strong magnetic field of the star does not allow the matter to go spirally inwards in the form of a disc onto the star's surface. There are many studies available in the literature, but most of them have studied funnel flow from just above the shock surface. They also assumed pre-shock flow velocity to be equal to free-fall and studied emission-line shapes (Hartmann *et al.*, 1994; Muzeroll, Calvet, & Hartmann, 2001). In 2002, Koldoba *et al.* studied magnetized accretion flow onto neutron star by solving MHD equations assuming strong magnetic field, and using the Newtonian potential for neutron star. Their results showed that flow velocity is very high near the star's surface. Another problem is that due to Newtonian potential a maximum of two critical points were possible. So only α-type solutions (a solution which passes through the outer critical point) existed. These solutions are not global solutions, only for a small parameter (energy, rotation period, etc) range these solutions reached the star's surface. Further, Karino & Kino (2008) extended Koldoba's model to study shocks. Their solution successfully matched the surface conditions (*i.e.,* negligible velocity near the star's surface) but the shock location was very far away from the star which contradicts observations (Rana *et al.*, 2005). In 1996, Li *et al.* suggested that the star's gravity can make the flow super-sonic and when the flow hits the star's surface with super-sonic speed, a shock will form and matter slows down to a negligible velocity through dissipation processes. Neutron stars are compact objects and have radius $\sim 1.0 \times 10^6$cm. So it is necessary to consider a strong gravity potential (pseudo-Newtonian potential Paczyński & Wiita, 1980) and variable adiabatic index EoS (because temperature changes two to four orders of magnitude due to shock and cooling processes) while studying flows onto compact objects. In this thesis, we

dedicate a part of the study to magnetized accretion flows onto neutron stars and white dwarfs by considering these important aspects.

Next is equatorial wind outflow from compact object. Winds can be blown out from the inner region of the accretion disc or from near the compact star which is surrounded by matter in the form of a ring. In this study we relaxed the strong magnetic field assumption *i.e.,* the field is self-consistently calculated throughout the solution. The flow is assumed to be in the equatorial plane. We study the effect of plasma composition on wind outflows from compact object. For this, we adopt the Weber & Davis (1967) model which is well tested for equatorial stellar winds (discussed in 1.2). Near the compact object, the temperature is very high and gravity is very strong, so we use CR EoS (Chattopadhyay & Ryu, 2009) and pseudo-Newtonian potential (Paczyński & Wiita, 1980). We study the effect of plasma composition on flow velocity and other flow variables of wind.

Moving onto a different scenario, collimated outflows/jets is a process in which outflow of matter is along the rotation axis of accreting central object. These jets are highly collimated, move with very high speeds ($0.001c$ to $\sim c$) and span over a large distance (pc-Mpc scale). There are many observational evidences of accreting black holes, YSOs, X-ray binaries and AGNs having jets (Reipurth & Bally, 2001; Mirabel & Rodriguez, 1999, 2003; Pringle, 1993) and there are also evidences for magnetic field in jets (Wardle & Homan, 2001; Homan, Attridge & Wardle, 2001; Livo, 2001; Pudritz, Hardcastle, & Gabuzda, 2012; Zamaninasab *et al.*, 2013). Scientists proposed that magnetic field collimates the outflow and accelerates it to relativistic velocities (de Gouveia Dal Pino, 2005). Vlahakis *et al.* (2003a,b) studied collimated outflows in SMHD. They could only obtain trans-Alfvén solutions since adiabatic index was fixed to $4/3$. Later, Polko *et al.* (2010) used Vlahakis *et al.* (2003a) model with fixed adiabatic index ($\Gamma = 5/3$) equation of state and different current distribution. They showed that the flow can become trans-Alfvénic (sub Alfvénic to super Alfvénic) and trans-fast (sub fast to super fast). Therefore, the thermodynamics of the flow may play an important role in determining the nature of the solution. In particular, outflow is hot near the base but the temperature decreases by few orders of magnitude at large distances, therefore the adiabatic index is not likely to remain constant throughout the flow. We study the collimation and composition of outflows/jets in case of compact objects using Vlahakis *et al.* (2003a); Polko *et al.* (2010) models but with the relativistic equation of state/CR EoS (Chattopadhyay & Ryu, 2009) in SMHD regime. We investigate the effect

of using fixed adiabatic index EoS and CR EoS. We also study the effect of plasma composition on jet collimation and flow variables of jet *e.g.,* velocity, temperature, etc.

Therefore, in this thesis, we study the effect of EoSs, and plasma composition on astrophysical magnetized flows, applicable from accretion onto compact objects to relativistic jets.

1.4 Thesis layout

The layout of the thesis is as follows:

- Chapter-1: We introduce the astrophysical flows and the importance of the magnetic field and magnetohydrodynamics.
- Chapter-2: We present an introduction to MHD, SMHD, and EoS. We explain the formation of critical points and methodology to solve equations of motion.
- Chapter-3: We present magnetized accretion solutions onto neutron stars, and white dwarfs. Probably for the first time, we show that with the inclusion of cooling, it is possible to connect flow from the accretion disc to the star's surface.
- Chapter-4: We study the effect of plasma composition on the terminal speed of wind outflow in pseudo- Newtonian gravity.
- Chapter-5: We study jet solutions in SMHD relativistic EOS. We found that plasma composition mainly affects the velocity and temperature of the jet but it does not affect the collimation and fast point location.
- Chapter-6: We conclude the major outcomes of this thesis.

Chapter 2

Mathematical Structure and Methodology to Solve Equations of Motion

2.1 Overview

We have studied magnetized flows (accretion, winds, and jets) and the nature of these flows are quite different from one other (also discussed in Chapter 1). Magnetized accretion flow and winds are generally in non-relativistic to mildly relativistic regime while astrophysical jets from AGNs and XRBs are relativistic in nature. Therefore, we study magnetized accretion and winds from compact object in magnetohydrodynamic regime and collimated outflows or jets in special relativistic magnetohydrodynamic regime. In the next sections, we describe the equations which we used in our study, the formation of critical points and numerical methods used.

2.2 Magnetohydrodynamic equations

The magnetohydrodynamic equations in the non-relativistic regime for a flow which is steady, inviscid and is composed of highly conducting plasma, are as follows (Heinemann & Olbert, 1978; Lovelace *et al.*, 1986; Ustyugova *et al.*, 1999),

$$\boldsymbol{\nabla}.\left(\rho\mathbf{v}\right)=0, \tag{2.1}$$

$$\boldsymbol{\nabla}.\mathbf{B} = 0, \tag{2.2}$$

$$\boldsymbol{\nabla} \times \mathbf{E} = 0, \tag{2.3}$$

$$(\rho\mathbf{v}.\boldsymbol{\nabla})\mathbf{v} = -\boldsymbol{\nabla}p + \frac{1}{c}(\mathbf{J} \times \mathbf{B}) - \Phi'(r)\hat{\mathbf{r}} \tag{2.4}$$

Here, r is radial distance, $\mathbf{v}$ is flow velocity, $\mathbf{E}$ is electric field, $\mathbf{B}$ is magnetic field, ρ is mass density, p is thermal pressure, $\mathbf{J}$ is current density and for highly conducting plasma $\mathbf{J} = c(\boldsymbol{\nabla} \times \mathbf{B})/4\pi$, $\Phi(r)$ is the gravitational potential. Bold letters are denoted the vector quantities. The Newtonian potential (NP) is $\Phi_{\rm NP}(r) = -GM/r$, and its derivative is $\Phi'_{\rm NP}(r) = GM/r^2$. The Paczyński & Wiita (1980) potential (PWP) is given by $\Phi_{\rm PWP}(r) = -GM/(r - r_{\rm g})$ and its derivative is $\Phi'_{\rm PWP}(r) = GM/(r - r_{\rm g})^2$. Where the Schwarzschild radius is $r_{\rm g} = 2GM/c^2$, G is the gravitational constant, M is mass of the central object and c is speed of light.

2.3 Special Relativistic Magnetohydrodynamics equations

The special relativistic magnetohydrodynamic equations can be obtained from the total energy-momentum tensor (Li *et al.*, 1992; Vlahakis *et al.*, 2003a). The energy-momentum tensor for matter is, $T^{\mu\nu}_{\rm matter} = (\bar{e} + p)u^\mu u^\nu + p\eta^{\mu\nu}$, where $\bar{e}$ is energy density, p is gas pressure, the four-velocity components are defined as $u^\mu = (\gamma c, \gamma\mathbf{v})$ and metric tensor components $\eta^{\mu\nu} = \text{diag}\,[-1, 1, 1, 1]$. The energy-momentum tensor of the electromagnetic field is given by $T^{\mu\nu}_{\rm em} = \left(F^{\mu\lambda}F^{\nu}_{\lambda} - \frac{1}{4}\eta^{\mu\nu}F^{\delta\lambda}F_{\delta\lambda}\right)/(4\pi)$. Therefore, the total energy-momentum tensor is $T^{\mu\nu} = T^{\mu\nu}_{\rm matter} + T^{\mu\nu}_{\rm em}$. The conservation of energy and momentum in a covariant form can be written as,

$$\nabla_\nu T^{\mu\nu} = 0. \tag{2.5}$$

Maxwell's equations are,

$$\boldsymbol{\nabla}.\mathbf{B} = 0, \quad \boldsymbol{\nabla}.\mathbf{E} = \frac{4\pi}{c}J^0, \quad \boldsymbol{\nabla} \times \mathbf{B} = \frac{1}{c}\frac{\partial\mathbf{E}}{\partial t} + \frac{4\pi}{c}\mathbf{J}, \quad \boldsymbol{\nabla} \times \mathbf{E} = -\frac{1}{c}\frac{\partial\mathbf{B}}{\partial t}, \tag{2.6}$$

where $J^\mu = \left(J^0, \mathbf{J}\right)$ is four-current density and $\mathbf{E}$ is electric field.

2.4 Closure equations

To solve the equations of motion which are mentioned above whether for MHD or SMHD, we need two more equations. They are, the ideal MHD condition for the electromagnetic field which relates the electric field to the magnetic field and the equation of state (EoS) for the matter which relates the thermodynamic variables. These two equations are known as closure equations because with these two equations we have a closed system *i.e.,* number of unknowns are equal to or less than the number of equations.

2.4.1 Ideal MHD flow assumption

For an ideal MHD flow, the electric field is zero in the co-moving frame (Mobarry & Lovelace, 1986; Choudhuri, 1998; Priest, 2014) *i.e.,* $u_\nu F^{\mu\nu} = 0$ or

$$\mathbf{E} = -\frac{1}{c}\mathbf{v} \times \mathbf{B}. \tag{2.7}$$

This is known as the ideal MHD condition. Then the flux freezing condition can be obtained from the Faraday equation,

$$\boldsymbol{\nabla} \times (\mathbf{v} \times \mathbf{B}) = \frac{\partial \mathbf{B}}{\partial t}.$$

For steady flow, the Faraday equation has the following form,

$$\boldsymbol{\nabla} \times (\mathbf{v} \times \mathbf{B}) = 0. \tag{2.8}$$

2.4.2 Equation of state with fixed adiabatic index

The energy density $\bar{e}$ for fixed adiabatic index Γ (specific heat ratio) or the equation of state (EoS) (see Chapter 6 of Choudhuri, 1998) is given by

$$\bar{e} = \frac{p}{\Gamma - 1},$$

and the adiabatic equation of state for fixed Γ is obtained by integrating the 1^{st} law of thermodynamics without any sink or source term,

$$p = \mathcal{K}\rho^\Gamma, \tag{2.9}$$

where $\mathcal{K}$ is the measure of entropy. If we use the continuity equation (2.1) with equation (2.9) then we obtain the entropy accretion rate $\dot{\mathcal{M}}$,

$$\dot{\mathcal{M}} = v_{\rm g} A_{\rm g} c_{\rm s}^{2N}. \tag{2.10}$$

Here, $c_{\rm s} \equiv \sqrt{\Gamma p/\rho}$ is the sound speed, and $N = 1/(\Gamma - 1)$ is the polytropic index and $A_{\rm g}$ is area across which matter is flowing with velocity $v_{\rm g}$ or in other words $v_{\rm g}$ is velocity component perpendicular to the area $A_{\rm g}$. For example, in case of equatorial stellar wind, $v_{\rm g} = v_{\rm r}$ radial velocity and $A_{\rm g} \propto r^2$ and similarly for poloidal flows *e.g.,* magnetized accretion, $v_{\rm g} = v_{\rm p}$ poloidal velocity and $A_{\rm g} = A_{\rm p}$.

2.4.3 Relativistic equation of state with variable adiabatic index

In the relativistic regime, for fluid having Maxwell-Boltzmann distribution, the ideal equation of state is given by,

$$\bar{e} = \rho c^2 + \frac{p}{\Gamma - 1} \text{ and } h = \frac{\bar{e} + p}{\rho} \tag{2.11}$$

here, h is specific enthalpy. The energy density ($\bar{e}$) also contains the rest mass energy density, and Γ is the adiabatic index which is fixed. In 1948, Taub, using relativistic kinetic theory showed that there is a fundamental inequality,

$$(h - p/\rho c^2)(h - 4p/\rho c^2) \geq 1. \tag{2.12}$$

that should be obeyed by an EoS, therefore the choice of EoS can not be arbitrary. Thus, ideal equation of state (2.11) is ruled out because it does not satisfy the Taub inequality (2.12) for $0 < p/\rho c^2 < \infty$.

We know that the adiabatic index depends upon temperature, and in case of outflow or accretion the temperature varies by two to four orders of magnitude. Additionally mass of the species that constitute the plasma also plays an essential role. So, the composition of the plasma is also important. Thus, to find a more accurate and consistent solutions, we need an EoS which has a temperature and composition dependent adiabatic index. Chandrasekhar (1938) obtained the exact relativistically perfect EoS for hot gas which has a variable adiabatic index. The form of this EoS is

given for single species perfect gas (Chandrasekhar, 1938; Synge, 1957),

$$\bar{e} = \rho c^2 + \rho c^2 \left[\frac{K_3(\rho c^2/p)}{K_2(\rho c^2/p)} - \frac{p}{\rho c^2} - 1 \right] \text{ and } h = \frac{K_3(\rho c^2/p)}{K_2(\rho c^2/p)}, \tag{2.13}$$

where, K_2 and K_3 are modified Bessel functions of the second kind. This equation of state satisfies the Taub inequality (2.12), and has temperature dependent adiabatic index. Thus, we do not need to specify the adiabatic index manually, it is taken care of by the EoS itself. But it is difficult to use this EoS in numerical calculations due to the presence of modified Bessel functions of the second kind, which we know are non-terminating series. There is another approximate and accurate EoS given by Chattopadhyay & Ryu (2009) for multi-species flow (*i.e.,* a flow composed of electron, positron, and proton) having variable adiabatic index — the CR EoS. In our analysis, we will use CR EoS, because it has a simple function $f(\Theta, \xi)$ instead of complicated Bessel functions.

The energy density for multi species flow as stated by CR EoS is given by,

$$\bar{e} = n_{\mathrm{e}^-} m_{\mathrm{e}^-} c^2 f(\Theta, \xi) = \rho_{\mathrm{e}^-} c^2 f(\Theta, \xi) = \frac{\rho c^2 f(\Theta, \xi)}{K}, \tag{2.14}$$

where, $f(\Theta, \xi) = (2 - \xi)\left[1 + \Theta\left(\frac{9\Theta+3}{3\Theta+2}\right)\right] + \xi\left[\frac{1}{\eta} + \Theta\left(\frac{9\Theta+3/\eta}{3\Theta+2/\eta}\right)\right]$, $K = [2 - \xi(1 - 1/\eta)]$, $\Theta = \kappa_{\mathrm{B}} T/m_{\mathrm{e}^-} c^2$ is dimensionless temperature, T is temperature, ρ_{e^-} is rest-mass density of electrons, $\eta = m_{\mathrm{e}^-}/m_{\mathrm{p}^+}$ is electron to proton mass ratio, the composition parameter $\xi = n_{\mathrm{p}^+}/n_{\mathrm{e}^-}$ is the ratio of number density of protons to that of electrons. A flow described by $\xi = 0.0$ implies an electron-positron pair plasma, $0.0 < \xi < 1.0$ imply electron-positron-proton plasma and $\xi = 1.0$ implies electron-proton plasma. Enthalpy h, variable adiabatic index Γ and polytropic index N are given by,

$$h = \frac{\bar{e} + p}{\rho} = \frac{f c^2}{K} + \frac{2\Theta c^2}{K}, \; \Gamma = 1 + \frac{1}{N}, \text{ and } N = \frac{1}{2}\frac{df}{d\Theta}. \tag{2.15}$$

If we integrate the 1$^{\mathrm{st}}$ law of thermodynamics without any sink or source term, we can obtain the adiabatic equation of state which has temperature dependent adiabatic index (Kumar & Chattopadhyay, 2013; Vyas *et al.*, 2015; Singh & Chattopadhyay, 2018b),

$$\rho = \mathcal{K} g(\Theta, \xi), \tag{2.16}$$

where, $g(\Theta, \xi) = \exp(k_3)\Theta^{3/2}(3\Theta + 2)^{k_1}(3\Theta + 2/\eta)^{k_2}$, $k_1 = 3(2 - \xi)/4$, $k_2 = 3\xi/4$ and $k_3 = (f - K)/(2\Theta)$ and $\mathcal{K}$ is the measure of entropy. Similar to fixed adiabatic index EoS

(equation 2.9), we can also obtain the entropy accretion rate $\dot{\mathcal{M}}$ for variable adiabatic index EoS (or CR EoS) with the help of continuity equation (2.1),

$$\dot{\mathcal{M}} = v_{\rm g} A_{\rm g} g(\Theta, \xi). \tag{2.17}$$

2.5 Methodology to solve equations of motion

The equations of motion for an inflow or outflow can be obtained from the momentum balance equation. The equations of motion have a general form irrespective in which flow variable we write it and the flow variables are v, ρ, etc. For example, in terms of velocity variable v, the equations of motion have the following form:

$$\frac{dv}{dr} = \frac{\mathcal{N}(r, v, T)}{\mathcal{D}(r, v, T)}. \tag{2.18}$$

Here $\mathcal{N}$ is numerator and $\mathcal{D}$ is denominator. If we specify the initial conditions then we can find the solution by integrating the equations of motion (2.18) with the help of other equations (*e.g.,* temperature gradient equation from the first law of thermodynamics).

2.5.1 Critical point conditions

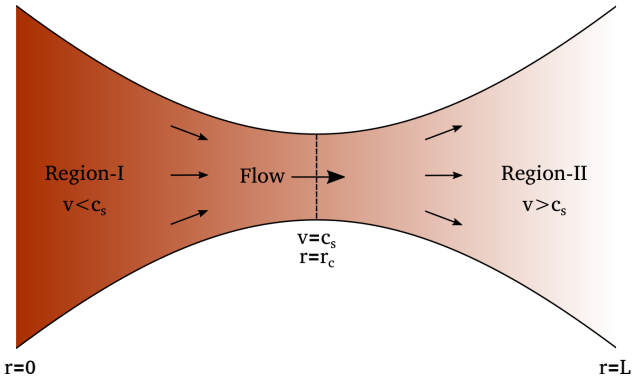

FIGURE 2.1: de-Laval Nozzle.

Formation of a critical point can be understood with an example of the de-Laval nozzle (Fig. 2.1) in HD regime, whose cross-sectional area (A) is a function of distance (r) *i.e.,* $A \equiv A(r)$. So with the help of the continuity equation and momentum balance equation, we can write the equations of motion for the flow which passes through the

tube like in Fig. 2.1 and has the following form (see section 6.7 Choudhuri, 1998),

$$\frac{dv}{dr} = \frac{\mathcal{N}(r, v, T)}{\mathcal{D}(r, v, T)} = \frac{-\frac{v}{A}\frac{dA}{dr}}{1 - M^2}. \tag{2.19}$$

Here, M is Mach number, $M = v/c_{\rm s}$. In equation (2.19), we note that velocity slope (dv/dr) and area slope (dA/dr) have opposite sign. Therefore, in region-I, if flow is subsonic ($v < c_{\rm s}$ or $M < 1$) and the area is converging (dA/dr is negative) then velocity slope becomes positive *i.e.,* flow is accelerating. Now, in region-II, flow is supersonic ($v > c_{\rm s}$ or $M > 1$) and area is diverging (dA/dr is positive) then again velocity slope becomes positive *i.e.,* flow is accelerating. Therefore, flow can become subsonic to supersonic when it passes through a throat which has shape as shown in Fig. 2.1. It also means that at some distance, flow velocity becomes equal to the local sound speed *i.e.,* $v = c_{\rm s}$ or $M = 1$ at distance $r = r_{\rm c}$, and at this distance, velocity slope attains $0/0$ form or $\mathcal{N}|_{r_{\rm c}} = \mathcal{D}|_{r_{\rm c}} = 0$ (see equation 2.19) since area slope is also zero at this point. This point is known as critical point and $r_{\rm c}$ is the critical point radius.

It may be noted that even in absence of an explicit throat in the flow geometry, it is the presence of gravity (*e.g.,* see the last term in the expression of $\mathcal{N}$ in equation 3.21 for magnetized accretion and also in equation 4.14 for outflows), which mathematically acts as an effective throat and causes the formation of a critical point in a flow. The presence of centrifugal and magnetic forces modify the effective gravity throat at different locations and as a result, we have multiple critical points (MCP) of different kinds, X-type critical point (has real velocity slope), O-type (has imaginary velocity slope), and if cooling is present then we have spiral-type critical point (has complex velocity slope). We know that plasma has three signal speeds (say $v_{\rm S}$) *i.e.,* slow speed, Alfvén speed, and fast speed. When the flow velocity is equal to one of the signal speed at a certain point (say $r_{\rm c}$) then equation (2.18) has $0/0$ or $\mathcal{N}|_{r_{\rm c}} = \mathcal{D}|_{r_{\rm c}} = 0$. So, in MHD or SMHD, we have three types of critical points, a slow critical point (flow velocity is equal to the slow speed), Alfvén critical point (flow velocity is equal to Alfvén speed) and fast critical point (flow velocity is equal to fast speed).

We can also use a critical point as the initial boundary for the integration of the equations of motion (2.18) by evaluating the velocity slope at the critical point with the help of L'Hospital's rule. One of the benefits of choosing critical point as the initial boundary for integration is that at this point $v = v_s$ which simplifies the equations of motion. A transonic solution is one which passes through the critical points and has maximum entropy. For example, a wind outflow solution passes through three critical

points (slow, Alfvén, and fast points) (see section 4.4). Therefore transonic solutions are the only plausible solutions for inflows or outflows.

2.5.2 Numerical Methods

In all studies, we used the Newton-Raphson method to find critical points from critical point conditions. The Newton-Raphson method has faster convergence than the bi-section method because it takes into account the slope of functions. To solve the indeterminate form of velocity slope at the critical point, we use 2^{nd} order numerical difference method for L'Hospital's rule. For solution integration, we used Runge-Kutta 4^{th} order method.

Chapter 3

The Study of Magnetized accretion flow onto compact objects

3.1 Overview

Neutron stars (NSs) are very fascinating objects because they have strong magnetic field and gravitational field. Also, white dwarfs (WDs) have very strong magnetic field. As we have discussed in Chapter 1, these objects after certain radius ($B^2/8\pi \sim (p, \rho v^2)$) accrete matter (from the inner region of the disc) in the form of accretion curtains along the field lines. In this chapter, we investigate magnetized accretion flow onto NSs and WDs by extending Koldoba *et al.* (2002) and Karino & Kino (2008), by considering Paczyński-Wiita pseudo-potential to mimic strong gravity. We include cooling processes (bremsstrahlung and cyclotron cooling) and assume fixed as well as variable adiabatic index EoS or CR EoS (Chattopadhyay & Ryu, 2009) for different compositions of flow. We calculate the parameter space and study magnetized accretion solutions for different rotation periods of the star and energy of the flow. We found that accretion solution has a very strong shock near the star's surface which is the primary shock, and for certain parameters (energy, rotation period of the star), accretion solution also has a weaker secondary shock very far away from the star. We have found that cooling is important to get a consistent magnetized accretion solution which satisfies the surface boundary of star *i.e.*, $v \to 0$ because cooling radiates away energy of the shock

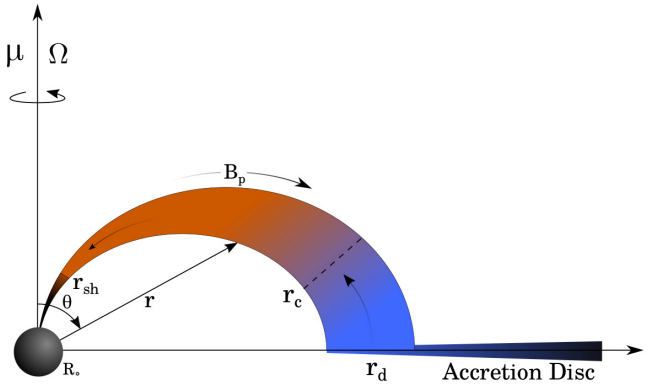

FIGURE 3.1: This is illustration of magnetized accretion flow onto NS for aligned magnetic moment (μ) with angular velocity (Ω). Where, θ is polar angle, r is radial distance, $R_\circ$ is star's radius, B_p is polodial magnetic field, r_sh is shock radius, r_c is critical point radius, and r_d is radius from the matter starts channelling the magnetic field.

and helps matter to slowly settle down onto the star's surface. Further, we investigate the shock properties *e.g.,* shock height, compression ratio, shock strength, luminosity, etc and study their dependence on the rotation period of the star and energy of the flow. As we have mentioned that composition of astrophysical flows is poorly known, so we have studied parameter space and magnetized accretion solutions for flow having different compositions. We have also investigated magnetized accretion flow onto a WD and our results have good match with the observations. We study the dynamics of magnetized accretion solutions with inclusion of cooling processes onto magnetized stars using fixed adiabatic index EoS and variable adiabatic index EoS (CR EoS) and these results are published in Singh & Chattopadhyay (2018a,b) respectively.

3.2 Equations and Assumptions

3.2.1 Governing Equations

We have used the MHD equations which were mentioned in 2.2 with assumptions that the flow is steady and axisymmetric. Therefore, velocity has the form $\mathbf{v} \equiv \mathbf{v}(\mathbf{v}_\mathrm{p}, \mathbf{0}, \mathbf{v}_\phi)$ and magnetic field $\mathbf{B} \equiv \mathbf{B}(\mathbf{B}_\mathrm{p}, \mathbf{0}, \mathbf{B}_\phi)$, where $\mathbf{v}_\mathrm{p}$ is poloidal velocity, $\mathbf{v}_\phi$ is azimuthal velocity, $\mathbf{B}_\mathrm{p}$ is poloidal magnetic field, and $\mathbf{B}_\phi$ is azimuthal magnetic field.

In presence of cooling, the $1^{\rm st}$ law of thermodynamics is given by

$$\rho v_{\rm p}\left[\frac{de}{dr}-\frac{p}{\rho^2}\frac{d\rho}{dr}\right]=Q_{\rm br}+Q_{\rm cycl}=Q, \tag{3.1}$$

where, $e=\bar{e}/\rho$ is the internal energy, $\bar{e}$ is the energy density, p is pressure, ρ is mass density and Q is the total cooling. $Q_{\rm br}$ is the bremsstrahlung cooling term and which is given by,

$$Q_{\rm br}=\lambda_{\rm br}\rho^2 T_{\rm e^-}^{1/2}, \tag{3.2}$$

where, $T_{\rm e^-}$ is electron temperature and $\lambda_{\rm br}\sim 5\times10^{20}$erg cm^{-3}g^{-2}s^{-1}. $Q_{\rm cycl}$ is cyclotron cooling term. Cyclotron cooling is a very complicated process where both emission and resonant absorption can be important. Therefore, depending on the frequency of the radiation, the flow might behave as an optically thick or thin medium, although the Thompson scattering optical depth of the flow might be well below 1. Generally, such complications are avoided by considering a cooling function which mimics all the complicated cooling processes (Saxton *et al.*, 1998). We choose the form of $Q_{\rm cycl}$ given by Busschaert *et al.* (2015),

$$Q_{\rm cycl}=\lambda_{\rm cycl}\left(\frac{A_{\rm p}}{10^{15}{\rm cm}^2}\right)^{-17/40}\left(\frac{B_{\rm p}}{10^7{\rm G}}\right)^{57/20}\times\left(\frac{\rho}{4\times10^{-8}{\rm g/cm}^3}\right)^{3/20}\left(\frac{T_{\rm e^-}}{10^8{\rm K}}\right), \tag{3.3}$$

where, $B_{\rm p}$ is the poloidal magnetic field component and $A_{\rm p}$ is the cross-section of the flow orthogonal to $B_{\rm p}$ and $\lambda_{\rm cycl}\sim1.2\times10^8$erg cm^{-3}s^{-1} (Busschaert *et al.*, 2015).

If we integrate the MHD equations in the presence of the above assumptions along the magnetic field lines then we can obtain the conserved quantities which are labelled with the magnetic stream function $\Psi(r,\theta)$. The conserved quantities are:

(i) By integrating continuity equation (2.1) we obtain the expression of mass flux $(\dot{M})$,

$$\rho v_{\rm p}A_{\rm p}=\text{constant}=\dot{M}. \tag{3.4}$$

(ii) Integrating equation (2.2), we obtain the magnetic flux conservation,

$$B_{\rm p}A_{\rm p}=\text{constant}. \tag{3.5}$$

Using equations (3.4) and (3.5), we can write $v_{\rm p}$ as

$$v_{\rm p}=\frac{\kappa(\Psi)}{4\pi\rho}B_{\rm p}, \tag{3.6}$$

where, κ is the mass to magnetic flux ratio.

(iii) Faraday equation (2.3) for highly conducting fluid gives the conservation of angular velocity of magnetic field lines (Ω),

$$\Omega\left(\Psi\right) = \omega - \frac{\kappa(\Psi) B_{\phi}}{4\pi\rho\varpi} = \text{constant}, \tag{3.7}$$

where, $\omega = v_{\phi}/r\sin(\theta)$ is the angular velocity and $\varpi = r\sin(\theta)$ is the cylindrical radius.

(iv) ϕ-component of momentum balance equation (2.4) gives the total angular momentum (Λ) which remains conserved along the magnetic field lines,

$$\Lambda(\Psi) = \omega\varpi^2 - \frac{B_{\phi}\varpi}{\kappa(\Psi)} = \text{constant}. \tag{3.8}$$

(v) Therefore, integration of poloidal component of momentum balance equation (2.4) gives the conservation of total energy (E) along the magnetic field lines,

$$E(\Psi) = \frac{1}{2}v_{\rm p}^2 + \frac{1}{2}(\omega - \Omega)^2\varpi^2 + h + \Phi(r) - \frac{\Omega^2\varpi^2}{2} - \int \frac{Qdr}{\rho v_{\rm p}} = \text{constant}. \tag{3.9}$$

In the above equations, h is the specific enthalpy. Equation (3.9) is the generalized Bernoulli integral along the magnetic field lines which remains constant even in the presence of cooling. One can retrieve the canonical form of Bernoulli integral assuming an adiabatic flow (Lovelace *et al.*, 1986; Ustyugova *et al.*, 1999; Koldoba *et al.*, 2002), if cooling is not considered.

3.2.2 Assumptions

We assume that NS has a dipole-like magnetic field whose magnetic moment (μ) is aligned with the rotation axis of the star (Koldoba *et al.*, 2002), see Fig. 3.1. Here, we have assumed that the magnetic field is very strong so that the flow does not alter the configuration of the magnetic field lines and this also implies that the flow is sub-Alfvén,

$$B_{\rm p}^2/8\pi \gg (p, \rho v^2) \;\text{ and }\; \rho_{\rm A}/\rho \ll 1 \;\text{ or }\; M_{\rm A}^2 \ll 1. \tag{3.10}$$

In the above, the poloidal Alfvénic Mach number is defined by

$$M_{\rm A}^2 \equiv \frac{v_{\rm p}^2}{v_{\rm Ap}^2} = \frac{\rho_{\rm A}}{\rho}, \tag{3.11}$$

where $v_{\rm Ap}^2 = B_{\rm p}^2/4\pi\rho$ and $\rho_{\rm A} = 4\pi\kappa(\Psi)$. The stream function (Ψ) for the dipole magnetic field in spherical coordinates is given by,

$$\Psi = \frac{\mu}{r}\sin^2(\theta) \quad \text{or} \quad r = r_{\rm d}(\Psi)\sin^2(\theta), \tag{3.12}$$

where $r_{\rm d} = \mu/\Psi$ is the radius from where the matter starts channelling the magnetic field lines and $B_{\rm p}$ is given by,

$$B_{\rm p}(r) = \frac{\mu}{r^3}(4 - 3\sin^2(\theta))^{1/2} \quad \text{or} \quad B_{\rm p}(r) = \frac{\mu}{r^3}(4 - 3r/r_{\rm d})^{1/2}. \tag{3.13}$$

We can obtain relations for ω and B_ϕ by using equations (3.7) and (3.8) with the strong magnetic field and sub-Alfénic assumption (for more detail see Koldoba *et al.* (2002); Singh & Chattopadhyay (2018b)),

$$|\omega - \Omega|/\Omega \ll 1 \text{ and } B_\phi/B_{\rm p} \ll 1. \tag{3.14}$$

The first relation implies that the local angular velocity (ω) of the fluid remains constant along the magnetic field lines and is equal to the angular velocity of the magnetic field lines $\Omega(\Psi)$. If the magnetic field lines are locked into the star's surface then $\Omega(\Psi) = \Omega_{\rm star}$, where $\Omega_{\rm star}$ is the angular velocity of a star. It means that the strong magnetic field forces the matter to co-rotate with the star. Therefore, $r_{\rm d}$ should be close to the co-rotation radius $r_{\rm co}(\equiv \left[GM_\circ/\Omega^2\right]^{1/3})$. Our assumption will not work for $r_{\rm d} \gg r_{\rm co}$. For that we have to take into account the effect of disc on the magnetic field configuration. The second relation shows that azimuthal component of magnetic field (B_ϕ) is negligible as compared to poloidal component of the magnetic field $(B_{\rm p})$, so we can neglect it. Cross-sectional area $(A_{\rm p})$ can be calculated from equations (3.5) and (3.13).

3.2.3 Entropy Accretion Rate and Electron Temperature

If we ignore any dissipative processes, then by integrating $1^{\rm st}$ law of thermodynamics without any source or sink term, we can obtain the adiabatic relation. Therefore, for

fixed adiabatic index EoS, the entropy accretion rate is given by (2.4.2),

$$\dot{\mathcal{M}} = v_{\rm p} A_{\rm p} c_{\rm s}^{2N} = \text{ constant for adiabatic flow.} \tag{3.15}$$

We have included radiative cooling processes (equations 3.2, 3.3) unlike Koldoba *et al.* (2002) and Karino & Kino (2008). We will show later that the flow will not come to rest on the surface of the central compact object if we neglect dissipation. Since this is not a two temperature solution but a one temperature problem with proton and electron having the same temperature. So computing the emissivity using T would overestimate. The electron temperature $T_{\rm e^-}$ is in general smaller than the proton temperature, and we approximate it as $T_{\rm e^-} = \sqrt{m_{\rm e^-}/m_{\rm p}} T$ (Chattopadhyay & Chakrabarti, 2002; Das & Chattopadhyay, 2008) in case of fixed adiabatic index EoS.

In case of variable adiabatic index EoS or CR EoS, the entropy accretion rate ($\dot{\mathcal{M}}$) is given by (2.4.3),

$$\dot{\mathcal{M}} = v_{\rm p} A_{\rm p} g(\Theta, \xi) = \text{ constant for adiabatic flow.} \tag{3.16}$$

To estimate the electron temperature $T_{\rm e^-}$ in CR EoS, we assume that the electron gas possess the same N as our single temperature, multi-species solution. Therefore, the approximated electron temperature is given by Kumar & Chattopadhyay (2014)

$$T_{\rm e^-} = \left[-\frac{2}{3} + \frac{1}{3}\sqrt{4 - 2\frac{(2N-3)}{(N-3)}} \right] \frac{m_{\rm e^-} c^2}{\kappa_{\rm B}}. \tag{3.17}$$

In case of CR EoS, the sound speed is defined by,

$$c_{\rm s}^2 \equiv \frac{2\Gamma(\Theta,\xi)\Theta c^2}{K}. \tag{3.18}$$

3.2.4 Bernoulli Function and Equations of Motion with Dipole Magnetic Field Assumption

Under the present set of assumptions, the Bernoulli integral from equation (3.1) and (3.9) takes the following form,

$$\mathcal{B}\left(r, v_{\rm p}\right) = \frac{v_{\rm p}^2}{2} + h + \Phi_{\rm g}(r) - \int \frac{Q dr}{\rho v_{\rm p}}, \tag{3.19}$$

where, $v_{\rm p} = \mu\kappa(\Psi)\left(4-3r/r_{\rm d}\right)^{1/2}/4\pi\rho r^3$, $\Phi_{\rm g}(r) = -\Omega^2 r_{\rm co}^2\left(\frac{\alpha r_{\rm d}}{r-r_{\rm g}}+\frac{r^3}{2\alpha^2 r_{\rm d}^3}\right)$, $\alpha = r_{co}/r_{\rm d} = 1$, $r_{\rm g} = 2GM_{\circ}/c^2$. Gradient of $v_{\rm p}$ can be obtained by taking the space derivative of the Bernoulli integral (equation 3.19),

$$\frac{dv_{\rm p}}{dr} = \frac{\mathcal{N}(r, v_{\rm p}, \Theta)}{\mathcal{D}(r, v_{\rm p}, \Theta)}, \tag{3.20}$$

where,

$$\mathcal{N}(r, v_{\rm p}) = \frac{3c_{\rm s}^2}{2r}\left(\frac{8-5r/r_{\rm d}}{4-3r/r_{\rm d}}\right) - \frac{\delta}{n} - \Phi_{\rm g}^{'}(r), \tag{3.21}$$

$$\mathcal{D}(r, v_{\rm p}) = \left(v_{\rm p} - \frac{c_{\rm s}^2}{v_{\rm p}}\right) \text{ and } \delta \equiv \frac{Q}{\rho v_{\rm p}}. \tag{3.22}$$

We have considered the full energy balance (equation 3.1), which gives the gradient in temperature in the presence of cooling,

$$\frac{d\Theta}{dr} = \left(\frac{\delta K}{2Nc^2}\right) - \frac{\Theta}{N}\left[\frac{1}{v_{\rm p}}\frac{dv_{\rm p}}{dr} + \frac{3\left(8-5r/r_{\rm d}\right)}{2r\left(4-3r/r_{\rm d}\right)}\right]. \tag{3.23}$$

3.2.5 Shock Conditions

The MHD shock conditions (Kennel *et al.*, 1989) reduce to simple hydrodynamic shock conditions with the help of strong field approximation, where the information of magnetic field lies inside the poloidal velocity,

$$[\rho v_{\rm p}] = 0, \left[\rho v_{\rm p}^2 + p\right] = 0, \text{and } \left[\rho v_{\rm p}\left\{\frac{v_{\rm p}^2}{2} + h - \int\frac{Qdr}{\rho v_{\rm p}}\right\}\right] = 0. \tag{3.24}$$

Square bracket implies the difference of the pre-shock and post-shock flow quantities.

3.3 Methodology

In section 2.5.1, we explained how critical points form. Physically, in case of accretion, gravity accelerates the inflow from the accretion radius towards the central object and thereby primarily increases the kinetic energy of the flow. However, since accretion is a convergent flow it increases the temperature as a secondary effect. Therefore, gravity while pulling the flow towards the central object increases both the velocity and temperature (and therefore the sound speed, which also affects the plasma signal speeds) together but increases the inflow velocity with a sharper gradient. This causes the flow velocity to cross the local signal speed at the critical point ($r_{\rm c}$). Now if the flow is also rotating and magnetized, then the nature of gravitational interaction can

be modified (by centrifugal force and magnetic force). Then the flow can have MCP ***i.e.,*** the flow can become transonic at different distances for a given set of parameters.

In the present study, due to the strong magnetic field assumption, we have one signal speed which is the sound speed. Therefore, a critical point forms when flow velocity ($v_{\rm p}$) is equal to local sound speed. Because in this case, the centrifugal force is present, so we may have multiple critical points. To solve the equations of motion (3.20, 3.23), one needs to specify the gravitational field via star's mass ($M_\circ$), star's rotation period (P) and the surface magnetic field of the star ($B_{\rm p\circ}$). Star's radius $R_\circ$ is an input parameter. It is well known that a small value of $M_\circ/R_\circ$ makes $\Phi(r)$ closer to the Newtonian gravitational potential. In this study, we aimed at magnetized accretion onto NS, but we have also modified these input parameters to study funnel accretion onto WD too, which would be presented later in the result section. Moreover, the rotation period of the star and surface magnetic field have some relation has also been observed (see, Pan *et al.*, 2013). In this study, we have considered radiative cooling, so either we have to supply the accretion rate ($\dot{M}$), or equivalently, supply the density ($\rho_{\rm d}$) at some distance ($r_{\rm d}$) from the central object. So, we need only two parameters, P and $\rho_{\rm d}$ as inputs. Then, we can find the poloidal velocity ($v_{\rm pc}$) or mass density ($\rho_{\rm c}$), and dimensionless temperature ($\Theta_{\rm c}$) at the critical radius ($r_{\rm c}$) from the critical point conditions (equations 3.21 & 3.22, $\mathcal{N}(r,v_{\rm p})|_{r_{\rm c}}=\mathcal{D}(r,v_{\rm p})|_{r_{\rm c}}=0$).

Flow generally starts with a subsonic velocity from $r_{\rm d}$ and after passing through a critical/sonic point, it becomes supersonic. The star's surface acts as the obstruction for the supersonic matter and drives a terminating shock near the surface. This is true for accretion solutions of all compact objects with a hard surface. The cooling processes are particularly dominant in the post-shock region since the post-shock is denser and hotter. Apart from the necessity to include cooling from physical arguments, we found that the cooling processes are absolutely necessary condition, in order to obtain a believable accretion solution. By radiating away a lot of shock-heated energy, the cooling processes help to achieve the inner boundary condition of $v_{\rm p}\rightarrow 0$ as $r\rightarrow R_\circ$. Moreover, the flow is rotating, so multiple sonic points may also occur and if that is the case, then the possibility of forming multiple shocks increases.

The method to find an accretion solution is as follows:

1. We find the critical point location and value of flow variables at that point and then velocity slope $(dv_{\rm p}/dr)_{r_{\rm c}}$ with the help of the L'Hospital's rule at the critical point for given set of compact object parameters $B_{\rm p\circ},\ P,\ M_\circ,\ R_\circ$.

2. We then integrate the equations of motion (3.20, 3.23) forward and backward from the critical point by using fourth order Runga-Kutta method.

3. While integrating we simultaneously check for the shock conditions (equation 3.24). If the shock conditions are satisfied at some radius $r_{\rm sh}$ then we compute the post-shock variables and then start integration from the shock but now on the post-shock branch.

4. Near the star's surface, we search for the post-shock solution which matches the surface boundary condition of the star.

3.4 Analysis and Results

As far we know this kind of study has not been done in the literature. So, we do not know the topology and nature of magnetized accretion solution with full cooling processes. Thus to understand the methodology to find a consistent magnetized solution, we have first studied magnetized flow with the inclusion of cooling (cyclotron and bremsstrahlung) using fixed adiabatic index of EoS which is mathematically and numerically easier to handle. We used expressions of $c_{\rm s}, h, T_{\rm e}, \dot{\mathcal{M}}$ and Γ according to the EoS but the form of equations of motion (see in the sections 3.2.2, 3.2.4, 3.2.5) remain same for both the EoS.

The analysis is done in the geometrical units, which means that velocity is in units of c and distance in terms of $r_{\rm g} = \frac{2GM_\circ}{c^2}$. We have considered that the radius and mass of the star as $R_\circ = 1.0 \times 10^6$cm and $M_\circ = 1.4\ M_\odot$, respectively. Therefore, in units of $r_{\rm g}$, the radius of the star is $R_\circ = 2.418 r_{\rm g}$ but we quote the rotation period (P) in seconds. The adiabatic index $\Gamma = 5/3$ and $\alpha = 1$.

3.4.1 Comparison of solutions in Newtonian and Paczyński-Wiita potential

In this section, we have discussed and compared the solutions of Koldoba's model (*i.e.,* no cooling) in Newtonian and Paczyński-Wiita potential. As we have discussed in Chapter 1 that in Newtonian potential (NP), we have a maximum two critical points and solutions are only α-type, however in Paczyński-Wiita potential (PWP), we have a maximum three critical points. In Fig. 3.2, we have plotted the $\mathcal{B}_{\rm c}$ versus $r_{\rm c}$ in panel (a), $\mathcal{B}_{\rm c}$ versus $\dot{\mathcal{M}}_{\rm c}$ in panel (b), logΘ in panel (c) and log$M$ in panel (d) versus r, dashed red curves for NP and solid green curves for PWP. These are solutions using Koldoba's

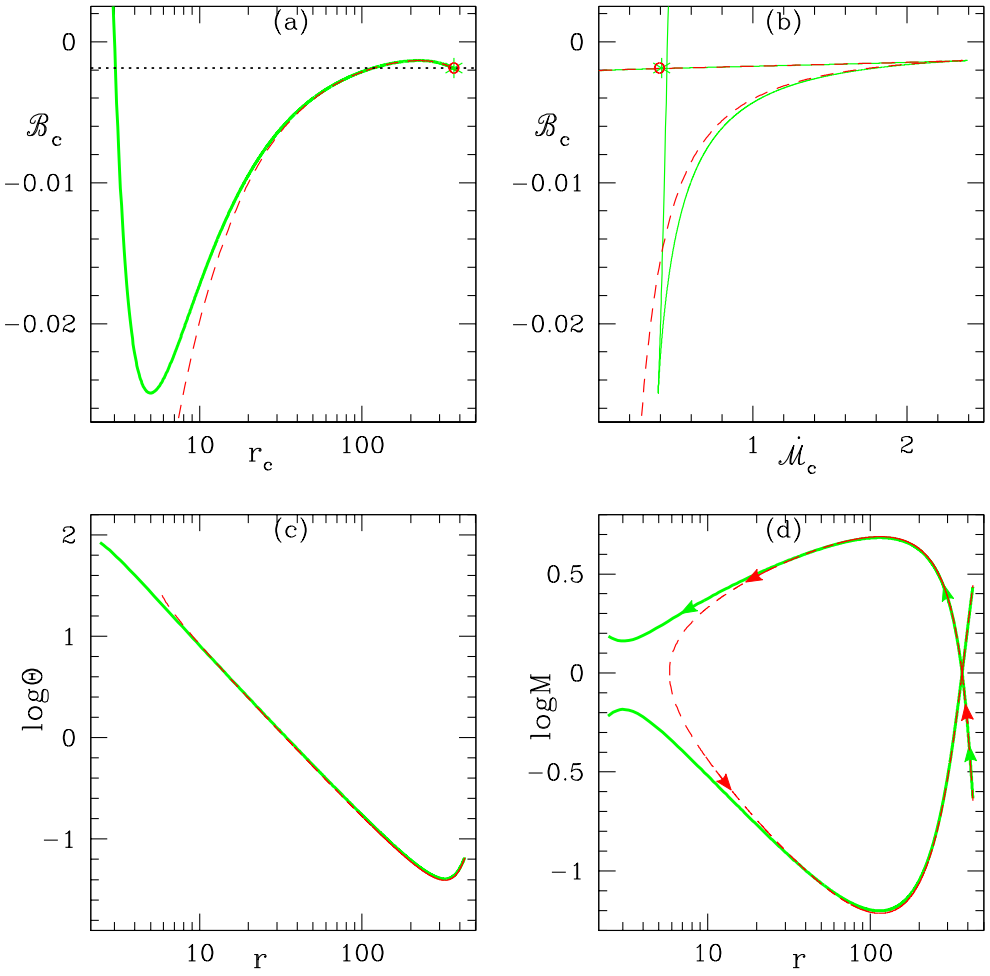

FIGURE 3.2: We have plotted the $\mathcal{B}_c$ versus r_c in panel (a), $\mathcal{B}_c$ versus $\dot{\mathcal{M}}_c$ in panel (b), logΘ in panel (c) and log$M$ in panel (d) versus r, dashed red curves for NP and solid green curves for PWP. Here $P = 1$s, $\mathcal{B} = -0.00190$ (dotted black).

model for neutron star having rotation period $P = 1$s, $\mathcal{B} = -0.00190$ and using fixed adiabatic index EoS.

In Fig. 3.2 (a), we can see that for $\mathcal{B} = -0.00190$ (dotted black), only two critical points are possible in NP (dashed, red) and three critical points in PWP (solid green). For the outer critical point (denoted by red open-circle for NP and green asterisk for PWP in Fig. 3.2 a), we have calculated the solutions. We can note that the accretion solution which is denoted by red-dashed curve with arrows for NP does not reach the star surface (see Fig. 3.2 d). However, for the accretion solution which is denoted by green-solid curve with arrows reaches the star surface (see Fig. 3.2 d). However, only for small parameter range, α-type solutions can be considered as magnetized accretion solutions but we do not know parameter range prior for those solutions, and there is

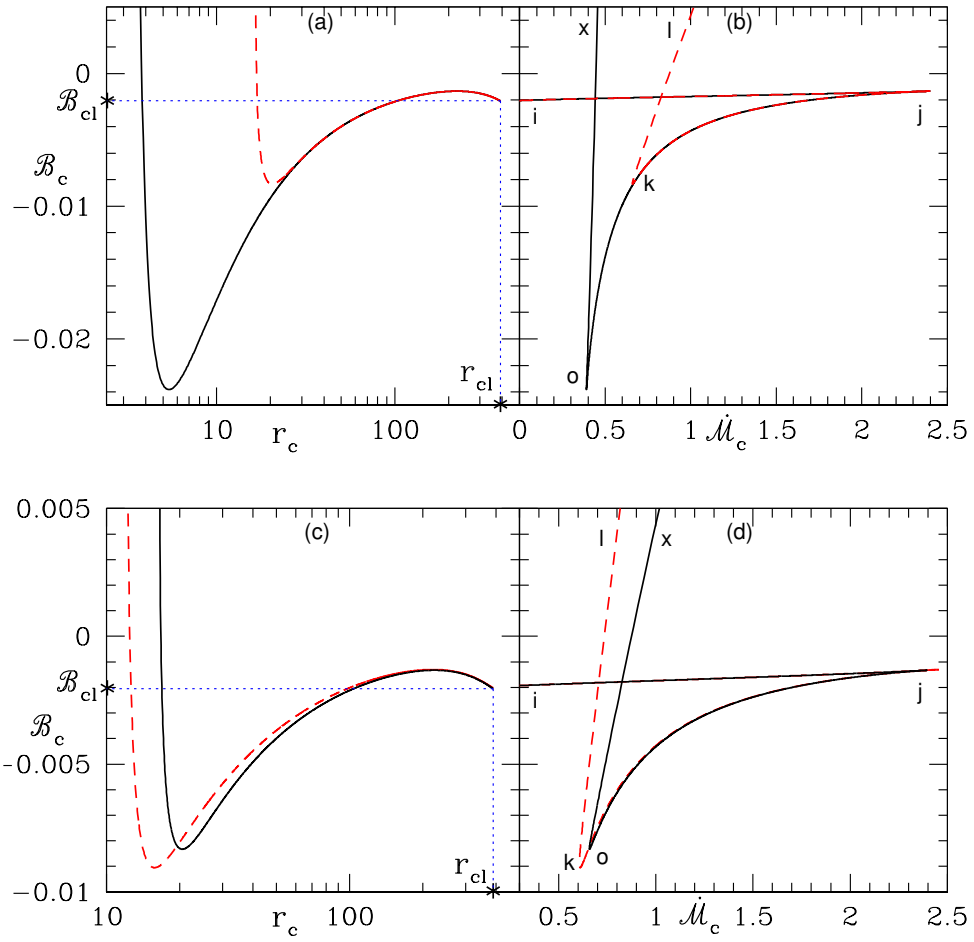

FIGURE 3.3: Total energy $\mathcal{B}_c$ is plotted with r_c (a, c) and $\mathcal{B}_c$ versus entropy accretion rate $\dot{\mathcal{M}}_c$ (b, d). The upper plots are for two values of surface magnetic field $B_{p\circ} = 10^9$G (solid, black) and 10^{11}G (dashed, red) for a density $\rho_d = 5.0 \times 10^{-10}$g cm^{-3} (a, b). In lower two panels (c, d) the plots are for two values of density $\rho_d = 5.0 \times 10^{-10}$g cm^{-3} (solid, black) and 1.0×10^{-8}g cm^{-3} (dashed, red) for $B_{p\circ} = 10^{11}$G. All the plots are for $P = 1$s (Singh & Chattopadhyay, 2018a).

no inner critical point present for NP (see Fig. 3.2 a) that means no shock solutions. To overcome this problem, we used Paczyński-Wiita potential in the rest of our analysis.

3.4.2 Solutions using fixed adiabatic index EoS

For $P = 1$s, we have plotted the $\mathcal{B}_c$ versus r_c in Fig. 3.3 (a, c) and $\mathcal{B}_c$ versus $\dot{\mathcal{M}}_c$ in Fig. 3.3 (b, d). In upper two panels (Fig. 3.3 a, b), we consider $\rho_d = 5.0 \times 10^{-10}$g cm^{-3} but two values magnetic field $B_{p\circ} = 10^9$G (solid, black) and $B_{p\circ} = 10^{11}$G (dashed, red). In Fig. 3.3 (c, d), we consider surface magnetic field as $B_{p\circ} = 10^{11}$G but two values of $\rho_d = 1.0 \times 10^{-8}$g cm^{-3} (solid, black) and $\rho_d = 5.0 \times 10^{-10}$g cm^{-3} (dashed, red). Dotted blue curves in Fig. 3.3 (a, c) show the upper limit of r_c, i. e., r_{cl} and its corresponding energy $\mathcal{B}_{cl}$. If there is a maximum and a minimum in the $\mathcal{B}_c - r_c$ curve for a given

value of P, then there is a possibility of forming multiple critical/sonic points (MCP), if the energy of the flow happens to fall in between the maximum or minimum values. For example, if $\mathcal{B}$ is between -0.0083 to -0.0013 for the accretion flow characterized by curve light-dashed in Fig. 3.3 (a), then the flow will harbour MCP. The $\mathcal{B}_{\rm c}$—$\dot{\mathcal{M}}_{\rm c}$ plots (Fig. 3.3 b, d) also show the same effect. The kite-tail feature is symptomatic of MCP. Various combinations of $\mathcal{B}_{\rm c}$ and $\dot{\mathcal{M}}_{\rm c}$, produce the sonic points, the IK (XO) branch of the dashed-solid curve is the loci of inner sonic points, KJ (OJ) branch of the dashed-solid curve is loci of middle sonic points and IJ curve is loci of outer sonic points (Fig. 3.3 b, d). As long as the entropy of the inner sonic point ($\dot{\mathcal{M}}_{\rm c}$) is greater than that of the outer sonic point, then there is possibility of a second shock formation away, and in addition to the shock forming close to the star's surface.

We have plotted the log of Mach number log$M$ (Fig. 3.4 a), poloidal velocity log$v_{\rm p}$ (Fig. 3.4 b), dimensionless temperature logΘ (Fig. 3.4 c) and entropy-accretion rate ($\dot{\mathcal{M}}$) (Fig. 3.4 d) as a function of r. The accretion parameters are $P = 1$s, $B_{\rm p\circ} = 10^{10}$G, $\rho_{\rm d} = 5 \times 10^{-10}$g cm^{-3} and $\mathcal{B} = -0.00203$. The accretion flow passes through the outer sonic point and then suffers a shock at radius 12.897. The subsonic post-shock matter accelerates and again becomes supersonic as it crosses the inner sonic point. This supersonic matter again suffers a shock at radius 2.434, which is very close to the surface of the star. The inset in each panel zooms onto the inner shock. The temperature and the poloidal velocity starts from quite low values and becomes relativistic. The temperature in the inner post-shock region reaches a very high values, due to cooling processes decreases drastically down to very lower values. Because of the presence of cooling processes the entropy is not constant (Fig. 3.4 d).

We plot log$M$ (Fig. 3.5 a), log$v_{\rm p}$ (Fig. 3.5 b), logΘ (Fig. 3.5 c) and $\dot{\mathcal{M}}$ (Fig. 3.5 d) as a function of r, which also harbours multiple shock with a much faster rotating system with $P = 10$ms, $B_{\rm p\circ} = 3.16 \times 10^{8}$G, $\rho_{\rm d} = 5 \times 10^{-10}$g cm^{-3} and $\mathcal{B} = -0.02846$. The two shocks are located at radii 5.081 and 8.414, but are much weaker than the previous case.

3.4.3 Solutions using variable adiabatic index EoS

In this section, we present results of magnetized accretion or funnel flow with variable adiabatic index EoS (CR EoS). In this analysis, for NS we have considered same $R_\circ = 1.0 \times 10^{6}$cm and mass $M_\circ = 1.4 M_\odot$ and also same unit system as in the case of fixed adiabatic index EoS analysis.

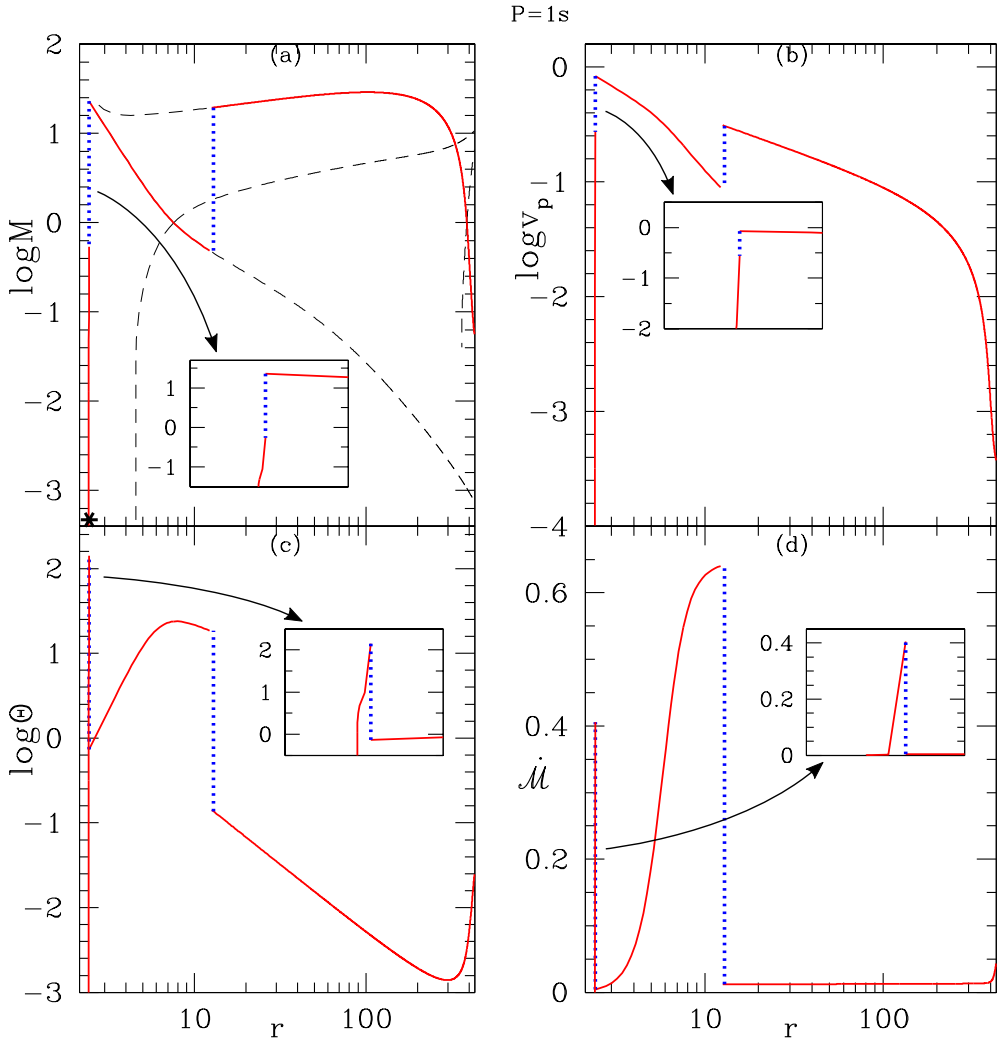

FIGURE 3.4: The accretion solution for $P = 1$ s. Log of Mach number $\log M$ in panel (a), log of poloidal velocity $\log v_{\rm p}$ in panel (b), log of dimensionless temperature $\log\Theta$ in panel (c) and $\dot{\mathcal{M}}$ in panel (d), as a function of r. The accretion solution is represented by solid red curve, shock by dotted blue curve and other branch of solution by dashed-black curve (Singh & Chattopadhyay, 2018a).

Similar to fixed adiabatic index EoS analysis, we have also studied the parameter space with CR EoS. We have plotted $\mathcal{B}_{\rm c}$ versus $r_{\rm c}$ in Fig. 3.6 (a, c) and $\mathcal{B}_{\rm c}$ versus $\dot{\mathcal{M}}_{\rm c}$ in Fig. 3.6 (b, d). Different curves in the upper two panels (Fig. 3.6 a, b) are plotted for $B_{\rm po} = 10^9$G (solid, black) and $B_{\rm po} = 10^{11}$G (dashed, red), but for the same value of $\dot{M} = 3.51 \times 10^{15}$g s^{-1}. The curves in the lower two panels (Fig. 3.6 c, d) are plotted for two values of $\dot{M} = 3.51 \times 10^{15}$g s^{-1} (solid, black) and $\dot{M} = 3.51 \times 10^{16}$g s^{-1} (dashed, red), but for the same value of $B_{\rm po} = 10^{11}$G. All the plots are for the same $P = 1$s and $\xi = 1$. It may be noted that in this case also, each of the $\mathcal{B}_{\rm c}(r_{\rm c})$ curve has a maximum $\mathcal{B}_{\rm cmax}$ and a minimum $\mathcal{B}_{\rm cmin}$. Any flow for which $\mathcal{B}_{\rm cmin} \leq \mathcal{B} \leq \mathcal{B}_{\rm cmax}$, there can be three critical/sonic points *i.e.*, inner, middle and outer sonic points. The inner and outer sonic points are

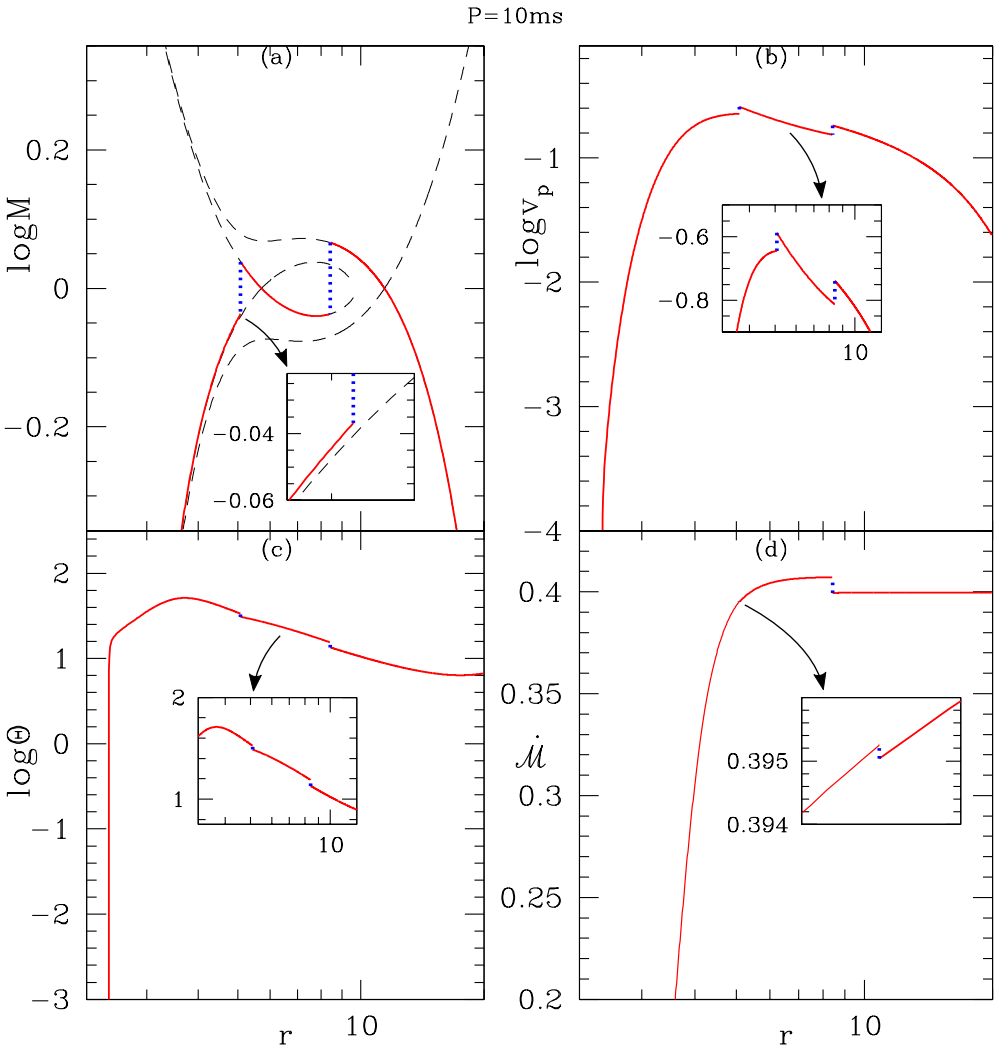

FIGURE 3.5: The accretion solution (f) for $P = 10$ ms. Log of Mach number $\log M$ in panel (a), log of poloidal velocity $\log v_{\rm p}$ in panel (b), log of dimensionless temperature $\log\Theta$ in panel (c) and $\dot{\mathcal{M}}$ in panel (d), as a function of r. The accretion solution is represented by solid red curve, shock by dotted blue curve and other branches of solution by dashed black curve (Singh & Chattopadhyay, 2018a).

X-type and the middle sonic point is spiral type. A flow with $\mathcal{B} \geq \mathcal{B}_{\rm cmax}$ there can be only one inner X-type sonic point. Interestingly, the upper limit of $r_{\rm c}$ is $r_{\rm cl}$, for which the corresponding $\mathcal{B}_{\rm c}$ is $\mathcal{B}_{\rm cl}$, and they are a function of P. For $\mathcal{B}_{\rm cl} \leq \mathcal{B} \leq \mathcal{B}_{\rm cmin}$, only an outer X-type sonic point is possible. In Figs 3.6 (b, d), XS (OL) curve represents the loci of inner sonic points which are X-type, SK (LK) curve represents the loci of middle spiral-type sonic points and KJ curve represents the loci of outer sonic points which are also X-type. This is the famous 'kite-tail' diagram in the energy-entropy space (i. e., $\mathcal{B}_{\rm c}$—$\dot{\mathcal{M}}_{\rm c}$ space). The kite-tail is the enclosed area FSK (or, HLK). Therefore, if $\mathcal{B}_{\rm c}$ lies between the coordinate points J and K, then there would three multiple sonic points. For the range of $\mathcal{B}_{\rm c}$ lies above K, only inner sonic point forms. If $\mathcal{B}_{\rm c}$ lies in the range

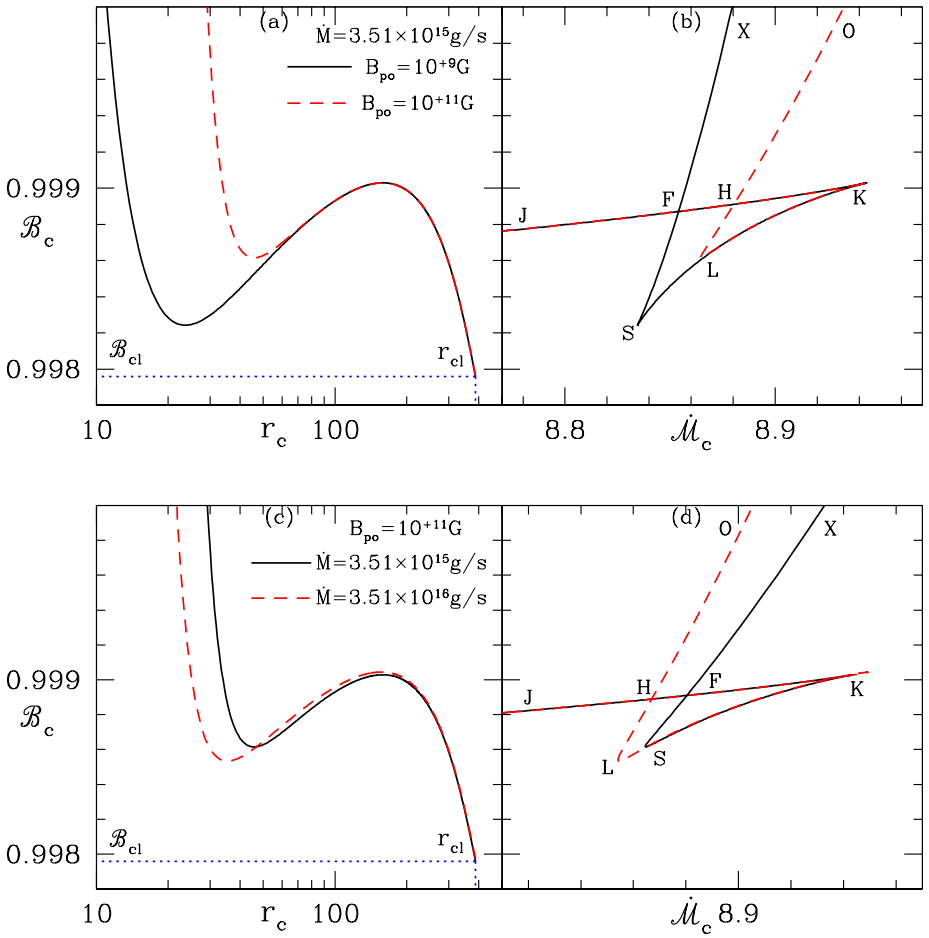

FIGURE 3.6: Critical energy $\mathcal{B}_c$ versus r_c (a, c) and $\mathcal{B}_c$ versus $\dot{\mathcal{M}}_c$ (b, d). In plots (a, b), solid black curve for $B_{p\circ} = 10^9$G and dashed red curve for $B_{p\circ} = 10^{11}$G with $\dot{M} = 3.51 \times 10^{15}$g s^{-1}. In plots (c,d), solid black curve for $\dot{M} = 3.51 \times 10^{15}$g s^{-1} and dashed red curve for $\dot{M} = 3.51 \times 10^{16}$g s^{-1} with $B_{p\circ} = 10^{11}$G. All these plots have, P = 1s and $\xi = 1$ (Singh & Chattopadhyay, 2018b).

between J and S (L), then there are two sonic points, the inner one is X type and the outer one is spiral type. These parameters do not produce global solutions. For $\mathcal{B}_c$ lies below the S (L), no transonic solution is possible. It must be noted that the effect of increasing the surface magnetic field shifts the kite-tail to higher entropy region (FSK $\rightarrow$ HLK), while by increasing the $\dot{M}$, the kite-tail is shifted to the low entropy region. It must also be noted that, if the gravitational interaction was dictated by Newtonian potential, then a $\mathcal{B}_c$—$\dot{\mathcal{M}}_c$ curve will not have XS (OL) branch, in other words, $\mathcal{B}_c$—r_c curves will have a maxima but no minima (see in Appendix A, Fig. A.1 a, b). The importance of $\mathcal{B}_c$—$\dot{\mathcal{M}}_c$ plot, is to look for the possibility of shock jump between the inner and outer sonic points. In the range of MCP region, if the inner sonic point is of higher entropy than that due to the outer sonic point, then there is a possibility of

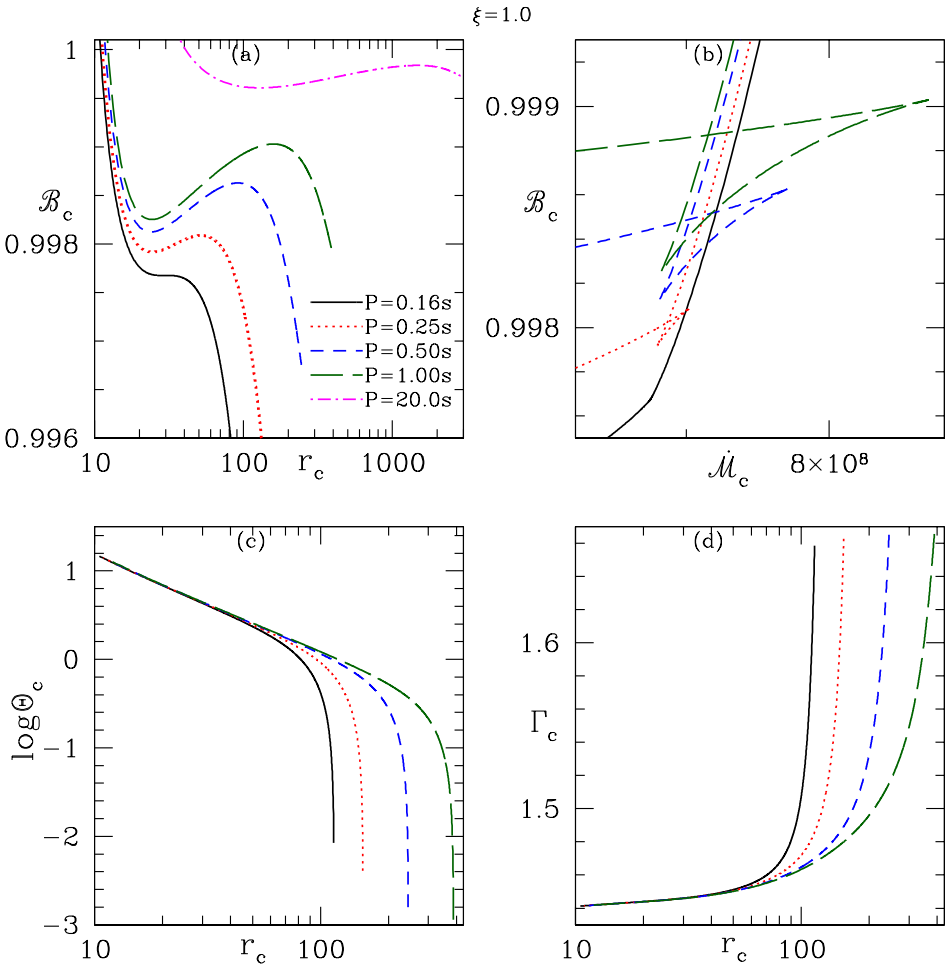

FIGURE 3.7: (a) $\mathcal{B}_c$ as a function of r_c, (b) $\mathcal{B}_c$ versus $\dot{\mathcal{M}}_c$, (c) logΘ_c and (d) (Γ_c) versus r_c for rotation periods $P = 0.16$s (solid, black), 0.25s (dotted, red), 0.5s (dashed, blue), 1.0s (long-dashed, darkgreen) and 20.0 (dash-dotted, magenta). For accretion rates, $\dot{M}_{0.16s} = 0.56 \times 10^{15}$g s^{-1} , $\dot{M}_{0.25s} = 0.88 \times 10^{15}$g s^{-1}, $\dot{M}_{0.5s} = 1.8 \times 10^{15}$g s^{-1}, $\dot{M}_{1.0s} = 3.51 \times 10^{15}$g s^{-1} and $\dot{M}_{20.0s} = 7 \times 10^{16}$g s^{-1}. For all the plots $\xi = 1$ (Singh & Chattopadhyay, 2018b).

shock transition in accretion, within the inner and outer sonic point region.

We know that there is a correlation between rotation period and surface magnetic field of neutron stars (Camilo *et al.*, 1994; Lamb *et al.*, 2005; Pan *et al.*, 2013). Following, Pan *et al.* (2013), we assume a simple relation between surface magnetic field and rotation period (in cgs units) as $B_{\rm po} = 10^{0.583 log{\rm P}+10}$G, and therefore reduce one of the input parameters. By using this relation, we have plotted the $\mathcal{B}_c$ (Fig. 3.7 a), Θ_c (Fig. 3.7 c) and Γ_c (Fig. 3.7 d) versus r_c. Each of the curves were plotted for rotation periods $P = 0.16$s (solid, black), 0.25s (dotted, red), 0.5s (dashed, blue), 1.0s (long-dashed, darkgreen) and 20.0s (dash-dotted, magenta). All the curves are plotted for $\dot{M}_{0.16s} = 0.56 \times 10^{15}$g s^{-1}, $\dot{M}_{0.25s} = 0.88 \times 10^{15}$g s^{-1}, $\dot{M}_{0.5s} = 1.8 \times 10^{15}$g s^{-1},

$\dot{M}_{1.0\mathrm{s}} = 3.51 \times 10^{15}\mathrm{g\ s^{-1}}$, $\dot{M}_{20.0\mathrm{s}} = 7 \times 10^{16}\mathrm{g\ s^{-1}}$ and $\xi = 1$. The $\mathcal{B}_\mathrm{c}$—r_c plot is quite different from pure hydrodynamic case (Kumar & Chattopadhyay, 2013). In general $\mathcal{B}_\mathrm{c}$ has one $\mathcal{B}_\mathrm{cmax}$ and one $\mathcal{B}_\mathrm{cmin}$. Unlike the pure hydrodynamic case, the location of $\mathcal{B}_\mathrm{cmax}$ and $\mathcal{B}_\mathrm{cmin}$ approaches each other, with decreasing P (or increasing rotation). Eventually, the maxima and minima merge at $P = 0.16$s. The dip between a $\mathcal{B}_\mathrm{cmax}$ and $\mathcal{B}_\mathrm{cmin}$ increases as P increases from 0.16s — 1s. However, for a very large value of P ($= 20$s), the dip decreases and finally only monotonic variation of $\mathcal{B}_\mathrm{c}$ with r_c is possible for very low rotation. As is expected Θ_c and Γ_c do not show the presence of extrema. Since Γ is a function of Θ and ξ, Γ_c is not constant. In Fig. 3.7 (b), we plot $\mathcal{B}_\mathrm{c}$ versus $\dot{\mathcal{M}}_\mathrm{c}$ were the curves are for the same values of P as mentioned above. Interestingly, the kite-tail do not form for $P = 0.16$s (solid, black), and starts to form as P is increased. The area encompassed by the kite-tail also increases as $P \to 0.25$—1.0. However, for very high P, the $\mathcal{B}_\mathrm{c}$—$\dot{\mathcal{M}}_\mathrm{c}$ curve do not form a kite tail and it opens up.

One would like to know, for a given ρ_d what is the range of flow parameters ($\mathcal{B}$ and P), for which multiple sonic points are possible and what would be the typical solution for a certain combination of $\mathcal{B}$ and P. In Fig. 3.8 (a), we plot the locus of $\mathcal{B}_\mathrm{cmax}$ (AB) and $\mathcal{B}_\mathrm{cmin}$ (AFE) as a function of P keeping $\rho_\mathrm{d} = 10^{-10}\mathrm{g\ cm^{-3}}$ same, for an electron-proton flow. Therefore, flows with any pair of $\mathcal{B}$, P parameters within the bounded region $BAFE$, would harbour multiple sonic points (two or three). From the $\mathcal{B}_\mathrm{c}$—r_c plots we have seen that there exists a maximum value of sonic points (r_cl), which corresponds to $\mathcal{B}_\mathrm{cl}$ in terms of Bernoulli parameter (marked in Fig. 3.6 a, c). Plotting $\mathcal{B}_\mathrm{cl}$ as a function of P, produces the curve GFD in $\mathcal{B}$—P space (Fig. 3.8 a). Depending on P, $\mathcal{B}_\mathrm{cl} < \mathcal{B}_\mathrm{cmin}$, or may also be $\mathcal{B}_\mathrm{cl} > \mathcal{B}_\mathrm{cmin}$. Flows with parameters within the region DFE (*i.e.,* where, $\mathcal{B}_\mathrm{cl} > \mathcal{B}_\mathrm{cmin}$), have only two sonic points and do not produce global solutions (i. e., solutions connecting r_d and $R_\circ$). Flow parameters from the region bounded by GFE (shaded with slanted curves) can never be transonic. Parameters from the region BAFD (shaded with vertical dashed curves) produce flows containing three sonic points and AC (thin black curve within BAFD region) is the same entropy curve *i.e.,* inner and outer critical point has the same entropy. The thin shaded strip AHIA within the region for three sonic point, harbours second shock at a larger distance from the star's surface. In $\mathcal{B}$—P parameter space, we mark various coordinate points as β ($\mathcal{B} = 0.99902$, $P = 0.1$s), γ ($\mathcal{B} = 0.99902$, $P = 1$s), ϵ ($\mathcal{B} = 0.99877$, $P = 1$s), ι ($\mathcal{B} = 0.9986$, $P = 1$s), λ ($\mathcal{B} = 0.9986$, $P = 3$s), τ ($\mathcal{B} = 0.99814, P = 1$s) and ν ($\mathcal{B} = 0.99814$, $P = 0.1$s). Here accretion rates, $\dot{M}_{0.1\mathrm{s}} = 0.35 \times 10^{15}\mathrm{g\ s^{-1}}$, $\dot{M}_{1.0\mathrm{s}} = 3.51 \times 10^{15}\mathrm{g\ s^{-1}}$ and $\dot{M}_{3.0\mathrm{s}} = 1.1 \times 10^{16}\mathrm{g\ s^{-1}}$. Each such point is the representative of the domain in the parameter space. In Fig. 3.8 (β—ν), starting

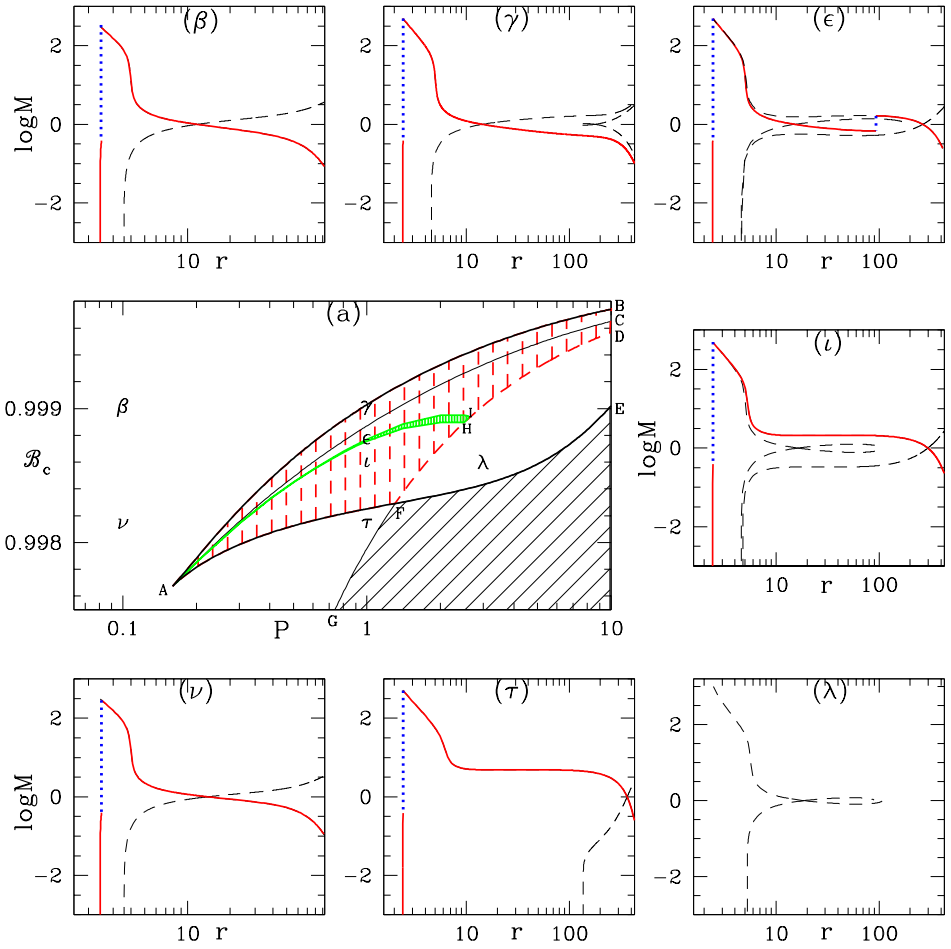

FIGURE 3.8: (a) Parameter space $\mathcal{B}_c - \mathrm{P}$ shows MCP region bounded by BAFE (solid, black). The shaded region CAFDC (dashed, red) produces three r_c. Region DFE produces two r_c. GFD is the curve of $\mathcal{B}_{cl}$ as a function of P. AHIA is the second shock parameter space. The region below GFE (shaded with slanted curves) do not produce transonic solutions. Points, β, ϵ, ι, λ, τ and ν are coordinate points which represents various regions in $\mathcal{B}_c$—$\dot{\mathcal{M}}_c$ space. Corresponding solutions M versus r are plotted in identically named panels (β—ν). Accretion solutions (solid, red), shock transitions (dotted, blue), wind type or multi valued solutions (dashed, black). Here, $\dot{M}_{0.1s} = 0.35 \times 10^{15}$g s^{-1} , $\dot{M}_{1.0s} = 3.51 \times 10^{15}$g s^{-1} and $\dot{M}_{3.0s} = 1.1 \times 10^{16}$g s^{-1} and $\xi = 1$ (Singh & Chattopadhyay, 2018b).

from top left corner in a clock wise manner, we plot the accretion solutions *i.e.,* Mach number $M = v_p/c_s$ as a function of r, corresponding to the coordinate points β—ν in Fig. 3.8 (a). The panels are named similar to the coordinate points in $\mathcal{B}$—P parameter space. The physical accretion solutions (solid, red) connects r_d to $R_\circ$. The dotted blue vertical curves represent shock transition. The dashed (black) curve represent either wind type or multi-valued solutions and cannot be considered proper accretion solutions. In general, the crossing points in the solutions signifies the location of sonic points r_c. For three sonic point region (coordinate points ϵ and ι), the middle spiral type

sonic point is not shown but is typically located near the region where $dM/dr \to 0$ for an upper or lower branch. In order to understand how P and $\mathcal{B}$ affects the solutions, we started with the β point, kept the same $\mathcal{B}$ but increased P to reach to the point γ. Then kept P same and reduced $\mathcal{B}$ to reach ϵ and ι and τ. Then again, kept the same $\mathcal{B}$ as τ, but decreased P to reach to ν, where the P of ν and β are the same. Point β is high energy but low P (*i.e.,* high spin). Higher spin causes the matter to rotate faster, and thus a significant portion of $\mathcal{B}$ is in the form of rotational energy. Therefore, to become transonic, the flow would gain the required magnitude of $v_{\rm p}$, only by going closer to the central object. Increasing the P (*i.e.,* at the point γ) by a moderate amount, reduces the rotation energy and therefore the interplay between gravity and centrifugal terms generate multiple sonic points, although the global solution is still through the inner sonic point. Reducing the specific energy or $\mathcal{B}$ further, makes the rotational and gravity terms comparable enough, not only to cause the accretion flow to pass through the outer sonic point, but can also trigger a shock transition between inner and outer sonic points (ϵ). If the energy is reduced even further, then the flow pressure decreases to the extent, such that, its combined effect with rotational energy is lower than that of gravitational pull and hence in spite of the presence of three sonic points, the second shock do not form. Point λ has the same $\mathcal{B}$ as ι, but has much higher P. Such low rotation, as well as low energy, makes the flow non-transonic, *i.e.,* transonic solution is not global. Point τ is outside the MCP region and of low energy, so there is only one sonic point but far away from the central object. Keeping the same $\mathcal{B}$ but reducing P, causes the sonic point to form closer to the central star. Since the central object has a hard surface, all the global accretion solutions end with a terminating shock.

To understand the physics of accretion onto a magnetized compact object, we should compare the distribution of other flow variables in addition to the spatial distribution of the M. In the left panels of Fig. 3.9, we have plotted the variables log$M$ (Fig. 3.9 a), logΘ (Fig. 3.9 b), Γ (Fig. 3.9 c) and the cooling rates log$Q$, log$Q_{\rm br}$ and log$Q_{\rm cycl}$ (Fig. 3.9 d) for the solution corresponding to point β in $\mathcal{B}$—P space (Fig. 3.8 a). We compared the same flow variables for the solution corresponding to the point ν in (Fig. 3.8 a) in the right panels (Fig. 3.9 e-h). The parameters at point β and ν are differentiated by $\mathcal{B}$ but with the same P. The solution type are therefore similar, except that the sonic point of higher $\mathcal{B}$ solution is located closer to the central object. The terminating shock is located at similar distance in the two cases, and post-shock flow variables as well as, the cooling rates are also similar. The radiative efficiency of the pre-shock flow is around $0.05 - 0.06$ but that of the post- shock flow is about 0.3.

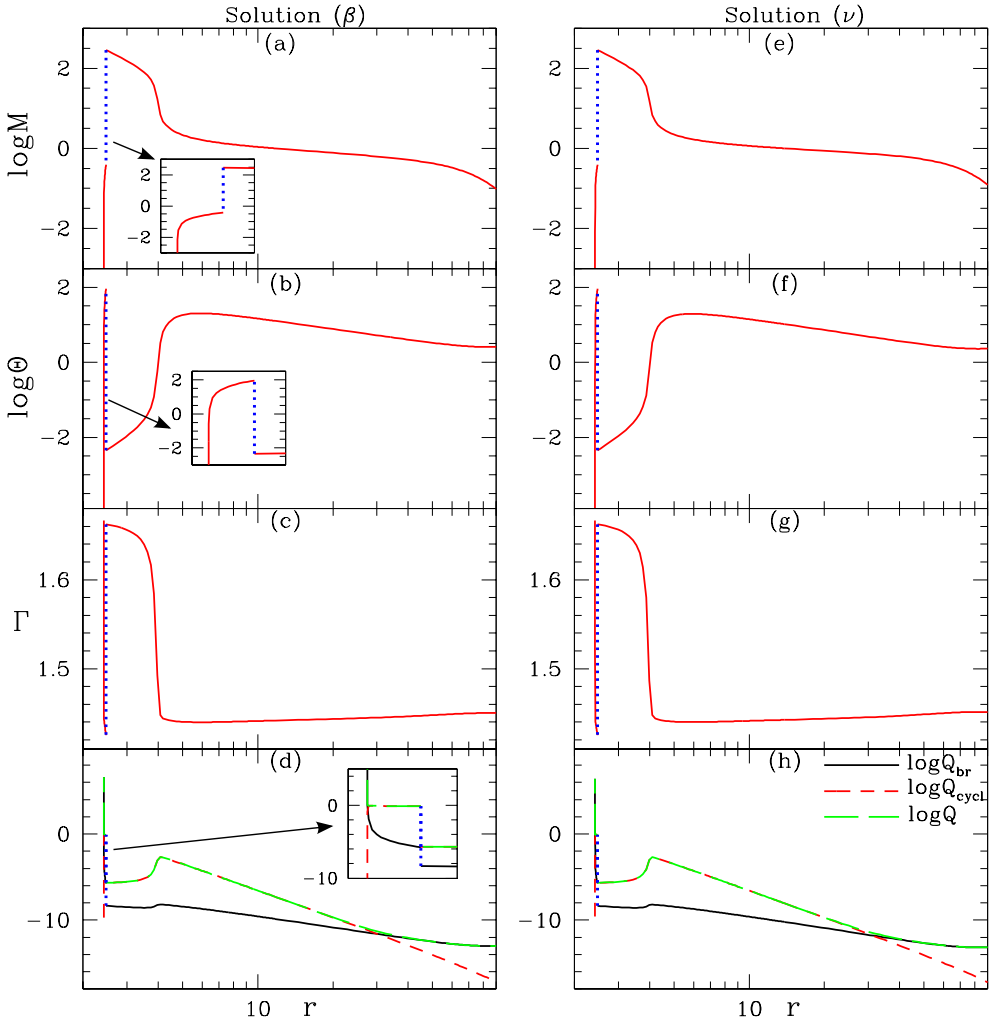

FIGURE 3.9: Variation of log$M$ (a, e); logΘ (b, f); Γ (c, g); total radiative losses in log scale Q (long-dashed, green), bremsstrahlung losses $Q_{\rm br}$ (solid, black) and cyclotron losses $Q_{\rm cycl}$ (dashed, red) in panels (d, h) as a function of r. Comparison of solutions corresponding to coordinate points β (a, b, c, d) and ν (e, f, g, h) of parameter space in Fig. (3.8 a). The inset in panels a, b, d zooms the inner shock region. Here, $\dot{M}_{\beta,\nu} = 0.35 \times 10^{15}$g s^{-1} and $\xi = 1$ (Singh & Chattopadhyay, 2018b).

In Fig. 3.10, we compare flow variables of two solutions in the parameter space range for three sonic points. On the left panels, we plot log$M$ (Fig. 3.10 a), logΘ (Fig. 3.10 b), Γ (Fig. 3.10 c) and the cooling rates log$Q$, log$Q_{\rm br}$ and log$Q_{\rm cycl}$ (Fig. 3.10 d) for the solution corresponding to point ϵ in $\mathcal{B}$—P space (Fig. 3.8 a). This solution harbours two shocks (dotted blue vertical). In the right panels, we plot the same corresponding variables (Fig. 3.10 e-h), but now for the parameters which characterizes coordinate point ι in the parameter space of Fig. 3.8 (a). This set of parameters also produces three sonic points, but shock condition for the second shock is not satisfied. The temperature of the two shocked solutions (corresponding to ϵ) is slightly higher, and the Q is also

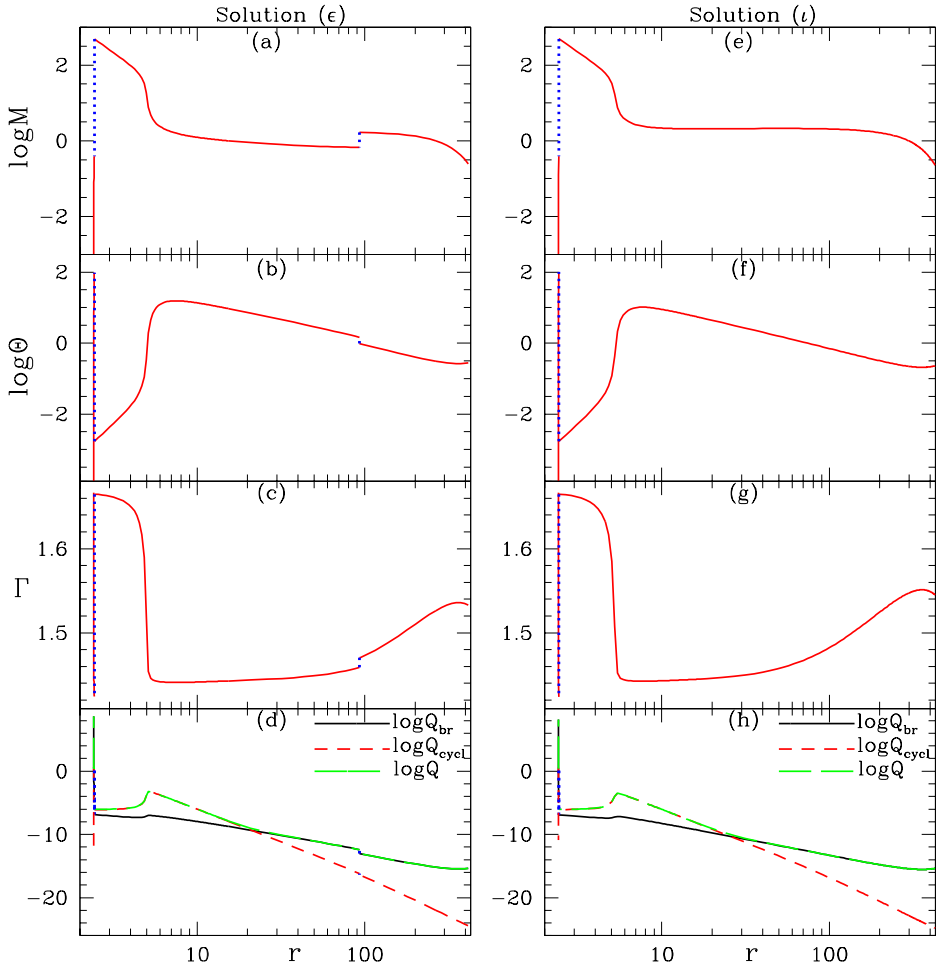

FIGURE 3.10: Variation of log$M$ (a, e); logΘ (b,f); Γ (c,g); total radiative losses in log scale Q (long-dashed, green), bremsstrahlung losses $Q_{\rm br}$ (solid, black) and cyclotron losses $Q_{\rm cycl}$ (dashed, red) in panels (d, h) as a function of r. Comparison of solutions corresponding to coordinate points ϵ (a, b, c, d) and ι (e, f, g, h) of parameter space in Fig. (3.8 a). Here, $\dot{M}_{\epsilon,\iota} = 3.51 \times 10^{15}$g s^{-1} and $\xi = 1$ (Singh & Chattopadhyay, 2018b).

slightly higher than the one shock solution (corresponding to ι). The second shock is noticeably weaker than the terminating shock close to the star's surface.

Solutions with higher and lower rotation periods are also compared for low energy. These solutions are outside the MCP region. In the left panels, we plot log$M$ (Fig. 3.11 a), logΘ (Fig. 3.11 b), Γ (Fig. 3.11 c) and the cooling rates log$Q$, log$Q_{\rm br}$ and log$Q_{\rm cycl}$ (Fig. 3.11 d) for the solution corresponding to point τ in $\mathcal{B}$—P space (Fig. 3.8 a). In the right panels, we plot the same set of variables (Fig. 3.11 e-h), but now for the parameters of the coordinate point ν in the parameter space of Fig. 3.8 (a). The solution with smaller rotation period is colder (τ) than the flow with higher rotation period (ν).

The accretion solutions presented in this study has some interesting features.

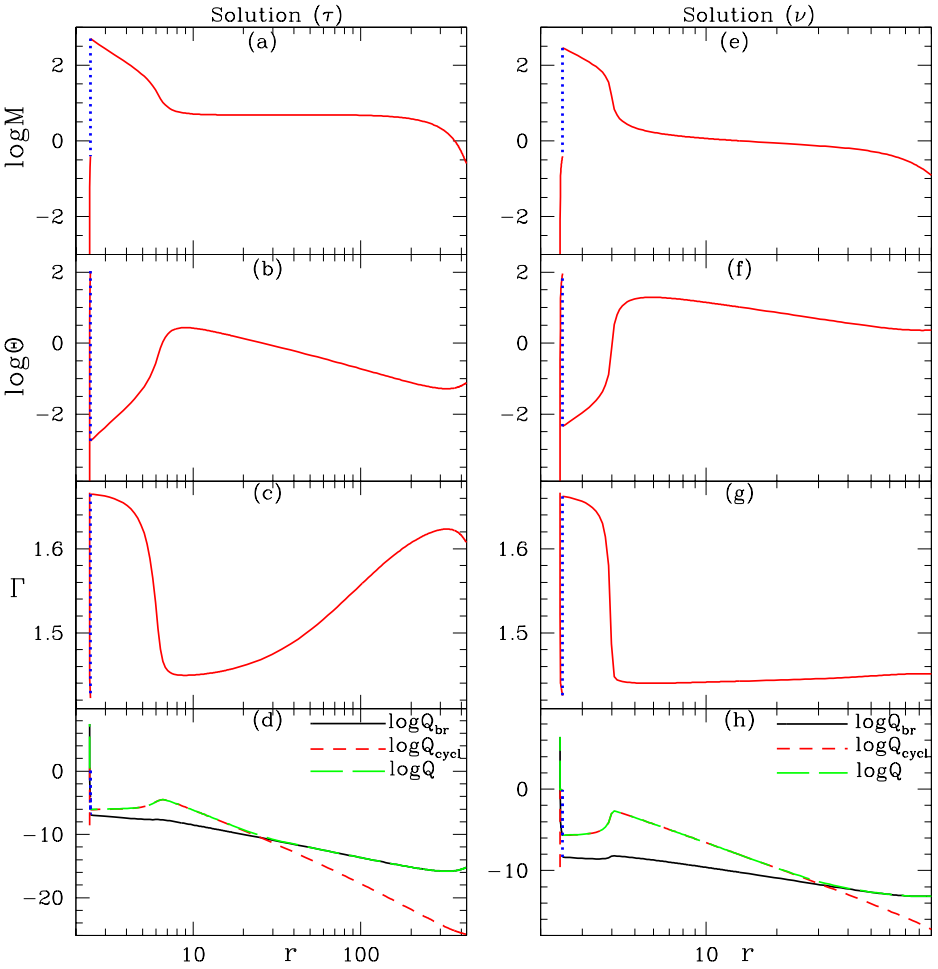

FIGURE 3.11: Variation of log$M$ (a, e); logΘ (b, f); Γ (c, g); total radiative losses in log scale Q (long-dashed, green), bremsstrahlung losses $Q_{\rm br}$ (solid, black) and cyclotron losses $Q_{\rm cycl}$ (dashed, red) in panels (d, h) as a function of r. Comparison of solutions corresponding to coordinate points τ (a, b, c, d) and ν (e, f, g, h) of parameter space in Fig. (3.8 a). Here, $\dot{M}_\tau = 3.51 \times 10^{15}$g s^{-1}, $\dot{M}_\nu = 0.35 \times 10^{15}$g s^{-1} and $\xi = 1$ (Singh & Chattopadhyay, 2018b).

Within a distance of $100r_{\rm g}$ from the star's surface, accretion streamlines are almost radial (*i.e.*, $r\cos(\theta) = r\sin(\theta)$). However, because of the bipolar magnetic field controls the accretion cross-section, therefore close to the stellar surface, the cross-section is smaller than $\sim r^2$. This makes ρ to be larger than a purely radial accretion (*i.e.*, Bondi accretion, Bondi, 1952), and consequently the cooling rates are higher than typical Bondi type accretion. As a consequence of enhanced cooling, the temperature dips in the region within about a $10r_{\rm g}$ and the location of the terminating shock. This dip in Θ is seen all the temperature distributions presented above. In one compares the temperature distribution of a global solution without cooling, such dips are not found (Fig. A.1 c).

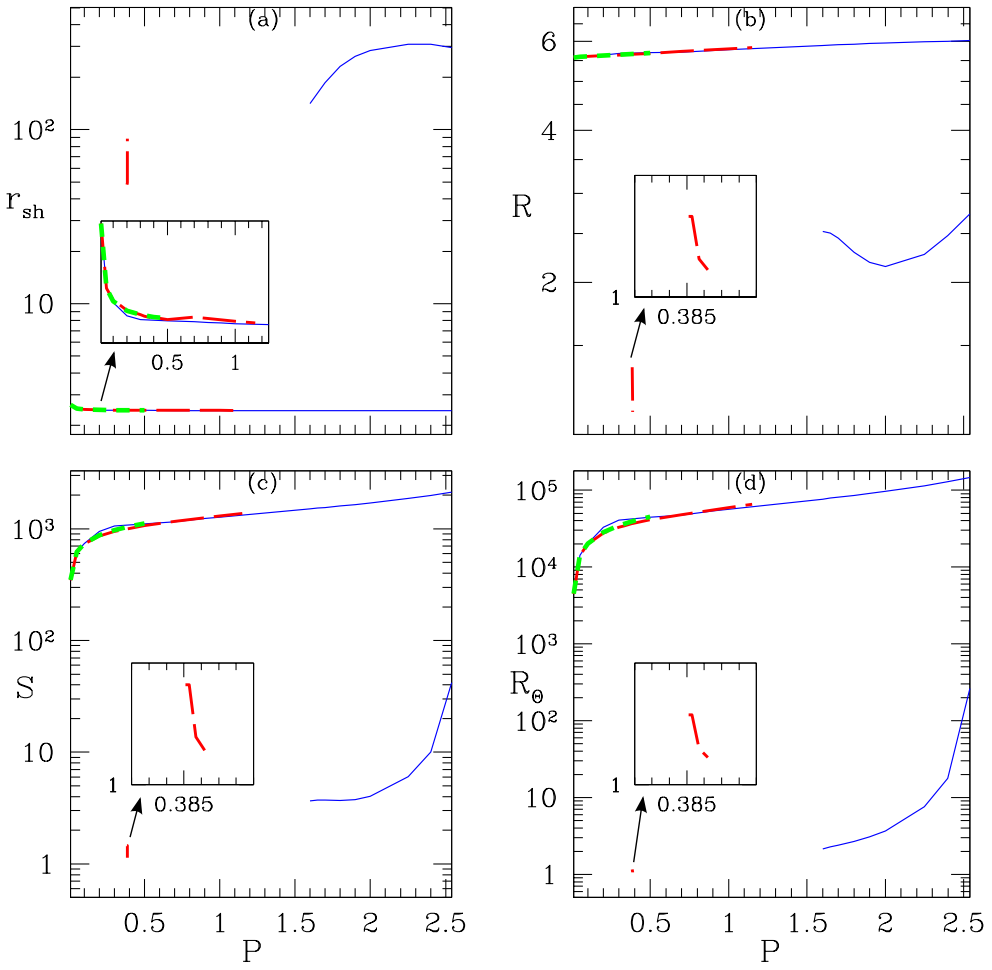

FIGURE 3.12: (a) The shock location $r_{\rm sh}$, (b) compression ratio R, (c) shock strength S and (d) temperature ratio R_Θ are plotted as a function of rotation period P for $\mathcal{B} = 0.99891$ (solid, blue), $\mathcal{B} = 0.9983$ (long-dashed, red) and $\mathcal{B} = 0.997$ (dashed, green). Here, $\dot{M}_{0.01\rm s} = 0.35 \times 10^{14}$g s^{-1} – $\dot{M}_{2.5\rm s} = 9 \times 10^{15}$g s^{-1} and $\xi = 1$ (Singh & Chattopadhyay, 2018b).

It is clear that for a given $\rho_{\rm d}$, the properties of the accretion is determined by $\mathcal{B}$ and P. Therefore the shock properties should also have some dependence on these two flow parameters. In Fig. 3.12 (a), $r_{\rm sh}$ is plotted as a function of P. The inner terminating shock is almost horizontal over-plotted curves close to the star's surface around $2-3r_{\rm g}$ in the panel. The inner shock decreases very weakly with the increase of P and has almost no dependence on $\mathcal{B}$. The second shock is represented by the curves at few $\times 10$—$100r_{\rm g}$. In Fig. 3.12 (b, c, d), the corresponding compression ratio $R = \rho_+/\rho_-$, shock strength $S = M_-/M_+$ and the temperature ratio $\mathrm{R}_\Theta = \Theta_+/\Theta_-$ respectively, are plotted as a function of P. Each curve is for $\mathcal{B} = 0.99891$ (solid, blue), $\mathcal{B} = 0.9983$ (long-dashed, red) and $\mathcal{B} = 0.997$ (dashed, green). The inner shock locations for various $\mathcal{B}$ overplot on each other, and therefore, are zoomed in the inset of panel Fig. 3.12

(a). Since the parameter space for transonic solutions are limited by the GFHD curve (Fig. 3.8 a) *i.e.,* whole range of rotation period is not available for all energy ($\mathcal{B}$) values. Therefore, the inner shock is limited for $\mathcal{B} = 0.997$ (dashed, green). No second shock is found for this energy parameter for any value of P. For a little higher $\mathcal{B} = 0.9983$ for a (long-dashed, red), the inner shock is obtained for $P \lesssim 1.1$ (see the inset). Second shock is obtained for a very short range of $P \sim 0.3851 - 0.3862$s and the location range of the second shock is $48.3 \leq r_{\rm sh} \leq 88.5$. For $\mathcal{B} = 0.99891$ the inner shock exist for a range of $P \lesssim 2.54$ (solid, blue). The second shock is in the limited range of $1.6 \lesssim P \lesssim 2.54$, and the second shock is also located far away from the star's surface $140 \leq r_{\rm sh} \leq 295$. The compression ratio R (Fig. 3.12 b) of the inner shock is very high $R \sim 6$ and is almost independent of $\mathcal{B}$ but is very weakly dependent on P. The R of the outer shock is $\mathcal{B}$ dependent. $R \lesssim 1.4$ (long-dashed, red) for $\mathcal{B} = 0.9983$ and $2 \lesssim R \lesssim 3$ (solid, blue) for $\mathcal{B} = 0.99891$. In the inset R for $\mathcal{B} = 0.9983$ is zoomed for second shock. The shock strength S (Fig. 3.12 c) and temperature ratio R_Θ (Fig. 3.12 d) plots also show that the inner shock to be very strong and depend marginally on $\mathcal{B}$, but the outer shocks do depend on $\mathcal{B}$ and are weak to moderate in strength. The insets in both the panels zoom the outer shocks for $\mathcal{B} = 0.9983$. We have also calculated post luminosity and found that the order of magnitude varies with the rotation period. Therefore, the post-shock luminosity at inner shock is, $\mathcal{L}_{0.01\rm s} \sim 10^{30}$erg s^{-1} to $\mathcal{L}_{2.5\rm s} \sim 10^{35}$erg s^{-1} and at the outer shock is $\mathcal{L} \sim 10^{24-26}$erg s^{-1}.

In Fig. 3.13 (a-d), all the shock variables are plotted for $P = 0.1$s (solid, blue), $P = 0.5$s (long-dashed, red) and $P = 2.0$s (dashed, green). In Fig. 3.13 (a), $r_{\rm sh}$ is plotted as a function of $\mathcal{B}$. For $P = 0.1$s (solid, blue) the shock is formed only close to the star's surface and for all values of $\mathcal{B}$. For $P = 0.5$s (long-dashed, red), the inner terminating shock forms for all values of $\mathcal{B}$, but at $0.998447 \lesssim \mathcal{B} \lesssim 0.9984497$, outer shock forms in a limited range $55.6 \lesssim r_{\rm sh} \lesssim 112$. For $P = 2$s (dashed, green) inner shock forms for $\mathcal{B} \gtrsim 0.99872$. Outer shock also forms in the range $0.998896 \lesssim \mathcal{B} \lesssim 0.998949$ and located in a range from $166.6 \lesssim r_{\rm sh} \lesssim 323$. Although all the inner shock almost overlaps (lower almost horizontal curves), the outer shock locations are perceptible. In Fig. 3.13 (b), R is plotted as a function of $\mathcal{B}$. $R \lesssim 6$ for the inner shock (upper curves) and all the curves for P overlaps. The compression ratio of the outer shock (lower slanted curves) ranges from being weak to moderate. The shock strength S (upper curves in Fig. 3.13 c) for the inner shock depends significantly on P and are quite high. While the S parameter for outer shock is comparatively much weaker and are zoomed in the two inset panels. The R_Θ (upper curves in Fig. 3.13 d) parameter for the inner

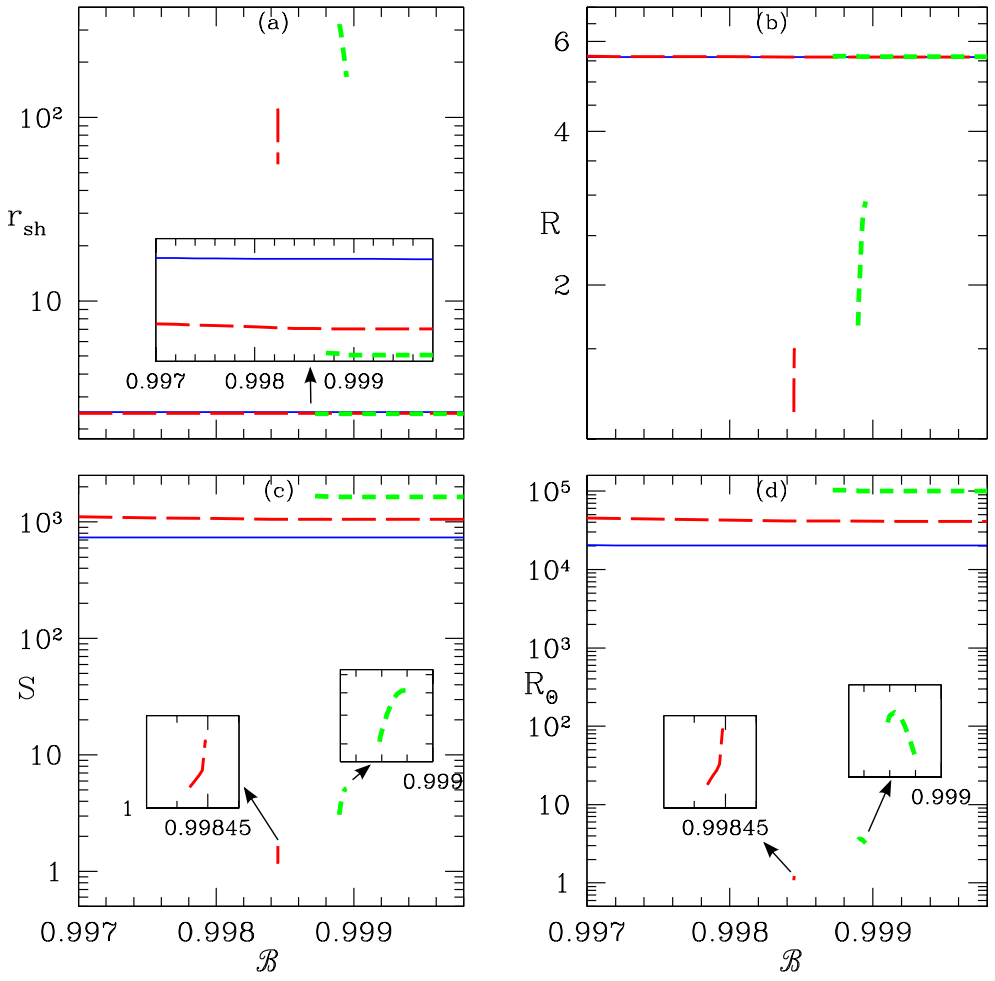

FIGURE 3.13: (a) The shock location $r_{\rm sh}$, (b) compression ratio R, (c) shock strength S and (d) temperature ratio (R_Θ) across the shock are plotted as a function of $\mathcal{B}$ for three rotation periods $P = 0.1$s (solid, blue), $P = 0.5$s (long-dashed, red) and $P = 2.0$s (dashed, green). The inset in panel (a) zooms the inner shock locations. There are two insets in panels (c & d), which zooms the outer shock quantities. Here, $\dot{M}_{0.1s} = 0.35 \times 10^{15}$g s^{-1}, $\dot{M}_{0.5s} = 1.8 \times 10^{15}$g s^{-1}, $\dot{M}_{2.0s} = 7 \times 10^{15}$g s^{-1} and $\xi = 1$ (Singh & Chattopadhyay, 2018b).

shock is higher for higher P and completely dominates the outer shocks (zoomed in the inset panels in Fig. 3.13 d). The inner shocks are so overwhelmingly strong that the signatures of the outer shock may not be significant, although might contribute dynamically if the outer shock is made unstable by some process. In this case, post-shock luminosity at inner shock does not change significantly with energy and has an order of magnitude is, $\mathcal{L}_{0.1s} \sim 10^{32}$erg s^{-1}, $\mathcal{L}_{0.5s} \sim 8 \times 10^{33}$erg s^{-1}, $\mathcal{L}_{2.0s} \sim 10^{35}$erg s^{-1} and at outer shock the order is $\mathcal{L}_{0.5s} \sim 5 \times 10^{25}$erg s^{-1}, $\mathcal{L}_{2.0s} \sim 10^{27}$erg s^{-1}.

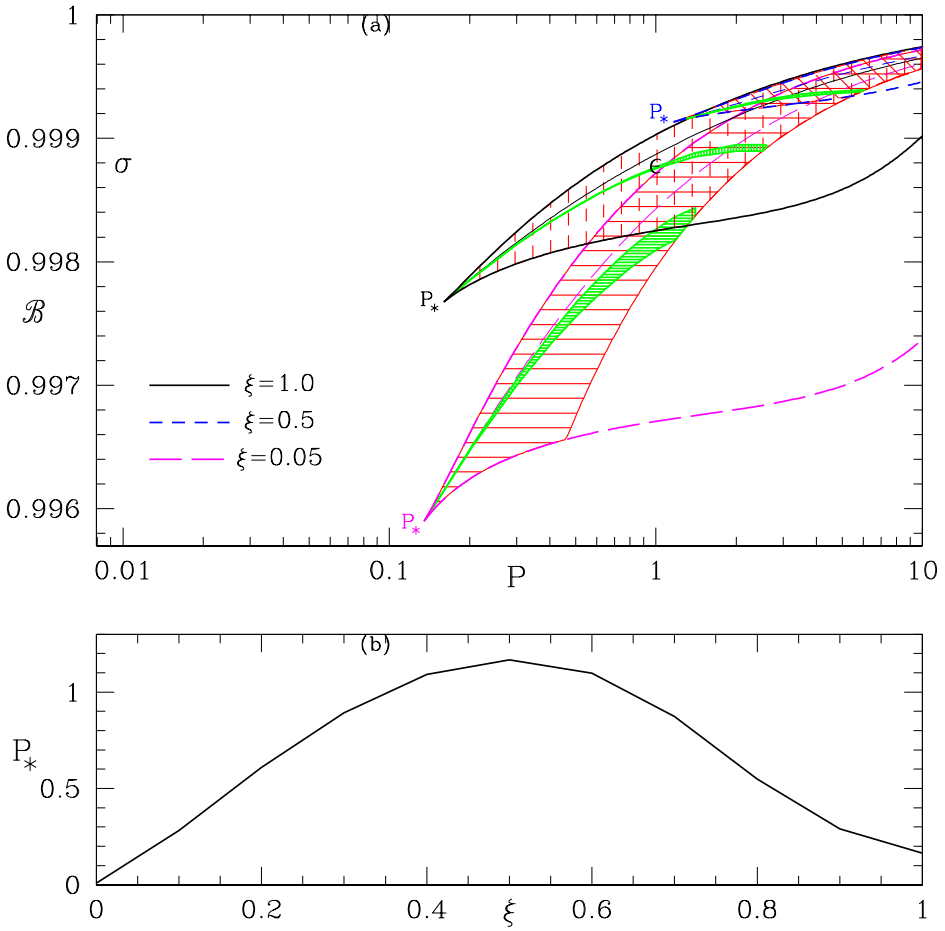

FIGURE 3.14: (a) $\mathcal{B}$—P parameter space, in which MCP region is demarcated for $\xi = 0.05$ (long-dashed magenta), $\xi = 0.5$ (dashed, blue) and $\xi = 1.0$ (solid, black). P_* is the minimum P beyond which MCP is possible. Two coordinate points are marked as 'σ' and 'ϵ', the values of $\mathcal{B}$, P corresponding to these points are used to obtain accretion solutions in Figs. 3.15 and 3.16, respectively. (b) P_* plotted as a function of ξ. Here, $\dot{M}_{0.01\mathrm{s}} = 0.35 \times 10^{14}\mathrm{g\ s^{-1}} - \dot{M}_{10.0\mathrm{s}} = 3.5 \times 10^{16}\mathrm{g\ s^{-1}}$ (Singh & Chattopadhyay, 2018b).

3.4.3.1 Effect of ξ

In Fig. 3.14 (a), we plot the MCP region in the $\mathcal{B}$—P parameter space for accretion rate $\dot{M}_{0.01\mathrm{s}} = 0.35 \times 10^{14}\mathrm{g\ s^{-1}} - \dot{M}_{10.0\mathrm{s}} = 3.5 \times 10^{16}\mathrm{g\ s^{-1}}$, but for different ξ. Each bounded region which represents MCP are for $\xi = 1.0$ (solid, black), $\xi = 0.5$ (dashed, blue) and $\xi = 0.05$ (long-dashed magenta). There is a certain value of rotation period (say P_*) below which MCP is not possible. Small rotation period (P $< P_*$) has small r_{co} or r_d. Therefore, gravity is very strong in the funnel for an accretion system having small P. If the gravity is too strong then, neither MCP nor, second shock forms. However, the MCP region (area under the bounded curves) depends significantly on ξ. The area under the curve shrinks for $0.5 < \xi \leq 1$ and then starts to increase. In fact for lepton

dominated flow ($\xi \sim 0.05$) the MCP region is quite significant. This is quite different from a purely hydrodynamic case. The strong magnetic field criteria increases angular momentum at larger r. Therefore, in spite of the thermal energy of the small ξ flow is mostly non-relativistic, but still, the angular momentum is large enough at large r to modify gravity and produce multiple sonic points. In Fig. 3.13 (b), we have plotted P_* versus composition parameter ξ. In this figure, we can see that P_* starts with minimum value at $\xi = 0.0$ then becomes maximum at $\xi \sim 0.5$. However if ξ further increases, P_* starts decreasing and reaches its value at $\xi = 1.0$. Two coordinate points named as σ ($\mathcal{B} = 0.99877;\ P = 0.01$s) and ϵ ($\mathcal{B} = 0.99877;\ P = 1$s) are marked in the $\mathcal{B}$—P, chosen to consider high and moderate rotation period of central stars. It may be noted that the ϵ point is same as the coordinate point identically named in Fig. 3.8 (a). Accretion solutions corresponding to these points are compared for different ξ in Figs. 3.15 & 3.16.

In Fig. 3.15 (a-i), we have compared flow variables corresponding to ϵ in Fig. 3.14 (a), *i.e.*, for $\mathcal{B} = 0.99877$ and $P = 1.0$s. Each column represents solutions of flows for the same values of $\mathcal{B}$ and P, but of different composition $\xi = 1.0$ (Fig. 3.15 a-c), $\xi = 0.5$ (Fig. 3.15 d-f) and $\xi = 0.05$ (Fig. 3.15 g-i). In order to compare the solutions of different ξ, in each row we have plotted log$M$ (Fig. 3.15 a, d, g), logΘ (Fig. 3.15 b, e, h) and Γ (Fig. 3.15 c, f, i). The same flow parameters $\mathcal{B}$, P produces two shocks for electron-proton ($\xi = 1.0$) flow, however, produces only the terminating shock for flows with $\xi = 0.5$ and $\xi = 0.05$. It is clear from Fig. 3.14 (a) that ϵ is in the zone which produces multiple shocks for $\xi = 1.0$, but not for $\xi = 0.5$ and $\xi = 0.05$. However, for $\xi = 0.5$, the point ϵ is below the MCP region, but is above the MCP region for $\xi = 0.05$. The sonic points for $\xi = 0.05$ is closer to the star's surface than that for $\xi = 0.5$. The temperature distribution confirms conclusions from earlier hydrodynamic studies of multispecies flow (Chattopadhyay & Ryu, 2009; Kumar & Chattopadhyay, 2013, 2014; Chattopadhyay & Kumar, 2016; Kumar & Chattopadhyay, 2017), *i.e.*, and electron-proton flow is hotter than flows dominated by leptons. However, although the temperature of the flow with $\xi = 1.0$ is more than an order of magnitude higher than the flow with $\xi = 0.05$, but the adiabatic index distribution shows that thermally, $\xi = 0.05$ flow is more relativistic than the electron-proton flow at around $r \sim 10 r_{\rm g}$.

In Fig. 3.16 (a-i), we compare the flow variables for the same $\mathcal{B}$ as the previous figure but for higher rotation period $P = 0.01$s and is marked in the $\mathcal{B}$—P parameter space as the coordinate point σ (Fig. 3.14 a). Similar to the previous figure, we plot log$M$ (Fig. 3.16 a, d, g), logΘ (Fig. 3.16 b, e, h) and Γ (Fig. 3.16 c, f, i) as a function of

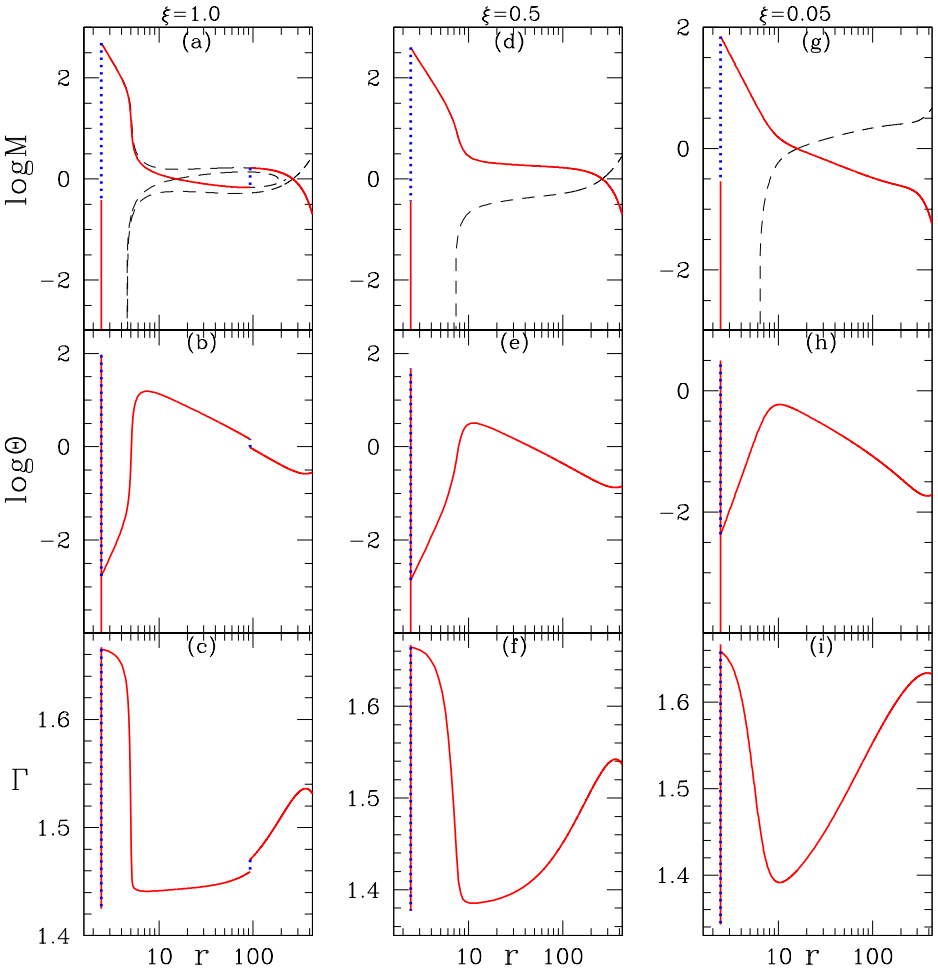

FIGURE 3.15: Variation of log$M$ (a, d, g), logΘ (b, e, h) and Γ (c, f, i) as a function of r. Each column of panels represent flow characterized by $\xi = 1.0$ (a-c), $\xi = 0.5$ (d-f) and $\xi = 0.05$ (g-i). The physical accretion solutions are solid curves with the shock jumps depicted as dotted blue vertical curves. The crossing of the dashed and the solid curves indicate the position of the sonic points. Here $\dot{M} = 3.51 \times 10^{15}$g s^{-1}. The solutions correspond to point ϵ or $\mathcal{B} = 0.99877$ and $P = 1$s in the $\mathcal{B}$—P parameter space of Fig. 3.14 (a) (Singh & Chattopadhyay, 2018b).

r. Panels in each column presents distribution of various flow variables for the same $\mathcal{B}$ and P but for different flow composition $\xi = 1.0$ (Fig. 3.16 a-c), $\xi = 0.5$ (Fig. 3.16 d-f) and $\xi = 0.05$ (Fig. 3.16 g-i). For the parameters of σ, there are no MCP for any ξ and consequently only forms the terminating shock close to the star's surface. However, the solutions differ from each other depending on ξ. Apart from the difference in location of the sonic points (crossing between solid and dashed curves), the size of the post-shock region for $\xi = 1.0$ is larger than lepton dominated flows. The temperature distribution for the electron-proton flow is higher, but because of the enhanced inertia of larger fraction of protons, Γ shows that lepton dominated flow are thermally more relativistic than the electron-proton flow.

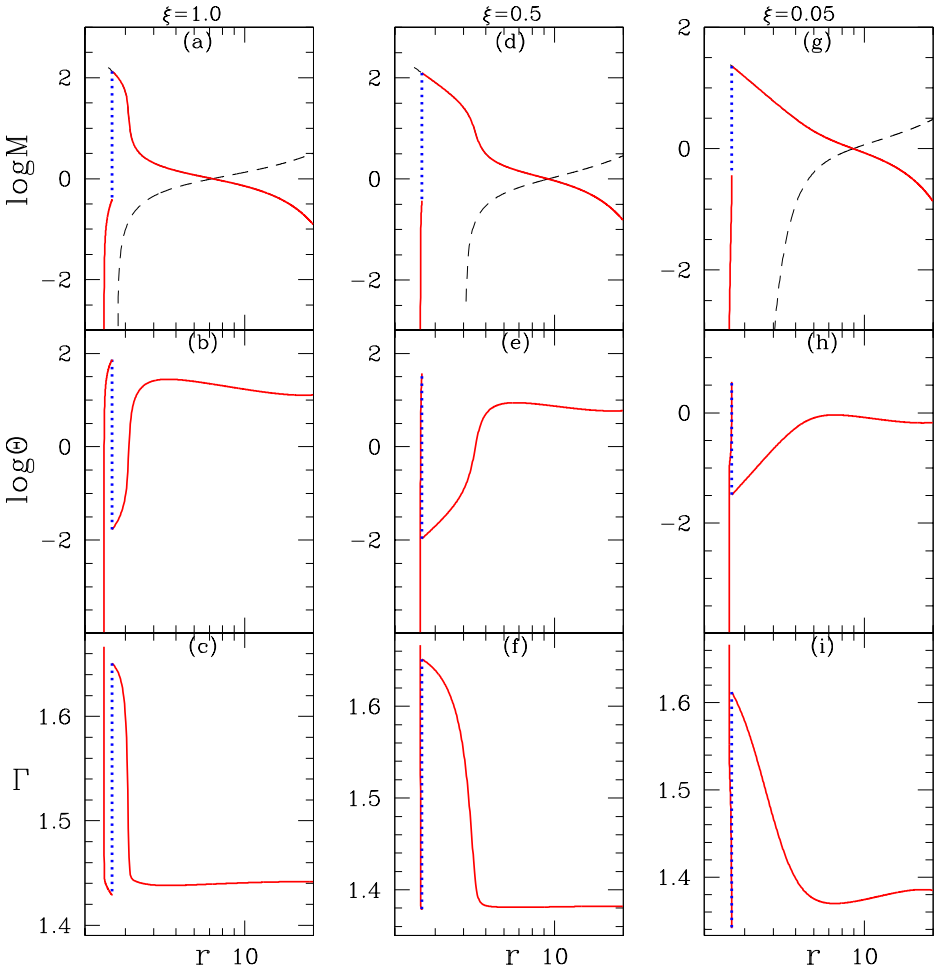

FIGURE 3.16: Variation of log$M$ (a, d, g), logΘ (b, e, h) and Γ (c, f, i) as a function of r. Each column of panels represent flow characterized by $\xi = 1.0$ (a-c), $\xi = 0.5$ (d-f) and $\xi = 0.05$ (g-i). The physical accretion solutions are solid curves with the shock jumps depicted as dotted blue vertical curves. Here $\dot{M} = 0.35 \times 10^{14}$g s^{-1}. The solutions correspond to point σ or $\mathcal{B} = 0.99877$ and $P = 0.01$s in the $\mathcal{B}$—P parameter space of Fig. 3.14 (a) (Singh & Chattopadhyay, 2018b).

3.4.3.2 White Dwarf type compact object

Among the three accepted versions of compact objects like a black hole, NS or a WD, all have very strong gravity, although black holes have a very unique property of having no hard boundary and are only screened from the outside universe by one way, imaginary surface called the event horizon. Since we are only concentrating on magnetized accretion flow onto compact objects with a hard surface, therefore black holes are beyond the scope of this analysis. The related defining property that separates gravitation interaction that these objects impose on the surrounding matter is the compactness parameter or $M_\circ/R_\circ$. In geometric units, the compactness parameter for black holes $M_\circ/R_\circ = 1$; for NS it is $0.5 \lesssim M_\circ/R_\circ \lesssim 0.66$ and for WDs $M_\circ/R_\circ \sim$ few $\times 10^{-4}$. Larger

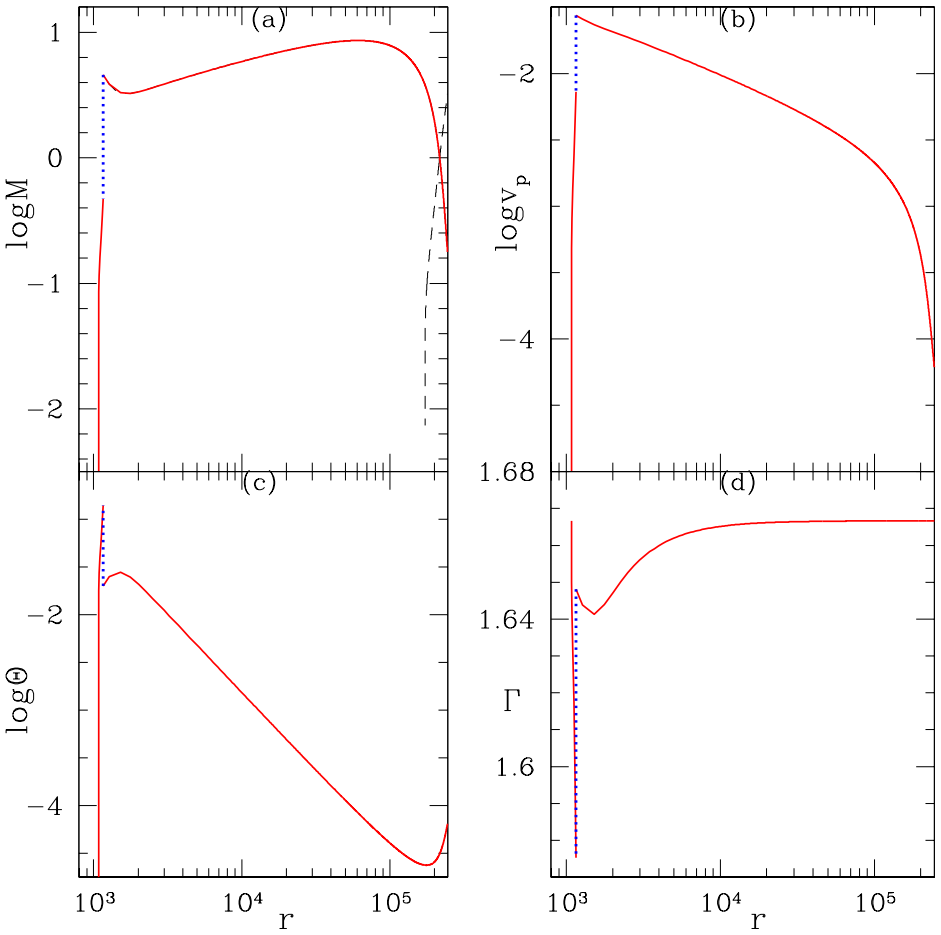

FIGURE 3.17: Magnetized accretion solution for WD. Plotted the variation of log$M$ (a), log$v_{\rm p}$ (b), logΘ (c) and Γ (d) as a function of r. The physical accretion solutions (solid, red), shock jumps (dotted, blue vertical curves) and wind type solutions (dashed, black) are shown. Sonic point is at the crossing of accretion and wind type solutions. Central object is WD with $M_\circ = 1.2M_\odot$, $R_\circ = 3.8 \times 10^8$cm, $B_{\rm p\circ} = 3 \times 10^7$G and $P = 12150$s. The solutions corresponds to $\mathcal{B} = 0.9999968$ and $\dot{M} = 5.54 \times 10^{15}$g s^{-1} (Singh & Chattopadhyay, 2018b).

the compactness parameter, *i.e.*, larger the mass packed in a finite volume, stronger is the gravity of the object, with black holes having the strongest gravity. Up to now, we have used compactness ratio in tune with the description of NS and all our solutions above can be thought to represent accreting NS cases. In the following, we change the central star properties to mimic accretion processes of a WD and still using the same methodology of solution.

The mass and radius of central star used to mimic a WD is $M_\circ = 1.2M_\odot$, $R_\circ = 3.8 \times 10^8$cm, the surface magnetic field as $B_{\rm p\circ} = 3 \times 10^7$G and the rotation period $P = 12150$s. It is quite clear that a WD has quite low compactness ratio, infact in units of $r_{\rm g}$, the radius of the WD is $R_\circ = 1.072 \times 10^3 r_{\rm g}$. Given the central star's parameters as assumed

above, we need to supply two parameters to $\mathcal{B} = 0.9999968$ and $\dot{M} = 5.54 \times 10^{15}$g s^{-1} we can obtain the accretion solution. In Fig. 3.17 (a), we plot log$M$ as a function of r. The solid (red) curve represents accretion solution, the dotted blue vertical curve represent the shock transition. The dashed curve is the wind type solution (obtained with wind type boundary conditions) and its crossing with the accretion branch determines the location of the sonic point. The accretion column terminates on the star's surface after suffering the terminating shock. Other flow variables of the accretion column are log$v_{\rm p}$ (Fig. 3.17 b), logΘ (Fig. 3.17 c) and Γ (Fig. 3.17 d). Since the WD accretion does not achieve relativistic temperature so we only considered electron-proton flow. The shock location obtained from our calculations is $r_{\rm sh} = 1.1577 \times 10^3 r_{\rm g}$, the post-shock temperature is $\sim 8.313 \times 10^8$K and the post-shock density is $\sim 4.672 \times 10^{-9}$g cm^{-3}. Therefore the shock height comes out to be $0.08R_\circ$ for the WD. Observational studies are in general agreement with the numbers generated by us (Rana *et al.*, 2005). A more exact agreement can be obtained if all the dissipative processes, accretion rate and the Bernoulli integral are chosen properly.

3.5 Discussion and Concluding Remarks

We have studied the magnetized accretion solution onto a compact object which has a strong magnetic field and hard surface. Since the gravity of a compact object is stronger than Newtonian potential, we used pseudo-Newtonian potential (PWP). We first study the magnetized accretion with fixed EoS to develop the mathematical and numerical methodology to find the solution with the inclusion of cooling *e.g.,* bremsstrahlung and cyclotron. However, as the accretion flow traverses the large distance, in the course of which the temperature varies two to four orders of magnitude. So, we also studied the magnetized accretion with temperature dependent Γ or CR EoS to describe the fluid. The advantage of PWP is that at large distance it is essentially Newtonian, and the advantage of CR EoS is that, it takes care of the adiabatic index at all temperatures and at temperature 10^7K, it behaves like fixed adiabatic index EoS with $\Gamma \sim 5/3$ (Chattopadhyay & Ryu, 2009). Therefore, the mathematical tools we have employed will enable us to go from weak gravity to a stronger one, as well as from low to very high temperatures. We have compared the sonic point properties of accretion flows under the influence of Newtonian gravity and PW gravity using fixed adiabatic index EoS (subsection 3.4.1) and CR EoS (Appendix A). Since Newtonian gravity do not allow the formation of inner sonic point, therefore in presence of rotation all accretion solutions

possess two sonic points, the outer X-type and the inner O-type (without dissipation). As a result, all accretion solutions would fold back in the form of an α (see discussions in Chattopadhyay & Kumar, 2016; Kumar & Chattopadhyay, 2017). Only some of the $\mathcal{B}$ and P combinations would allow the turning radius to be less than the star radius (*e.g.,* Fig. 4 a in Koldoba *et al.*, 2002). Only $\mathcal{B} < 0.9981$ (without the rest mass energy $\mathcal{B} < -0.0019$) corresponds to a 'global' solution *i.e.,* connect $r_{\rm d}$ and $R_{\rm c}$. However, in PW gravity *i.e.,* a stronger gravity, global solutions are available for all available $\mathcal{B} > \mathcal{B}_{\rm cl}$.

The velocity of the accreting matter is supersonic close to the star's surface, but for a stable accretion solution it has to either stop or co-rotate with the star on its surface. Since the post-shock density and temperature is high, as well as, the presence of the magnetic field, cooling processes dominate and helps to minimize the infall velocity of the accretion flow on the star's surface. Therefore, in this analysis, all the accretion solution ends on the star's surface with a terminating shock very close to the star's surface, unlike Koldoba *et al.* (2002) and Karino & Kino (2008). The terminating shocks are very strong (Figs. 3.12, 3.13) and therefore likely to contribute significantly to the total electromagnetic output of the system (Figs. 3.9 d,h; 3.10 d,f; 3.11 d,h).

We have calculated the total luminosity for different solutions and found that order of magnitude is 10^{34-36}erg s^{-1}. Also, the optical depth for different solutions which remains less ~ 0.1. Therefore, plasma is optically thin and radiations from cooling processes can escape (Saxton *et al.* (1998), and Busschaert *et al.* (2015)) and flow gets cooled. The effect of cooling is observed in the temperature distribution of the flow, where enhanced cooling reduces the temperature of the flow before the terminating shock, as well as, the post-shock flow just above the star's surface. There are no such dips in temperature in the accretion flow if cooling processes are ignored (Figs. 3.2, A.1 c).

Stronger gravity of PW potential causes the formation of MCP (multiple critical point) region in the $\mathcal{B}$—P parameter space. This produces various accretion solutions, some of which admits a second shock. While the terminating strong shocks, which accompanies all global accretion solutions, are very strong $R \sim 6$ and close to the star's surface $r_{\rm sh} \rightarrow 2.5 - 3r_{\rm g}$, but second shocks are weaker < 3 and located much further out $r_{\rm sh} \gtrsim$ few times $10r_{\rm g}$. The electromagnetic signature of this second shock is likely to be washed out in the steady state scenario, but shock oscillation induced by various dissipation processes might give rise to many interesting phenomena. The most interesting fact is that the two post-shock regions are separated by a supersonic region, therefore the second shock is acoustically separated from the terminating shock

closer to the star's surface, although the oscillations in the second shock in principle can make the terminating shock time dependent. How this will pan out in terms of observation, needs to be determined through numerical simulations and is currently beyond the scope of this study.

Although there is a general agreement on various features with hydrodynamic black hole accretion solutions, there are some significant differences as well. The cross-sectional area of the accretion is smaller than a typical $\sim r^2$ cross section expected in the inner region of a black hole accretion disc. Therefore, the density of matter near a NS or WD surface is much larger than the one near the black hole horizon. As a result, bremsstrahlung, cyclotron and other cooling processes are much more important near the star's surface than a black hole.

Another important difference is the sonic point properties. In the hydrodynamic case, $r_{\rm c}$ can be as large as possible and for $r_{\rm c} \rightarrow$ large, $\mathcal{B}_{\rm c} \rightarrow 1$. However, in the present case, maximum of $r_{\rm c}$ possible is $r_{\rm cl}$ and the corresponding energy is $\mathcal{B}_{\rm cl}$. So, in the case of purely hydrodynamic flow, X-type sonic points for global solutions are obtained if $\mathcal{B} > 1$, but here X-type sonic points related to a global solution are obtained if $\mathcal{B} > \mathcal{B}_{\rm cl}$. Since CR EoS also contains the information of composition, therefore we also studied how the proton content affects the solution. In the purely hydrodynamic case, the proton poor flow is thermally non-relativistic and the MCP region is small and vanishes for $\xi = 0$. But in the present case, the MCP region is large for proton poor flow. This is because, the strong magnetic field decreases angular momentum close to the star, but increases at a larger distance. So whatever may be the thermal state of the flow, centrifugal interaction alone is important enough at large distance to modify gravity and produce multiple sonic points. So even for $\xi \sim 0$ flow, multiple sonic points, and second shocks are possible in the presence of the magnetic field.

In conclusion, we obtained solutions of the accretion flow onto a magnetized compact star, in presence of bremsstrahlung and cyclotron cooling, in the strong magnetic field approximation. We also used the variable Γ EoS to describe the fluid. All global accretion solution forms a very strong terminating shock near the star surface. This terminating shock also contributes significantly to the total radiation budget of these accretion systems. There is also a possibility of forming multiple sonic points in a limited range of flow parameters. A weak to moderately strong shock at a distance of about hundred $r_{\rm g}$ is formed for flows characterized by the parameters from this limited range of parameters. Accretion flow with two shocks are a class of interesting solutions and its implication need to be investigated further. The same methodology can

be employed for NS or WD type compact objects. A typical accretion solution onto a WD type compact object generates satisfactory post- shock properties.

Chapter 4

Effect of Composition on Magnetized Outflows

4.1 Overview

In Chapter 3, we have studied the accretion flow in a defined magnetic field geometry onto compact object. In this chapter, we focus on the wind outflow in the equatorial plane of central object in self-consistent magnetic field without cooling. We study equatorial wind outflow from compact stars by extending Weber & Davis (1967) (abbreviated as WD) model. We concentrate on the role, that correct thermodynamics of the plasma may play on the WD type wind solutions. We consider a CR EoS and obtain outflow solutions for winds around compact objects using PWP to study the behaviour around a stronger gravity. However, we would like to understand the role which strong gravity might play on such wind solutions as well, by comparing with the winds in Newtonian potential. We study how the magnetic field affects the formation of critical points and parameter space by comparing Bondi (*i.e.,* radial), rotating (*i.e.,* Bondi + rotation) and magnetized rotating (Bondi + rotation + magnetic field) outflows. In magnetized rotating outflow, we have shown that a solution passes through all the critical points is a plausible solution for wind outflows. We discuss the exchange of energy in different forms and the effect of magnetic force throughout the flow. Further, we study parameter space and solutions for different angular momentum, energy and composition of the flow. We calculate the streamlines and magnetic field lines, and show that how the rotation of the flow effect configuration of the flow. Plasma composition controls the

thermal energy and inertia of the flow, so we study its effect on flows having different energy. These results are published in Singh & Chattopadhyay (2019a).

4.2 MHD equations and assumptions

4.2.1 Governing equations

We used MHD equations which mentioned in 2.2 with assumptions of the flow is steady, inviscid and highly conducting plasma. Assuming ideal MHD, we integrate MHD equations along magnetic field lines and axis symmetry assumption to obtain the conserved quantities as:

(i) The mass flux conservation is obtained from the continuity equation (2.1),

$$\rho v_{\rm r} r^2 = \text{constant} = \dot{M}, \tag{4.1}$$

(ii) The magnetic flux conservation is obtained from the Maxwell's equation (2.2),

$$B_{\rm r} r^2 = \text{constant} = B_\circ r_\circ^2, \tag{4.2}$$

(iii) The Faraday equation (2.3), for highly conducting fluid gives,

$$r(v_{\rm r} B_\phi - v_\phi B_{\rm r}) = \text{constant} = -\Omega B_{\rm r} r^2, \tag{4.3}$$

(iv) r-component of momentum balance equation (2.4) gives the total energy conservation,

$$\frac{1}{2}v_{\rm r}^2 + \frac{1}{2}v_\phi^2 + h + \Phi(r) - \frac{B_\phi B_{\rm r} \Omega r}{4\pi\rho v_{\rm r}} = \text{constant} = E, \tag{4.4}$$

(v) ϕ-component of momentum balance equation (2.4) gives the total angular momentum conservation,

$$r v_\phi - \frac{B_\phi B_{\rm r} r}{4\pi\rho v_{\rm r}} = \text{constant} = L. \tag{4.5}$$

Here r is the radial distance, $r_\circ$ is the radius of a star, or, the radial distance near black hole, ρ is the mass density, $v_{\rm r}$ is the radial velocity component, v_ϕ is the azimuthal velocity component, $B_{\rm r}$ is the radial magnetic field and subscript '$\circ$' denote the magnetic field at distance $r_\circ$, B_ϕ is the azimuthal magnetic field, Ω is the angular velocity of star

or matter at $r_\circ$. In equation (4.5), we see that total angular momentum has two terms, the first term is the angular momentum associated with matter and the second term represents the angular momentum associated with the magnetic field. Therefore, only sum of both angular momenta is conserved and not the individual entities. This also means angular momentum can transfer between matter to field and vice-versa. The radial Alfvénic Mach number is defined by

$$M_{\rm A}^2 = \frac{4\pi\rho v_{\rm r}^2}{B_r^2}, \tag{4.6}$$

From equations (4.3) and (4.5), we can derive the expression for v_ϕ,

$$v_\phi = \Omega r \frac{(M_{\rm A}^2 L r^{-2}\Omega^{-1} - 1)}{(M_{\rm A}^2 - 1)}. \tag{4.7}$$

4.2.2 Entropy Accretion Rate and Sound Speed

As we discussed in section 2.4.2 the adiabatic relation can be obtained by integrating the $1^{\rm st}$ law of thermodynamics with the help of the continuity equation,

$$\rho = \mathcal{Q}\exp(k_3)\Theta^{3/2}(3\Theta + 2)^{k_1}(3\Theta + 2/\eta)^{k_2}, \tag{4.8}$$

where, $k_1 = 3(2-\xi)/4$, $k_2 = 3\xi/4$ and $k_3 = (f-K)/(2\Theta)$ and $\mathcal{Q}$ is the measure of entropy. Using equation (4.1), the entropy accretion rate $\dot{\mathcal{M}}$ is given by,

$$\dot{\mathcal{M}} = v_{\rm r} r^2 \exp(k_3)\Theta^{3/2}(3\Theta + 2)^{k_1}(3\Theta + 2/\eta)^{k_2}. \tag{4.9}$$

One may note that, $\dot{\mathcal{M}}$ is a temperature and composition dependent measure of entropy, which remains constant along a non-dissipative flow, or in absence of shocks. The sound speed is given by

$$c_{\rm s}^2 = \frac{2\Gamma\Theta c^2}{K}. \tag{4.10}$$

4.3 Methodology

We know that plasma has three signal speeds *i.e.,* slow magnetosonic speed ($u_{\rm S}$), Alfvén speed (in our case we are using radial Alfvén speed $u_{\rm A}$) and fast magnetosonic speed ($u_{\rm F}$) and in the present case, the order of these speeds are $u_{\rm S} < u_{\rm A} < u_{\rm F}$. We know that for outflows, radial velocity ($v_{\rm r}$) is very small near the surface of star or a radius

near the black hole, therefore, $M_{\rm A} \ll 1$ and very far from the central object, $M_{\rm A} \gg 1$. Therefore, at a certain radius (say $r_{\rm A}$), v_r is equal to $u_{\rm A}$ (*i.e.*, $v_{\rm r}|_{r_{\rm A}} \equiv v_{{\rm A}r} = u_{\rm A}$) but at that radius, denominator of v_ϕ is zero (see equation 4.7). Thus the numerator should also be zero at that critical radius to make v_ϕ always finite and this point is known as Alfvén critical point. Therefore, numerator of v_ϕ gives a relation between the critical radius of the Alfvénic point and total angular momentum,

$$L = \Omega r_{\rm A}^2. \tag{4.11}$$

Using equations (4.1), (4.2) and (4.6), we can also write $M_{\rm A}^2$ as,

$$M_{\rm A}^2 = \frac{v_{\rm r} r^2}{v_{{\rm A}r} r_{\rm A}^2} = \frac{\rho_{\rm A}}{\rho}. \tag{4.12}$$

and v_ϕ and B_ϕ become,

$$v_\phi = \frac{\Omega r}{v_{{\rm A}r}} \left(\frac{v_{{\rm A}r} - v_{\rm r}}{1 - M_{\rm A}^2} \right) \quad \text{and} \quad B_\phi = -B_{\rm r} \frac{\Omega r}{v_{{\rm A}r} r_{\rm A}^2} \left(\frac{r_{\rm A}^2 - r^2}{1 - M_{\rm A}^2} \right). \tag{4.13}$$

The r-component of momentum balance equation (2.4) gives the equation of motion,

$$\frac{dv_{\rm r}}{dr} = \frac{\mathcal{N}}{\mathcal{D}}, \tag{4.14}$$

$$\mathcal{N} = v_{\rm r} r \left\{ \left(\frac{2c_{\rm s}^2}{r^2} - \frac{\Phi'(r)}{r} \right) (M_{\rm A}^2 - 1)^3 + \Omega^2 \left(\frac{v_{\rm r}}{v_{{\rm A}r}} - 1 \right) \left[(M_{\rm A}^2 + 1) \frac{v_{\rm r}}{v_{{\rm A}r}} - 3M_{\rm A}^2 + 1 \right] \right\}$$

$$\mathcal{D} = \left(v_{\rm r}^2 - c_{\rm s}^2 \right) (M_{\rm A}^2 - 1)^3 - \frac{\Omega^2}{r^2} M_{\rm A}^4 \left(r^2 - r_{\rm A}^2 \right)^2.$$

To find wind solution, we need two input parameters *i.e.*, E, L, initial boundary conditions and composition of flow ξ which is free parameter. In our case, we use Alfvén point $r_{\rm A}$ as the initial condition because at that radius equation (4.14) or $dv_{\rm r}/dr \to 0/0$. Thus equating the numerator and denominator to zero, provides us with the critical point conditions and hence acts as mathematical boundary conditions. However, $dv_{\rm r}/dr \to 0/0$ at other critical points when $v_{\rm r} = u_{\rm S}$ or $v_{\rm r} = u_{\rm F}$. These critical points are known as the slow critical point ($r_{\rm S}$) or the fast critical point ($r_{\rm F}$), respectively. Therefore, $\mathcal{N} = 0$ and $\mathcal{D} = 0$ are the critical point conditions to find the all critical point (slow points, Alfv én points, fast points and they can either be X-type or O-type) for a given set of input parameters. We have found that for a small energy range and given angular momentum, there exists possibility of five critical points. By supplying total angular

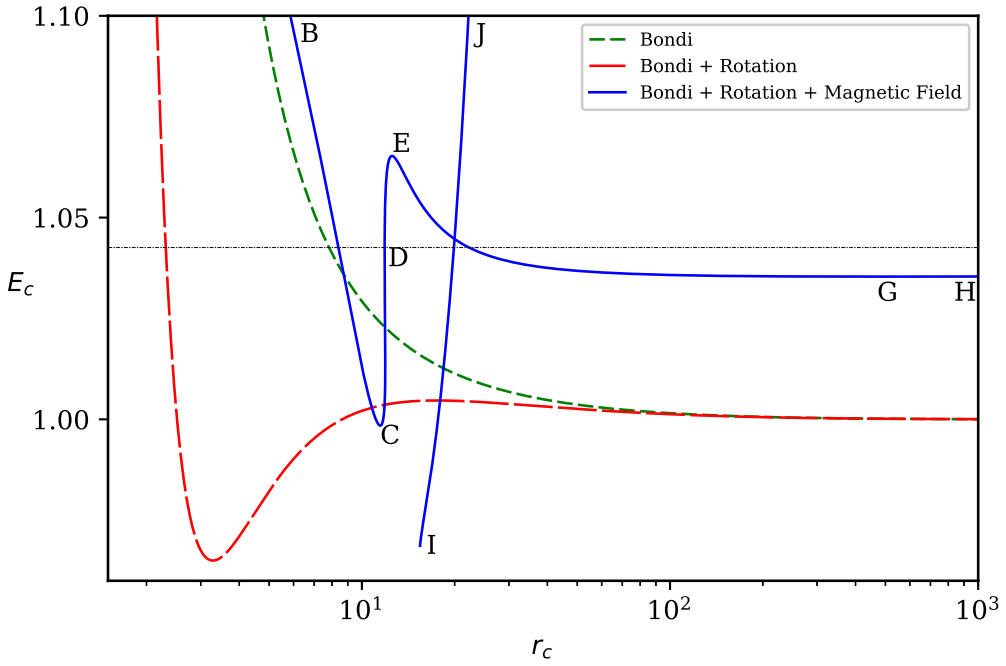

FIGURE 4.1: In this plot, total energy (E_c) is plotted versus critical radius (r_c) for Bondi flow (dashed, green), Bondi flow with rotation (long-dashed, red) and magnetized, rotating flow (solid, blue) for $L = 1.75$. Thin dashed curve represent E=1.04257 (Singh & Chattopadhyay, 2019a).

momentum L, r_A and v_{Ar}, from the critical point conditions we can find out critical radius (r_c) and critical radial velocity v_{rc}. Then, the total energy $E = E_c$ at the critical point can be calculated from equation (4.4) and entropy accretion rate ($\dot{\mathcal{M}} = \dot{\mathcal{M}}_c$) from equation (4.10). With the help of L'Hospital's rule, we determine the gradient of v_r at the critical points. We integrate the equation of motion forward and backward from the critical points with the help of Runge-Kutta 4^{th} order method and find the complete wind solution.

4.4 Analysis and Results

We considered the speed of light in vacuum (c) and Schwarzschild radius (r_g) as the unit of velocity and distance, respectively. Since the Alfvén point is the initial condition, we supply them to obtain solutions of magnetized winds. In Fig. 4.1, we have plotted Bernoulli parameter or specific energy (E_c) as a function of critical radius (r_c) for Bondi flow (dashed, green), Bondi flow with rotation (long-dashed, red) and Bondi flow with both the rotation and magnetic field (solid, blue) for a flow with composition $\xi = 1$. For

rotating flow $L = 1.75$, additionally for magnetized wind, $r_{\rm A} = 11.85$ and $v_{{\rm A}r} = 0.167$. The strong gravity is mimicked by PW potential. Purely Bondi flow (i. e., hydrodynamic flow and only radial velocity component) harbours a single critical point (a sonic point where $v_{\rm r} = c_s$) for any value of $r_{\rm c}$, which is clear from the dashed (green) curve, which is a monotonically decreasing function of r. It may be noted, that the sonic or critical point occurs in a fluid, due to the presence of gravity. A sufficiently hot gas confined very close to the central object would expand against gravity. However, due to $\sim (r - r_{\rm g})^{-2}$ nature of gravity, it will fall faster than the thermal term ($2c_s^2/r$). Since the kinetic term gains at the expense of both gravity and thermal term, at some point $v_{\rm r} \geq c_s$, i. e, the flow becomes transonic at the critical point. The $E_{\rm c}$—$r_{\rm c}$ curve (dashed, green) is a monotonically decreasing function, and therefore, for any given $E = E_{\rm c}$ the Bondi flow admits only one sonic point.

However, for a Bondi-rotating flow (hydrodynamic, $v_{\rm r}$ and v_ϕ components), the effective gravity deviates from its usual $\sim (r - r_{\rm g})^{-2}$ form due to the presence of the centrifugal term v_ϕ^2/r. This interplay of rotation and gravity produces multiple sonic/critical points, which is also clear from the $E_{\rm c}$—$r_{\rm c}$ curve (long-dashed, red). $E_{\rm c}$—$r_{\rm c}$ curve has a maximum and minimum for flows with L above a certain value. Therefore, for any value of $E = E_{\rm c}$ within the two extrema, the flow would harbour multiple critical points.

Hydrodynamics is relatively simple, since in this regime there is only one signal speed i. e., the sound speed (c_s) which is basically the propagating pressure perturbations and are isotropic in nature. Magnetized flow (solid, blue) is entirely a different ball game. As has been mentioned above, there are three signal speeds in a magnetized plasma *i.e.,* slow speed, Alfvén speed and fast speed. It may be noted that propagation of the perturbations of the magnetic field is the Alfvén wave, but the competition between magnetic and plasma pressure gives rise to the slow and fast magnetosonic waves. When the plasma pressure and magnetic pressure works in phase, it is fast wave, if not then it is slow. This is precisely the reason we have three signal speeds in a magnetized plasma. Even the nature of these three waves are different, Alfvén is a transverse wave, while fast and slow waves are longitudinal. Moreover, while Alfvén and slow waves are not isotropic, but fast wave is quasi-isotropic. Hence, instead of sonic points ($v_{\rm r} = c_s$) as we find in hydrodynamic regime, for magnetized plasma, we have slow ($v_{\rm r} = u_{\rm S}$), fast ($v_{\rm r} = u_{\rm F}$) magnetosonic points and Alfvén ($v_{\rm r} = u_{\rm A}$) point.

Above, we have discussed that multiple critical points may arise in non-magnetized plasma because of the presence of angular momentum. This also applies in magnetized

plasma too. However, the additional feature is the plasma angular momentum is itself modified by the magnetic field (equation 4.5), therefore the effective gravity is modified by the plasma angular momentum as well as the magnetic field components. In other words, addition of rotation in magnetized plasma leads to the existence of one to four critical points in general, but within a small energy range ($E_{\rm c}$) we have found five critical points. It means the flow can either be super-slow ($v_{\rm r} > u_{\rm S}$) and/or super-Alfvén ($v_{\rm r} > u_{\rm A}$) and/or super-fast ($v_{\rm r} > u_{\rm F}$) or we can say that flow can pass through one critical point or through multiple critical points similar to WD wind solution (Weber & Davis, 1967). Curve marked BC represent X-type slow points, CD represents O-type slow points, DE is O-type fast points. Points on the curve EG are X-type fast points, while GH curve are O-type fast points. Curve IJ is another set of X-type slow points. The thin, dashed curve is for $E = 1.04257$, which represents the outflow solution in the next figure, passes through slow, Alf vén, and fast points, or is equivalent to the classical WD solution.

In Fig. 4.2 (a), we plot the $E_{\rm c}$ with $\dot{\mathcal{M}}_{\rm c}$ corresponding to the curves of Fig. 4.1. The zones marked BC, CD, DE, EG, and GH are shown on this figure too. The parameters corresponding to the solid box (red) correspond to the outflow solution which passes through the slow, Alfv́en and fast points (i. e, the outflow is trans-slow, trans-Alfv́en, trans-fast). Fig. 4.2 (a) clearly shows that, wind represented by the solid box (red), possesses the same entropy ($\dot{\mathcal{M}}_{\rm c}$) and energy $E_{\rm c}$ in all the three critical points. The solid inverted triangle represents a flow which has the same specific energy and total angular momentum as the flow represented by the solid box, but passes only through the slow and/or Alfvén critical points and has lower entropy. One may remember, that to find the solutions, we have to supply $r_{\rm A}$ along with E, L and ξ, and obtain the value of $v_{{\rm A}r}$ by iteration. We choose $r_{\rm A} = 11.85$ for all the solutions in this study, till mentioned otherwise. In Fig. 4.2 (b), we plot the actual outflow solutions, corresponding to the parameters of the solid square of Fig. 4.2 (a). It may be noted $v_{{\rm A}r} = 0.167$ in this case. The solid (red) curve with arrows shows the outflow solution passing through the slow (trans-slow), Alfv́en (trans-Alfv́en) and fast points (trans-fast) represented on the figure as S (*i.e.*, $r_{\rm S}$), A (*i.e.*, $r_{\rm A}$), and F (*i.e.*, $r_{\rm F}$), respectively. This solution passes through all the critical points and is a global solution (connecting outflows near the compact object with asymptotically large distance). Since the entropy of all the critical points are same (solid square in Fig. 4.2 a), the wind solution is smooth. Among all possible global solutions, the one passing through S, A and F has higher entropy and therefore is the correct physical solution. This is equivalent to the WD class of

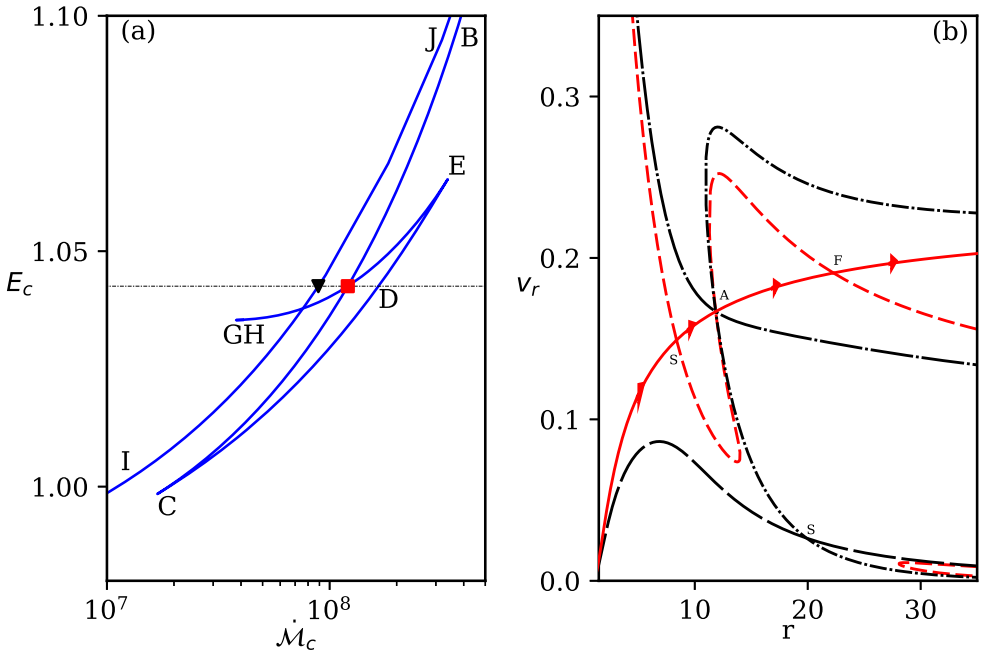

FIGURE 4.2: (a) E_c—$\dot{\mathcal{M}}_c$ plot corresponding to Fig. 4.1. The branches named BC, CD etc up to IJ are also marked on the curve. The square (red) corresponds to the outflow solution passing through slow, Alfv́en and fast points. The triangle (black) represent solutions which is not passing through all three critical points. (b) v_r versus r or actual outflow solutions. The solid red curve with arrow heads represent the transonic wind solution passing through slow, Alfv́en and fast points, marked as S, A, F, respectively. The dashed red curves are the transonic outflow solutions with wrong boundary condition. long-dashed black curve is a trans-slow solution. Dashed-dotted curve is the trans-slow, trans-Alfv́en solutions and long-dashed-dotted curve is a trans-Alfv́enic flow. $E = 1.04257$ (dotted horizontal), $L = 1.75$ for all the curves (Singh & Chattopadhyay, 2019a).

solutions. The dashed curve represents the solution which also passes through S, A and F points but with boundary conditions which are opposite to that of the outflow solution and is multi-valued in a limited range of r. The boundary condition of an outflow is that it has to be sub-slow (i.e., $v_r \sim$ small) near the central object and super-fast (i.e, $v_r \sim$ high) at asymptotically large distances, which is evidently not the case for the dashed (red) curve. Other solutions which are not marked with arrows, also do not satisfy the boundary conditions of an outflow. These solutions either pass through A (long-dashed-dotted, black), or through A and S (dashed-dotted, black), or at times only through S (long-dashed, black). It is interesting to inquire about solutions for $E > 1.04257$ mark (above the dotted horizontal curve in Fig. 4.2 a). Such solutions may have entropy higher than that corresponding to the solid square, but unfortunately, those solutions do not pass simultaneously through r_S, r_A, & r_F. Moreover, if there

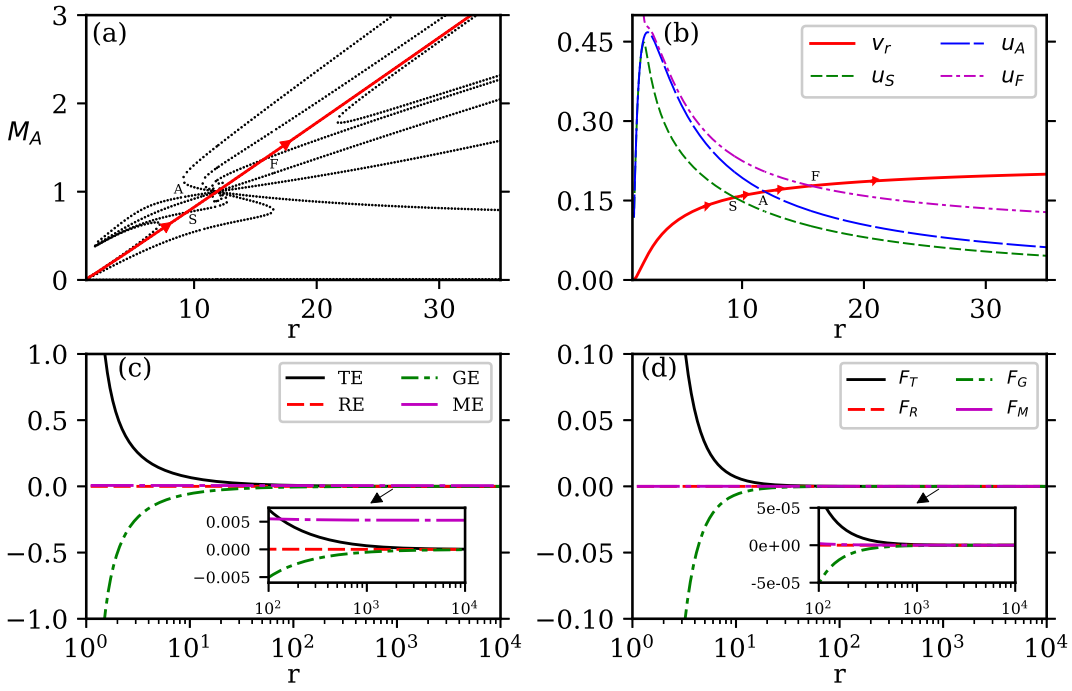

FIGURE 4.3: (a) M_A vs r as a function of r. The solid curve with arrow heads is the physical wind solution and the dotted are other unphysical branches. Location of the slow magneto-sonic, Alfvén and fast magneto-sonic points are marked as S, A and F, respectively. (b) Comparing v_r (solid with arrows, red), u_S (dashed, green), u_A (long-dashed blue) and u_F (dashed-dot, violet) of the physical wind branch as a function of r. The locations where v_r crosses u_S, u_A and u_F are marked as S, A and F. (c) Thermal (solid, black), rotational (dashed, red), gravitational (dashed-dot, green) and magnetic (long- dashed-dotted violet) terms of the Bernoulli parameter E are named as TE, RE, GE and ME, respectively. (d) Comparison of forces F_T (solid, black), F_R (dashed, red), F_G (dashed-dot, green), F_M (long-dashed violet) as function of r. Panels (b— d) presents variables corresponding to the solution (solid) in panel a. The wind is for $E = 1.03075$ and $L = 1.0$. Here $\xi = 1$ (Singh & Chattopadhyay, 2019a).

exist a global solution for such parameters, still we cannot consider them as proper solutions because those are decelerating. The resulting terminal speed therefore, is less than the solution represented by solid curve with arrows in Fig. 4.2 (b). In other words, the outflow solution for any set of E—L, which passes simultaneously through r_S, r_A and r_F (one with arrows) is the correct and accelerating class of wind solutions and was first pointed out by Weber & Davis (1967).

In Fig. 4.3 (a), we plot the Alfvén Mach number M_A (equation 4.6) as a function of r, corresponding to the physical solution (trans-slow, trans-Alfvén, trans-fast) represented as solid curve, marked with arrows. Physical wind solution passes simultaneously through all the three critical points S, A and F. The dotted curves represent other unphysical solutions. It may be noted that, ordinary Mach number distribution

(i. e., $v_{\rm r}/c_s$) is not presented in the figure. This is simply because in a magnetized plasma, sound speed works in tandem with magnetic pressure and by itself is not vitally important. However, Alfvén speed determines the flow structure, therefore, the information whether a flow is super or sub Alfvénic is important. In Fig. 4.3 (b), we compare $v_{\rm r}$ (solid with arrows, red), $u_{\rm S}$ (dashed, green), $u_{\rm A}$ (long-dashed blue) and $u_{\rm F}$ (dashed-dot, violet) of the physical wind solution presented in the previous panel, as a function of r. These solutions corresponds to $E = 1.03075$, $L = 1.0$ and $\xi = 1$. The locations of $r_{\rm S}$, $r_{\rm A}$ and $r_{\rm F}$ (marked as S, A and F in the figure) corresponds to the intersection of $v_{\rm r}$ with $u_{\rm S}$, $u_{\rm A}$ and $u_{\rm F}$. In Fig. 4.3 (c), we plot various components of E, namely, the thermal or TE ($\equiv h - 1$), the rotational or RE ($\equiv v_\phi^2/2$), the gravitational or GE ($\equiv \Phi$) and the magnetic or ME ($\equiv -\{B_\phi B_{\rm r}\Omega r\}/\{4\pi\rho v_{\rm r}\}$) terms of equation (4.4). The inset zooms all the curves for $r \rightarrow$ large. Near the compact object, TE term dominates, while at $r \gtrsim 100 r_{\rm g}$ the ME term dominates. Similarly, we plot various force terms $F_{\rm T}$ (thermal), $F_{\rm R}$ (rotational), $F_{\rm G}$ (gravitational) and $F_{\rm M}$ (magnetic), along the streamline in Fig. 4.3 (d). Near the central object, $F_{\rm T}$ drives the flow against gravity. At large distance all the forces become comparable to each other, therefore comparing the combination of forces which competes with each other gives a better picture. The thermal force is the primary agency which opposes gravity, while magnetic force reduces v_ϕ. So we paired the competing forces like $F_{\rm T}$ and $F_{\rm G}$ and compared with the other combination $F_{\rm R}$ and $F_{\rm M}$. At large distance the magnetic and the centrifugal forces together exceeds the thermal and the gravitational forces and drives the wind outward (see Fig. B.1 in Appendix B).

We study the effect of L on outflow solutions. In Fig. 4.4 (a) we plot $E_{\rm c}$ as a function of $r_{\rm c}$, each curve is for $L = 0.1$ (solid, black), 1.0 (dashed, red) and 2.0 (long-dashed, green). With the increase of L, the flow becomes more energetic at a given critical point. In Fig. 4.4 (b) we plot $E_{\rm c}$ versus $\dot{\mathcal{M}}_{\rm c}$. For each value of L, all the branches for O-type and X-type critical points are present, however for low L (solid, black) the kite-tail part is very small, which implies that multiple critical points are possible only for a rotating flow. Although L has a significant effect on the parameter- space, but in order to get a more quantitative idea, one need to compare outflow solutions for different L but same E.

We compare the flow solutions, like $v_{\rm r}$ (Fig. 4.5 a), v_ϕ (Fig. 4.5 b), Θ (Fig. 4.5 c) and Γ (Fig. 4.5 d) as a function of r, for various values of $L = 0.35$ (solid, black), $L = 1.0$ (dashed, red), $L = 2.0$ (long-dashed, green). All the plots have the same Bernoulli parameter $E = 1.03075$ and $\xi = 1.0$. In Fig. 4.5 (a), the solid circle, arrow head, and

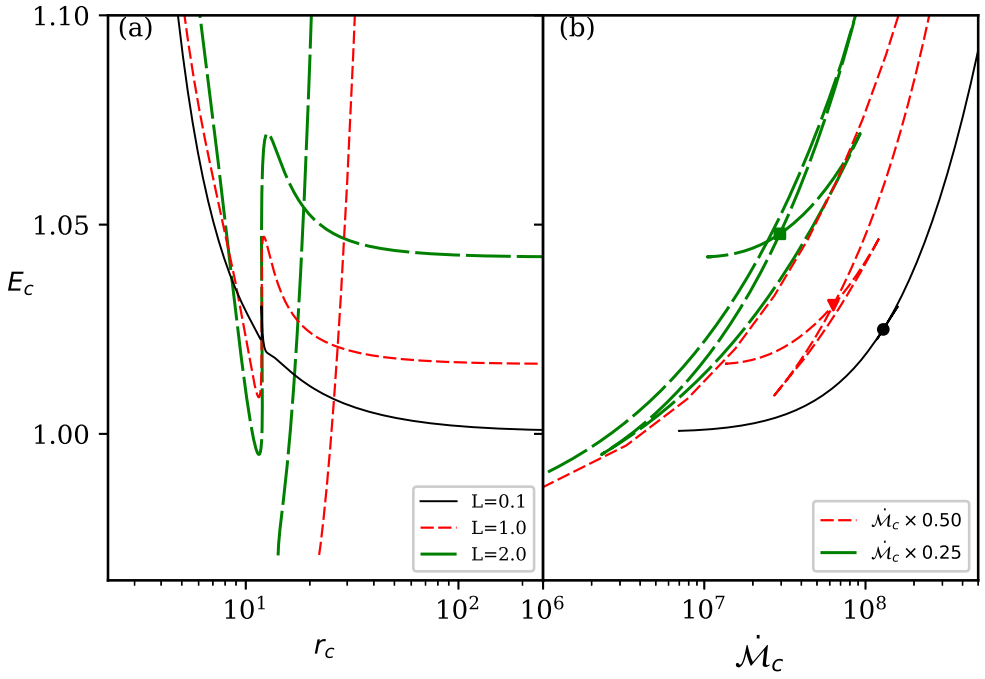

FIGURE 4.4: (a) We have plotted the total energy E_c at critical point r_c for total angular momentum $L = 0.1$ (solid, black), 1.0 (dashed, red) and 2.0 (long-dashed, green). (b) E_c—$\dot{\mathcal{M}}_c$ for various values of $L = 0.1$ (solid, black), 1.0 (dashed, red) and 2.0 (long-dashed, green). Here $\xi = 1$ (Singh & Chattopadhyay, 2019a).

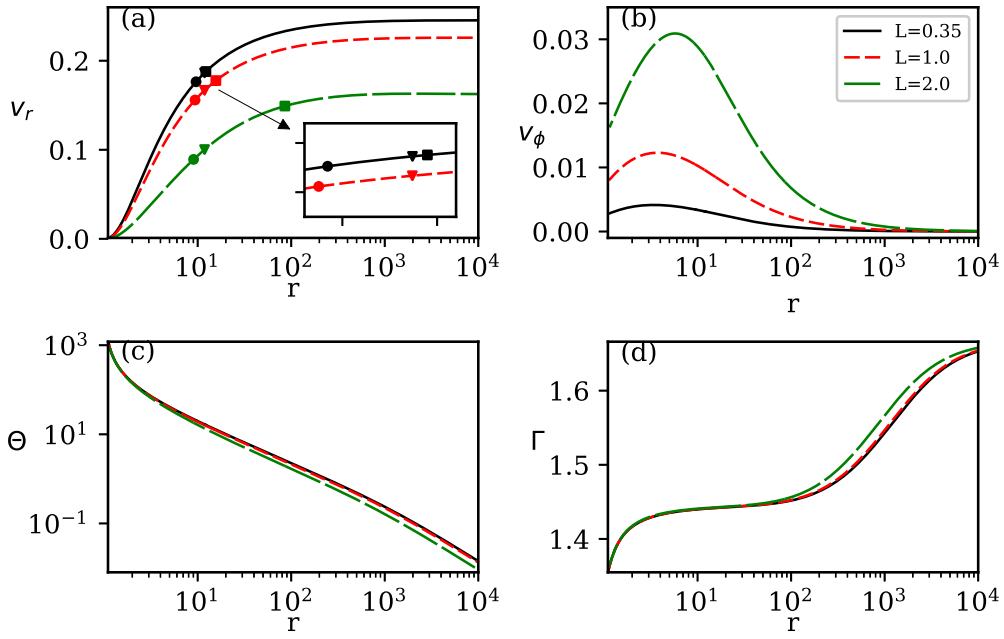

FIGURE 4.5: Flow solutions like, (a) v_r, (b) v_ϕ, (c) Θ and (d) Γ as a function of r. Each curve is for $L = 0.35$ (solid, black), $L = 1.0$ (dashed, red), $L = 2.0$ (long-dashed, green) Here $E = 1.03075$, $\xi = 1$ (Singh & Chattopadhyay, 2019a).

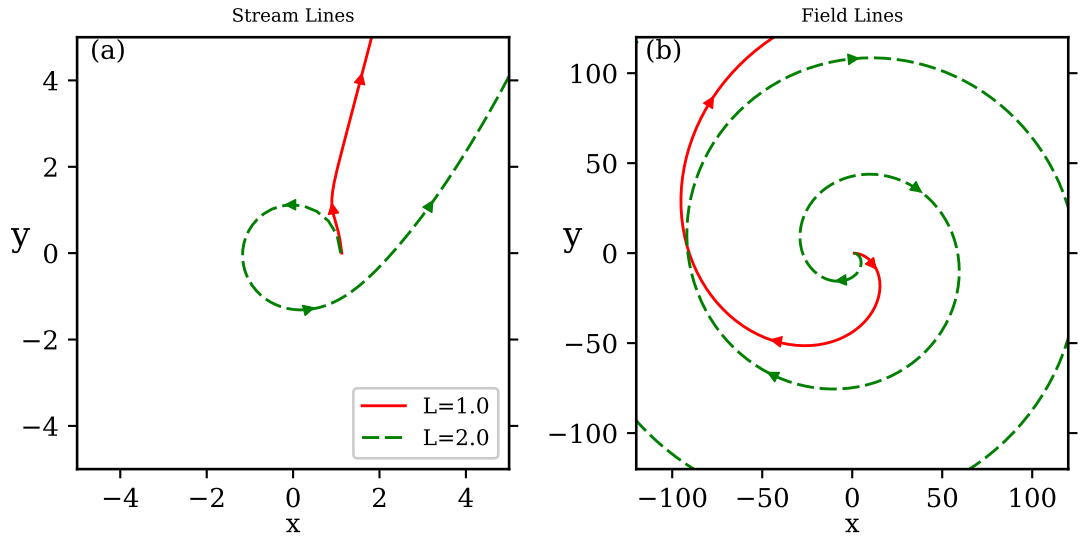

FIGURE 4.6: (a) Flow streamlines and (b) magnetic field lines. Each of the curves are for total angular momentum $L = 1.0$ (solid, red) and $L = 2.0$ (dashed, green) in xy-plane. In both the cases $E = 1.03075$ (Singh & Chattopadhyay, 2019a).

square represents the positions of the slow, Alfvén and fast points, respectively. For $L = 0.35$, the Alfv én and fast points are almost merged, the inset zooms the region to resolve those two points. Outflows with higher L and same E have higher values of v_ϕ. Interestingly, outflows with higher values of L, are slower (low $v_{\rm r}$ in long-dashed curve). If one compares various terms in the equation (4.4), by keeping E constant but increasing L, then the budget in centrifugal and magnetic terms are larger compared to that in radial kinetic and thermal terms. Therefore, v_ϕ increases with L, but $v_{\rm r}$ and Θ decreases.

We plot the outflow streamlines in Fig. 4.6 (a) and the magnetic field lines Fig. 4.6 (b) of a plasma whose $E = 1.03075$, where total angular momenta are $L = 1.0$ (solid, red) and $L = 2.0$ (dashed, green) in xy-plane. The wind streamline (SL) and magnetic field lines (FL) are obtained by integrating the following equations,

$$d\phi_{\rm SL} = \frac{v_\phi}{v_{\rm r}}\frac{dr}{r}; \;\&\; d\phi_{\rm FL} = \frac{B_\phi}{B_r}\frac{dr}{r} \tag{4.15}$$

This plot reconfirms the governing equations which showed that the magnetic field is clockwise but the wind is counter clockwise. It also shows a very important effect that magnetic field has on ionized plasma. It modifies the plasma streamline by redistributing the plasma angular momentum (rv_ϕ), such that, for $L = 1.0$ flow (solid red;

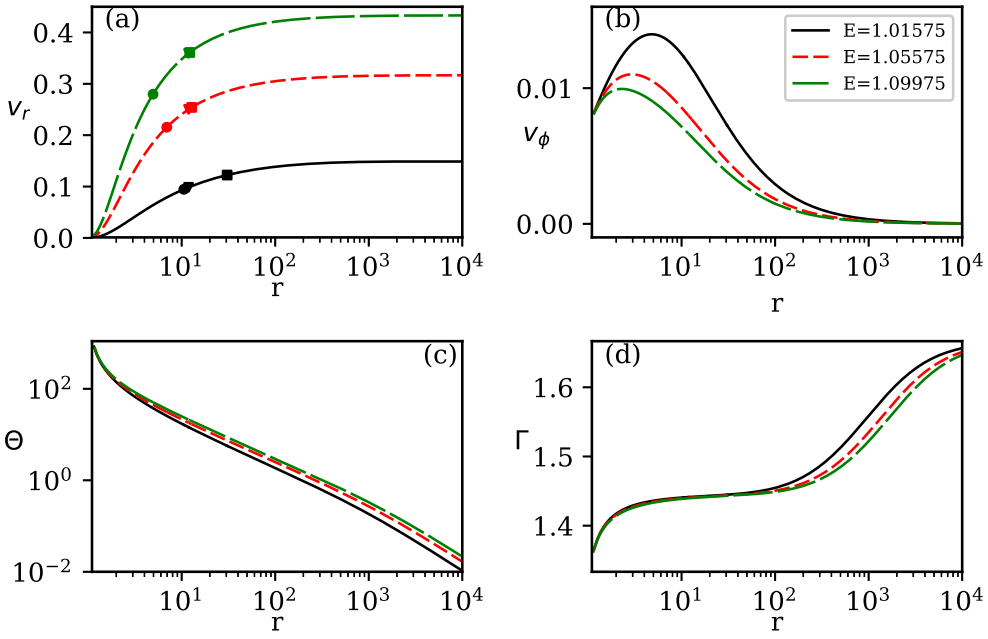

FIGURE 4.7: These are the wind solutions for different Bernoulli parameters $E = 1.01575$ (solid, black), 1.05575 (dashed, red) and 1.09975 (long-dashed, green). We have plotted the radial velocity $v_{\rm r}$ (a), v_ϕ (b), Θ (c) and Γ (d) versus radius r. All the plots are for $L = 1.0$ and $\xi = 1.0$ (Singh & Chattopadhyay, 2019a).

Fig. 4.6 a) which was launched with a counter-clockwise rotation, is flung out even before completing a loop. So this figure presents the structure of the outflow for two angular momenta as depicted in Fig. 4.5. It is clear that the outflow and the magnetic field are not parallel to each other.

To study the effect of Bernoulli parameter, we compare $v_{\rm r}$ (Fig. 4.7 a), v_ϕ (Fig. 4.7 b), Θ (Fig. 4.7 c) and Γ (Fig. 4.7 d), for various values of $E = 1.01575$ (solid, black), 1.05575 (dashed, red) and 1.09975 (long-dashed, green) for a given value of $L = 1.0$. The solid circle, arrow head, and square represents the positions of the slow, Alfvén and fast points, respectively. The flow with higher E is faster (high $v_{\rm r}$), less rotating (low v_ϕ) and hotter (high Θ) compared to flows with lower values of E. Γ is not constant in any of the cases discussed so far and it follows the Θ distribution.

In Fig. 4.8, we present the effect of strong gravity. We chose electron-proton or $\xi = 1.0$ plasma, where the flow has the same Bernoulli parameter E ($= 1.301$), $r_{\rm A}$ ($= 3.3859$) and total angular momentum L ($= 1.75$). However, we compare magnetized-wind solutions expanding in a region described by Newtonian gravitational potential (solid, black) with another one in a region described by PWP (dashed, red). We chose a higher value of E, in order to maximize the effect. Even for the same specific energy and

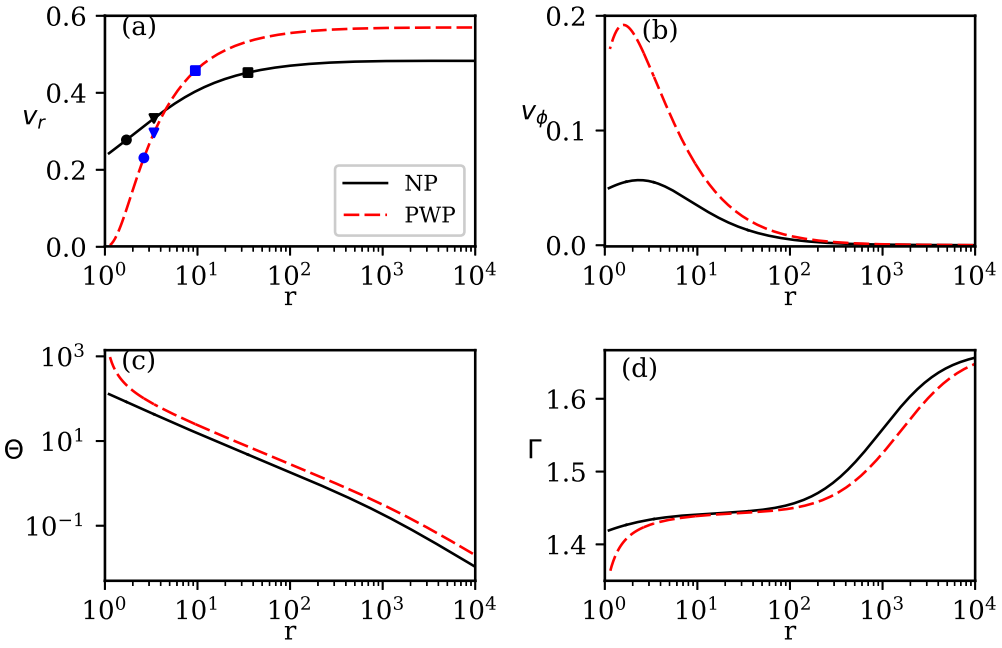

FIGURE 4.8: Wind solution in Newtonian potential $\Phi_{\rm NP}$ (solid, black) and in Paczyński & Wiita potential $\Phi_{\rm PWP}$ (dashed, red) for $E = 1.301$, $L = 1.75$ and $\xi = 1$. The flow variables are (a) $v_{\rm r}$, (b) v_ϕ, (c) Θ and (d) Γ versus radius r. The slow-point, Alfvén point and fast-point are marked as solid circle, triangle and square (Singh & Chattopadhyay, 2019a).

angular momentum, the wind in a region described by $\Phi_{\rm PWP}$ is faster and hotter than the one in a region described by a Newtonian gravity. The stronger gravity of a $\Phi_{\rm PWP}$ compresses the plasma around the compact object and produces a higher temperature flow. The inner boundary condition of the outflow in $\Phi_{\rm NP}$, shows that $v_{\rm r}$ (although sub-slow) is quite high, while v_ϕ and Θ is lower than that around $\Phi_{\rm PWP}$. The acceleration achieved for flows around $\Phi_{\rm NP}$ is quite moderate, while that around $\Phi_{\rm PWP}$ is significant. If we use lower E then perhaps the $v_{\rm r}$ at the inner boundary for $\Phi_{\rm NP}$ will have proper value but then the terminal speed would be very low. One may conclude that, if we use $\Phi_{\rm NP}$ to describe the gravity around a compact object, then, only slow outflows can be obtained.

In Fig. 4.9 (a, b), we plot the effect of composition of the flow on its critical point properties. We plot the Bernoulli parameter as a function of critical radius i.e., $E_{\rm c}$ versus $r_{\rm c}$, for fixed value of $L = 1.0$ and $r_{\rm A} = 11.85$, but different values of composition or $\xi = 0.0$ (solid, black), $\xi = 0.5$ (dashed, red), $\xi = 1.0$ (long-dashed, green). Similar to previous $E_{\rm c}$ and $\dot{\mathcal{M}}_{\rm c}$ plot, the proper wind solution corresponds to the $E_{\rm c}$ versus $\dot{\mathcal{M}}_{\rm c}$

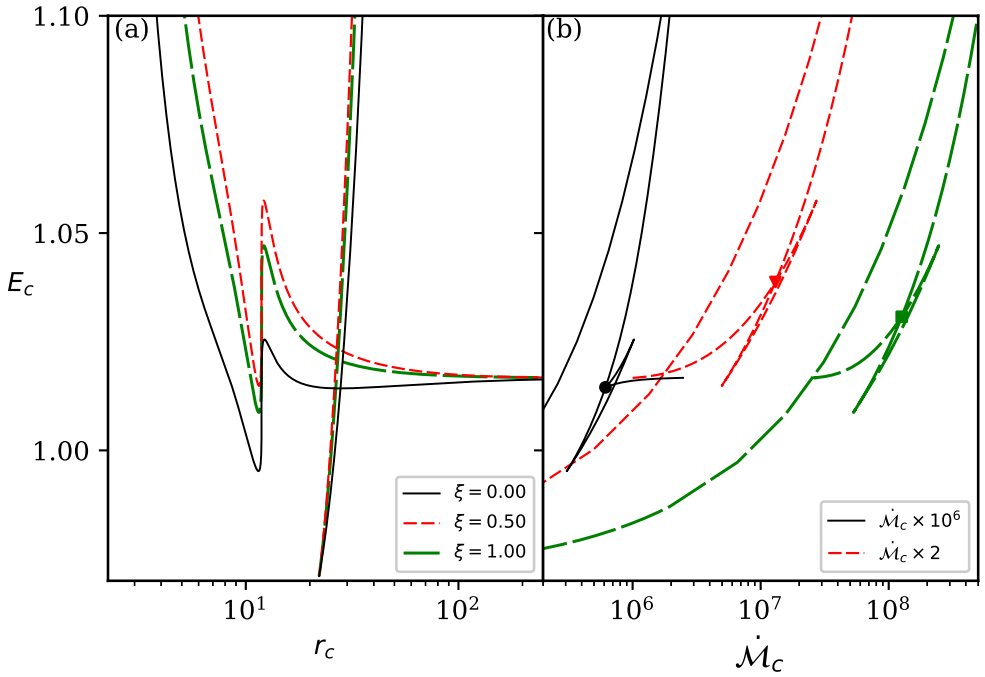

FIGURE 4.9: In panel we plot, (a) E_c versus r_c and (b) E_c versus $\dot{\mathcal{M}}_c$. The curves represent $\xi = 0.0$ (solid, black), $\xi = 0.5$ (dashed, red), $\xi = 1.0$ (long-dashed, green). All plots are for $L = 1.0$ (Singh & Chattopadhyay, 2019a).

at the intersection of the X-type slow branch and X-type fast branch (marked as solid circle, triangle and a square for three values of ξ).

In Fig. 4.10 (a-d), we compare v_r, v_ϕ, Θ and Γ for flows with the same E $(= 1.03075)$ and L $(= 1.0)$ but for different composition $\xi = 0.05$ (solid, black), 0.5 (dashed, red) and 1.0 (long-dashed, green). All the flow variables like v_r, v_ϕ and Θ depend on ξ. The $\xi = 1.0$ or electron-proton flow has somewhat higher v_r close to the base. The lepton dominated wind ($\xi = 0.05$) has higher v_r at some intermediate range of r, but finally for a flow with a composition parameter $\xi = 0.5$, the terminal v_r or $v_r^{\rm max} = v_r|_{r\to\infty}$ is higher than the flow with other two combinations, albeit by a small amount. This is not expected in hydrodynamics. It may be noted that, in hydrodynamics for $r \to$ large, $h \to 1$, centrifugal term $\to 0$, $\Phi(r) \to 0$, $v_r^{\rm max} \to \sqrt{2(E-1)}$. In other words, the terminal speeds of winds in hydrodynamics do not depend on composition, but for MHD winds, even as $r \to$ large, $h \gtrsim 1$ because of the presence of the magnetic term and hence $v_r^{\rm max}$ depends on ξ. The azimuthal velocity v_ϕ also depends on ξ, where an electron-proton flow has the least v_ϕ distribution when compared with flows of higher proportion of leptons. However, $v_\phi \to 0$ at $r \to$ large, therefore the asymptotic value of v_ϕ does not depend on ξ. It may be noted that, the effect of ξ cannot be studied by attributing

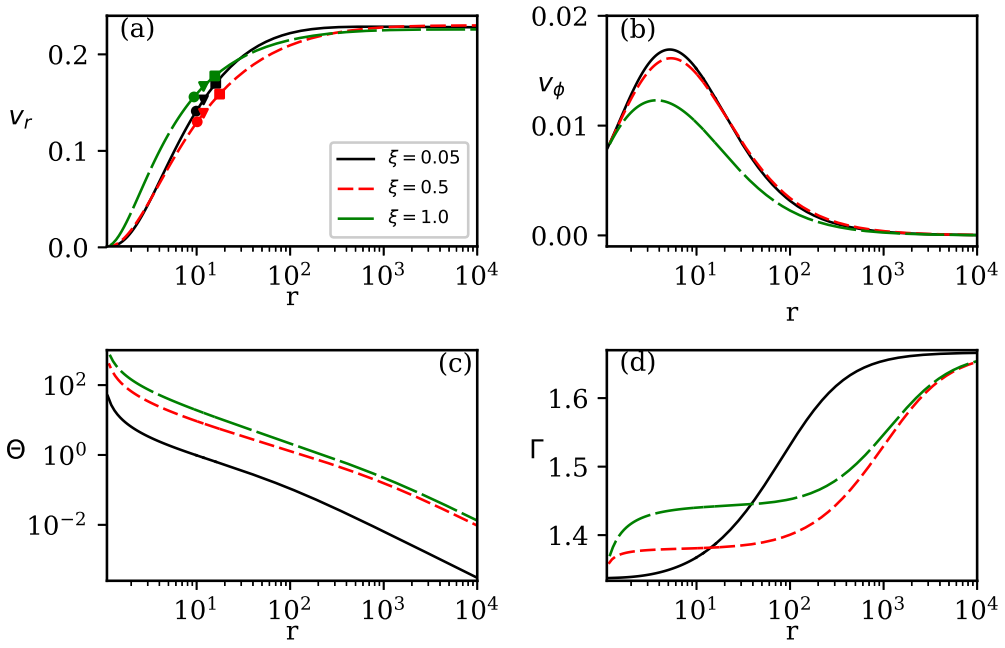

FIGURE 4.10: (a) $v_{\rm r}$, (b) v_ϕ, (c) Θ and (d) Γ as a function of r, where each curve represent $\xi = 0.05$ (solid, black), $\xi = 0.5$ (dashed, red) and $\xi = 1.0$ (long-dashed, green). All the curves have the same $E = 1.03075$ and $L = 1.0$ (Singh & Chattopadhyay, 2019a).

some scale factor, as one can clearly see that, the v_ϕ curves intersect for flows with $\xi = 0.5$ and 0.05. Similar to all the studies in the hydrodynamic regime in the present case too, the temperature distribution $\Theta(r)$ is highest for $\xi = 1.0$. Although Θ is high for $\xi = 1.0$ compared to other flows with $\xi < 1$, the Γ for electron-proton flow is not the lowest. In fact, at lower values of r, $\Gamma_{\xi=0.05} < \Gamma_{\xi=0.5} < \Gamma_{\xi=1}$. This is because, Γ compares the thermal energy of the plasma compared to its inertia, hence high value of Θ cannot compensate for higher inertia of an electron-proton flow. In comparison, a lepton dominate flow ($\xi = 0.05$) achieves $\Gamma \to 4/3$, in spite of starting with a temperature at least an order of magnitude less that of an electron-proton flow.

In Fig. 4.11, we have plotted $v_{\rm r}^{\rm max}$ as a function of ξ, for various values of energies ($E = 1.15475,\ 1.04575,\ 1.03075,$ and 1.01075) and a given value of L. It is interesting to note that terminal speed distribution for higher to lower energies of the magnetized outflow, depends on ξ. For higher energies, it decreases with ξ, but for lower E, $v_{\rm r}^{\rm max}$ maximizes at some value of ξ. The maxima depends on E. This is a significantly different result compared to hydrodynamics. This effect arises due to the competition between pressure gradient and magnetic forces in the equations of motion.

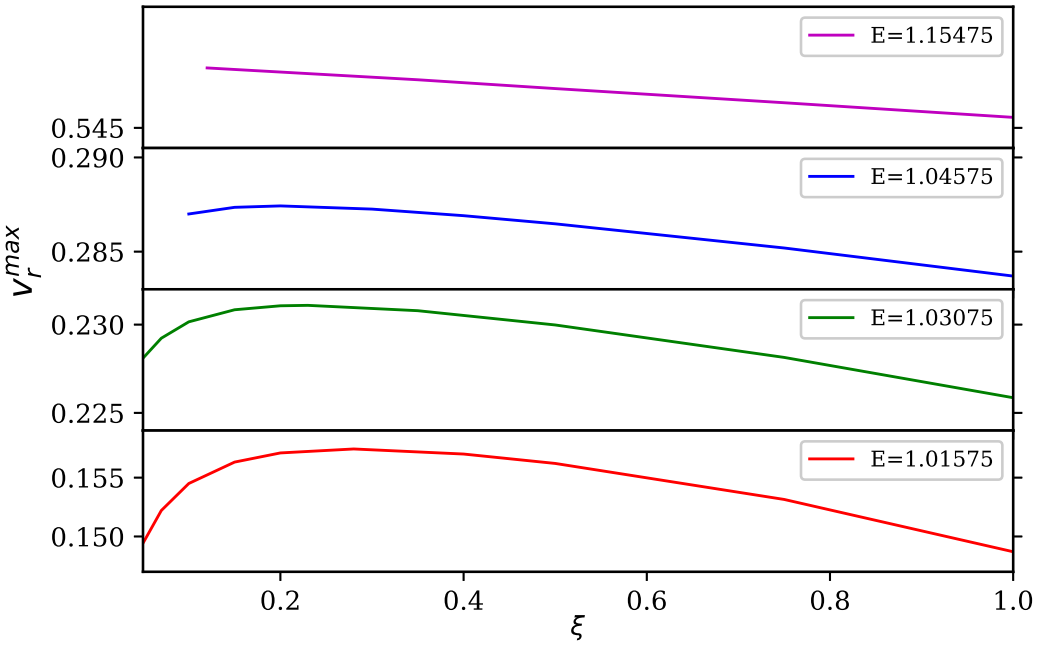

FIGURE 4.11: Terminal speed $v_{\rm r}^{\rm max}$ is plotted as a function of ξ from top panel and downwards for $E = 1.15475,\ 1.04575,\ 1.03075$, and 1.01075, respectively. $L = 1.0$ for all the curves (Singh & Chattopadhyay, 2019a).

4.5 Discussion and Concluding Remarks

Our main focus is on studying the effect of variable Γ EoS and the composition on magnetized wind solutions. This model is the bedrock over which magnetized jet models were developed later. In this context, it may be noted that there are of course many models of generation of outflows around compact objects, tailored to address different scenarios. For example, if the underlying accretion disc is luminous then radiation can drive outflows via scattering processes (Icke, 1980; Tajima & Fukue, 1996, 1998; Moller & Sadowski, 2015; Yang *et al.*, 2018; Vyas & Chattopadhyay, 2019) or for cooler gases via the line driven processes (Nomura *et al.*, 2016; Nomura & Ohsuga, 2017). In case the accretion flow is of low luminosity, then magnetic, gas pressure and centrifugal term may drive outflows (Gu, 2015; Yuan *et al.*, 2015; Bu *et al.*, 2016a,b; Bu & Mosallanezhad, 2018). In the present study, we are also working in the regime where radiation is not important. However, our main focus is to study a typical transmagnetosonic outflow solution and what are the parameters these solutions depend on. In particular, the effect of a variable Γ EoS and different compositions of the plasma on the outflow solution has probably not been studied before. In this study, we have revisited magnetized, wind model using Paczyński & Wiita potential, variable Γ EoS

and for various values of total angular momentum (L), Bernoulli parameter (E) and composition (ξ) of the flow. E and L are constants of motion. However, as is the case in hydrodynamics, in MHD too, there can be a plethora of solutions corresponding to the same set of constants of motion. As has been shown by Bondi (1952), of all the possible solutions related to a given set of constants of motion, the physical global solution is the one which has the highest entropy and also happens to be the transonic one. Similarly in MHD (Fig. 4.2), it was shown that the solution passing through slow, Alfv́en and fast points is the correct solution. We have found that for a given set of values of E and ξ, higher angular momentum outflows are slower (lesser $v_{\rm r}$) compared to flows with lower L. This is understandable, since matter which is rotating faster, will not able to possess higher $v_{\rm r}$. In particular, for flows with lower L, magnetic field may deflect outflow from counter clockwise to a quasi- radial flow relatively close to the central object (Fig. 4.6 a). In other words, the effect of magnetic field cannot be quantified by how much the flow is accelerated radially, but magnetic field has a very important role in regulating flow angular momentum. We also show that faster outflow is possible, for flows with higher E. Interestingly, the Θ differs slightly if E or L is changed, but the change in $v_{\rm r}$ and v_ϕ is more significant. However, $v_{\rm r}$, v_ϕ and Θ distributions are significantly different for different values of ξ. This is because, if we change the composition of the flow, then we are not only changing its thermal energy content (which pushes the matter outward), but also the inertia of flow. Therefore, the terminal speed of the outflows at a given value of E and L maximizes at a given value of ξ. Although, the ξ at which the peak of $v_{\rm r}^{\rm max}$ will occur, also depends on E. The peak steadily shifts to higher ξ as E decreases. The dependence of various flow variables on ξ for MHD flows probably has not been reported before. In addition, the spectra emitted by such winds should be quite different for different values of ξ, since the different velocity distributions would result in different density distributions. Moreover, different temperature distributions would strongly determine the processes that would dominate the emission. We also studied the wind solutions in different gravitational potentials to show how the compactness of the central object affects the outflow solutions.

Chapter 5

Study of Relativistic Magnetized Outflows with Relativistic Equation of State

5.1 Overview

In this chapter, we continue our study of outflows of Chapter 4 but now about the axis of rotation and not along the equatorial plane. Collimated outflows or jets start very close from the central object where the temperature is very high and these outflows have relativistic speeds, so we study these outflows in the special relativistic regime. Since the outflows scale a large temperature range while flowing out, we use relativistic equation of state (CR EoS) to describe the thermal state of the outflow. Moreover, magnetic field is expected to play a vital role, therefore we study these outflows in special relativistic magnetohydrodynamic (SMHD) regime. In this study, we follow the methodology of Polko *et al.* (2010), but consider a CR EoS to obtain the radially self-similar solutions. There are few parameters (*i.e.,* current distribution, entropy) and initial conditions (*e.g.,* angle of magnetic field lines with the disc plane at the Alfvèn point, the cylindrical radius of the Alfvèn point, etc) which give rise to various plausible solutions. We analyse the dependence of such solutions on aforementioned parameters and initial conditions. Further, we also calculate the streamlines, and study behaviour of forces which affect the outflow acceleration and morphology. As mentioned in Chapter 1 that Polko *et al.* (2010) used Vlahakis *et al.* (2003a) model with fixed adiabatic

index ($\Gamma = 5/3$) equation of state and showed that the flow can become trans-Alfvénic (sub Alfvénic to super Alfvénic) and trans-fast (sub fast to super fast). In contrast, Vlahakis *et al.* (2003a) could obtain only trans-Alfvénic flow with $\Gamma = 4/3$. Therefore, the thermodynamics of the flow may play an important role in determining the nature of the solution. Thus, we have also studied the effect of EoSs (*i.e.,* fixed adiabatic index and CR EoSs) on outflow solutions. We have shown that the flow variables (*i.e.,* velocity, temperature, etc.) highly depend on the plasma composition. These results are published in Singh & Chattopadhyay (2019b).

5.2 Special relativistic magnetohydrodynamic equations and assumptions

5.2.1 Governing equations

We have used the special relativistic magnetohydrodynamic (SMHD) equations (see section 2.3) for the study of relativistic outflows. As we have explained in section 2.4 that we need two closure equations, one for the electro-magnetic field which is flux freezing condition of MHD and another for the matter which is EoS, these two equations help to reduce the number of unknowns.

5.2.1.1 Relativistic EoS having variable Γ

In this analysis of outflows we use relativistic EoS (see section 2.4.3). Integrating $1^{\rm st}$ law of thermodynamics ($u_\mu \nabla_\nu T^{\mu\nu} = 0$) with the help of continuity equation, we can obtain the adiabatic equation of state,

$$\rho = \mathcal{K} g(\Theta, \xi), \tag{5.1}$$

where, $g(\Theta,\xi) = \exp(k_3)\Theta^{3/2}(3\Theta+2)^{k_1}(3\Theta+2/\eta)^{k_2}$, $k_1 = 3(2-\xi)/4$, $k_2 = 3\xi/4$ and $k_3 = (f-K)/(2\Theta)$ and $\mathcal{K}$ is the measure of entropy. Therefore, pressure p is given by,

$$p = \frac{2\mathcal{K} g(\Theta,\xi)\Theta}{K} c^2 \tag{5.2}$$

5.2.2 Conventional form of SMHD equations

By using the EoS and ideal MHD assumption, we can write equations (2.5) and (2.6) in the conventional form. The mass conservation equation is $\nabla_\mu(\rho u^\mu) = 0$, or the

continuity equation,

$$\frac{\partial\left(\gamma\rho\right)}{\partial t}+\boldsymbol{\nabla}.\left(\mathbf{v}\gamma\rho\right)=0. \tag{5.3}$$

The momentum conservation equation is, $\nabla_\nu T^{k\nu}=0$, where the $k=1,2,3$ components,

$$\gamma\rho\left(\frac{\partial}{\partial t}+\mathbf{v}.\boldsymbol{\nabla}\right)\left(h\gamma\mathbf{v}\right)=-\boldsymbol{\nabla}p+\frac{J^0\mathbf{E}+\mathbf{J}\times\mathbf{B}}{c}. \tag{5.4}$$

The first law of thermodynamics is obtained by going to the co-moving frame of the flow, $u_\mu T^{\mu\nu}_{\ ,\nu}=0$,

$$\left(\frac{\partial}{\partial t}+\mathbf{v}.\boldsymbol{\nabla}\right)e+p\left(\frac{\partial}{\partial t}+\mathbf{v}.\boldsymbol{\nabla}\right)\left(\frac{1}{\rho}\right)=0, \tag{5.5}$$

where $e\equiv\bar{e}/\rho$.

We study the axisymmetric steady flow, therefore, $\partial/\partial t=0$ and $\partial/\partial\phi=0$. For axisymmetric flow, the solenoidal condition can be written as,

$$\boldsymbol{\nabla}.\mathbf{B}=\boldsymbol{\nabla}.\mathbf{B}_{\rm p}=0. \tag{5.6}$$

The total magnetic field B is given as,

$$\mathbf{B}=\mathbf{B}_{\rm p}+\mathbf{B}_\phi,\ \ \text{where, }\mathbf{B}_{\rm p}=\frac{\boldsymbol{\nabla}A\times\hat{\phi}}{\varpi}. \tag{5.7}$$

Here, $\mathbf{B}_{\rm p}$ and $\mathbf{B}_\phi$ are the poloidal and azimuthal components of the magnetic field, respectively. The $A(\varpi,z)$ is a poloidal magnetic flux function and this can be defined as $A=\frac{1}{2\pi}\int\int\mathbf{B}_{\rm p}.d\mathbf{S}$ and $\mathbf{B}_{\rm p}.\boldsymbol{\nabla}A=0$ which means that poloidal magnetic field lines are orthogonal to the gradient of magnetic flux function. Here, ϖ represents the cylindrical radius, $\mathbf{v}\equiv v_{\rm p}\mathbf{e}_{\rm p}+v_\phi\mathbf{e}_\phi$, $v_{\rm p}$ is poloidal velocity and v_ϕ is azimuthal velocity. With the help of ideal MHD flow condition (2.7) and $E_\phi=0$ (from Faraday equation 2.6) we can show that $\mathbf{v}_{\rm p}\parallel\mathbf{B}_{\rm p}$, so

$$E=\frac{\varpi\Omega}{c}\mathbf{B}\times\mathbf{e}_\phi,\ \ \mathbf{v}=\frac{\Psi_{\rm A}}{4\pi\gamma\rho}\mathbf{B}+\varpi\Omega\mathbf{e}_\phi\ \text{and}\ \frac{\Psi_{\rm A}}{4\pi\gamma\rho}=\frac{v_{\rm p}}{B_{\rm p}}. \tag{5.8}$$

Here, $\Psi_{\rm A}$ is the mass to magnetic flux ratio and Ω is the field angular velocity. We can obtain the constants of motion by projecting equations (5.3) - (5.5) along and perpendicular to the streamline and then integrating them (for more details see Vlahakis *et al.*, 2003a), we have five constants of motion $\Omega(A,s),\ \Psi_{\rm A}(A,s),\ L(A,s),\ \mu(A,s),\ \mathcal{K}(A,s)$, where $s\equiv ct-\ell$, t is time and ℓ is length of a poloidal field line. These constants of motion are as follows:

(i) The mass to magnetic flux ratio is obtained from continuity equation (5.3) and equation (5.6),

$$\Psi_{\rm A} = \frac{4\pi\gamma\rho v_{\rm p}}{B_{\rm p}}. \tag{5.9}$$

(ii) The angular velocity of field lines at the disc is obtained from the Faraday equation (2.3),

$$\Omega = \frac{v_\phi}{\varpi} - \frac{\Psi_{\rm A} B_\phi}{4\pi\gamma\rho\varpi}. \tag{5.10}$$

(iii) Azimuthal component of momentum balance equation (5.4) gives the total specific angular momentum *i.e.,* angular momentum associated with the matter ($L_{\rm M}$) and magnetic field ($L_{\rm B}$), has the form,

$$L \equiv L_{\rm M} + L_{\rm B} = h\gamma\varpi v_\phi - \frac{\varpi B_\phi}{\Psi_{\rm A}}. \tag{5.11}$$

(iv) By taking dot product with velocity (**v**) with momentum balance equation (5.4) gives the total energy to mass flux ratio *i.e.,* energy associated with the matter ($\mu_{\rm M}$) and magnetic field ($\mu_{\rm S}$), has the form,

$$\mu \equiv \mu_{\rm M} + \mu_{\rm S} = h\gamma - \frac{\varpi\Omega B_\phi}{\Psi_{\rm A} c^2}. \tag{5.12}$$

(v) The measure of entropy is given by equation (5.1),

$$\mathcal{K} = \frac{\rho}{g(\Theta,\xi)}. \tag{5.13}$$

The poloidal Alfvénic Mach number (see, Michel, 1969) is defined as,

$$M \equiv \frac{\gamma v_{\rm p}}{\left(B_{\rm p}/\sqrt{4\pi\rho h}\right)},$$

and using equations (2.15), (5.2) and (5.8), we can also write M as,

$$M^2 = q(A)\frac{h(h - f(\Theta,\xi)/K)K}{2\Theta g(\Theta,\xi)} = q(A)\frac{h}{g(\Theta,\xi)}, \tag{5.14}$$

where $q(A) \equiv \Psi_{\rm A}^2/4\pi\mathcal{K}$. To solve SMHD equations we assume that jet solutions are radially self-similar (for more details see section 3 in Vlahakis *et al.*, 2003a). The derivative of dimensionless temperature Θ and enthalpy h *w.r.t* polar angle θ is given by,

$$\frac{d\Theta}{d\theta} = -\frac{g(\Theta,\xi)\Theta K}{qN\left(hK - 2\Gamma\Theta\right)}\frac{dM^2}{d\theta} \text{ and } \frac{dh^2}{d\theta} = -\left(\frac{2h^2}{M^2}\right)\frac{2\Gamma\Theta}{hK - 2\Gamma\Theta}\frac{dM^2}{d\theta}. \tag{5.15}$$

If we take the derivative of total energy *w.r.t* polar angle (θ) with the help of equations (5.14) and (5.15) we obtain (for more details see Appendix C and Polko *et al.*, 2010),

$$A_1(\theta,\psi,G^2,M^2)\frac{dM^2}{d\theta}+B_1(\theta,\psi,G^2,M^2)\frac{d\psi}{d\theta}=C_1(\theta,\psi,G^2,M^2), \tag{5.16}$$

where $x\equiv\varpi\Omega/c$ is cylindrical radius in terms of light-cylinder, $G\equiv x/x_{\rm A}$ (here, $x_{\rm A}\equiv x$ at Alfvén point) and ψ is the angle of poloidal field line with the disc. The transfield equation which controls the collimation of the flow, can be obtained from the momentum equation by taking dot product with $-\boldsymbol{\nabla}A$ *i.e.,* perpendicular to the poloidal field line,

$$A_2(\theta,\psi,G^2,M^2)\frac{dM^2}{d\theta}+B_2(\theta,\psi,G^2,M^2)\frac{d\psi}{d\theta}=C_2(\theta,\psi,G^2,M^2). \tag{5.17}$$

Therefore, we can get the wind equation or outflow equation ($dM^2/d\theta$) for radially self-similar flows by solving (5.16) and (5.17) equations,

$$\frac{dM^2}{d\theta}=\frac{C_1B_2-C_2B_1}{A_1B_2-A_2B_1}. \tag{5.18}$$

Where, the coefficients A_1, B_1, C_1, A_2, B_2 and C_2 are given in the Appendix C. The wind equation (5.18) has two critical points (Alfvén and fast critical point) *i.e.,* where it becomes $0/0$ form and this can be solved with the L'Hospital's rule, so the Alfvén point condition is given in the Appendix C.

5.3 Methodology

We study the flow in the special relativistic domain, in which the slow magnetosonic point does not form, *i.e.,* we find the solution from the sub-Alfvénic to super-fast regime. To obtain the solution of magnetically driven relativistic outflow about the axis of symmetry, we integrate equations (5.15)[1] and (5.18). In addition, we also solve equation (C.2) and total energy to mass flux ratio equation (C.1) to obtain ψ if the value of μ is known. First, we supply the values of Alfvén point $x_{\rm A}$, F (current distribution), q, $\theta_{\rm A}=\theta|_{x_{\rm A}}$, $\psi_{\rm A}=\psi|_{x_{\rm A}}$. We obtain $M_{\rm A}^2$ $(=1-x_{\rm A}^2)$ and therefore $\Theta_{\rm A}$ using equations (2.15 & 5.14). Then we obtain $\sigma_{\rm A}$ from equations (C.10 & C.11) for a given value of $\sigma_{\rm M}$. Now we obtain the value of μ and $p_{\rm A}=dM^2/d\theta|_{x_{\rm A}}$ from equations (C.10) and (C.9), respectively. With these values, we integrate equations (5.18, C.2, 5.14 or 5.15) starting from $x_{\rm A}$ inward and outward. The solution may not pass through the fast point,

[1]Equation (5.14) instead of equation (5.15) may also be used, since they are equivalent.

so we iterate on $\sigma_{\rm M}$ until the solution passes through the fast point as well. We use Runge- Kutta fourth order method to integrate but also use Newton-Raphson's method to accurately obtain the flow quantities like $\theta_{\rm f},\ \psi_{\rm f},\ G^2_{\rm f}, M^2_{\rm f}$, where the suffix 'f' denotes quantities measured at the fast-point. Since, we integrate the equations starting from the Alfvén point, therefore $x^2_{\rm A}, \theta_{\rm A}, \psi_{\rm A}$ essentially are the boundary conditions or boundary parameters. In this study, there is no need to specify adiabatic index Γ since it is self-consistently obtained from EoS. In addition to this, we have one more free parameter ξ which controls the composition of the flow.

5.4 Analysis and Results

In this analysis, the velocity is measured in the units of speed of light c, distance is in units of light cylinder $r_{\rm c} \equiv \frac{c}{\Omega}$ and temperature is in degree Kelvin. In our model, there are two main free input parameters F and q, three boundary parameters $\psi_{\rm A}, \theta_{\rm A}, x^2_{\rm A}$ and a composition parameter ξ. We study the effect of these parameters on the outflow solutions and on the collimation of outflowing matter with CR EoS.

5.4.1 Solutions for different current distributions (F)

In Fig. 5.1, we plot different solutions for different current distribution parameter $F = 0.750$ (solid, black), 0.760 (dashed, red), 0.770 (long-dashed, green), 0.780 (dashed-dotted, blue), 0.795 (long-dashed-dotted, magenta) and other four parameters are fixed *i.e.,* $x^2_{\rm A} = 0.75,\ \theta_{\rm A} = 50,\ \psi_{\rm A} = 55,\ q = 500$ & $\xi = 1.0$. In Fig. 5.1 (a), the projected streamline in the $x-z$ plane is plotted. The distribution of corresponding flow variables like logM^2 (Fig. 5.1 b), poloidal velocity $v_{\rm p}$ (Fig. 5.1 c), azimuthal velocity v_ϕ (Fig. 5.1 d), matter ($\mu_{\rm M}$) and magnetic field ($\mu_{\rm S}$) part of the Bernoulli parameter (Fig. 5.1 e), angular momentum associated with the matter $(L_{\rm M})$ and magnetic field $(L_{\rm B})$ which are part of the total angular momentum (Fig. 5.1 f), Lorentz factor γ (Fig. 5.1 g), log of temperature log$T$ (Fig. 5.1 h) and adiabatic index Γ (Fig. 5.1 i) with log$z$ are plotted. In Fig. 5.1 (a), solid-circles represent Alfvén point location and solid-triangles represent the fast point location, where z is the vertical height and x is the cylindrical radius. In Fig. 5.1 (a), we note that if we increase F, the solution collimates at higher height (z). Higher value of F implies weaker magnetic field near the base, so it travels larger z before the outflow starts to collimate. In panel Fig. 5.1 (c), we see that $v_{\rm p}$ has a dip, which is due to the interaction of magnetic field with matter. Near the base, $\mu_{\rm S}$ gains at the cost of

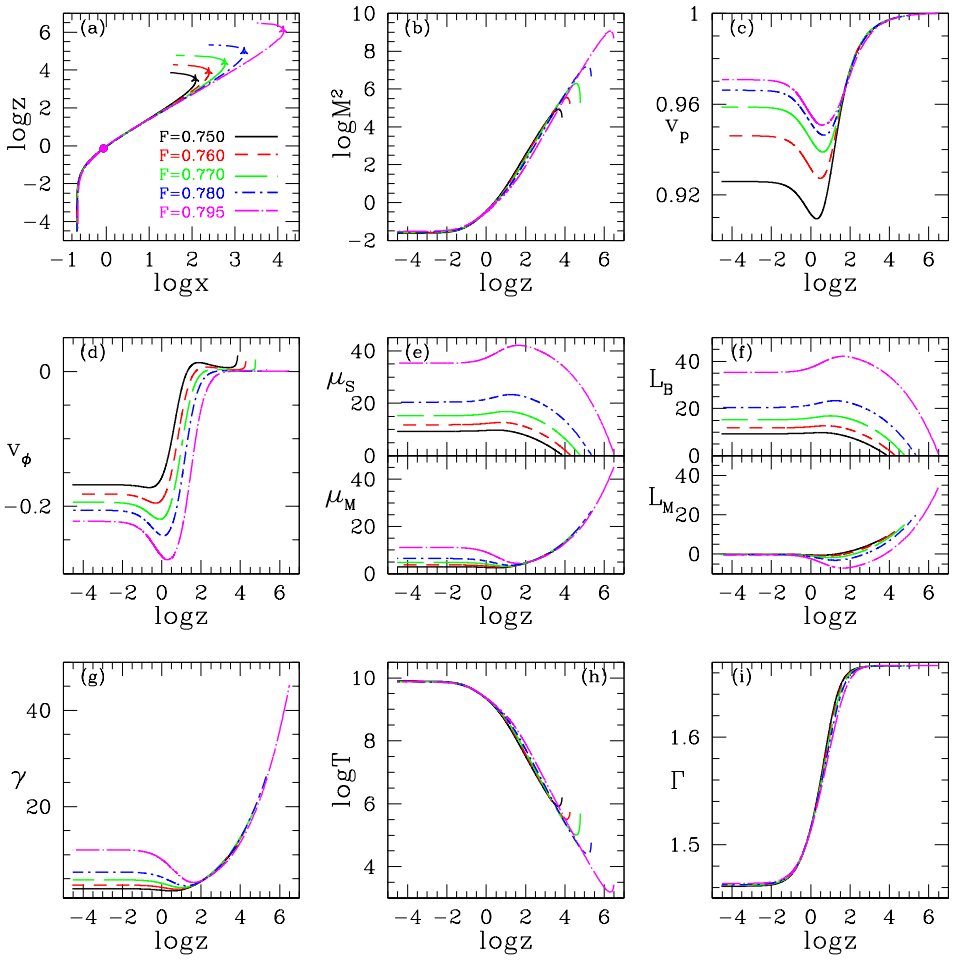

FIGURE 5.1: Outflow solutions for different values of $F = 0.750$(solid, black), 0.760(dashed, red), 0.770(long-dashed, green), 0.780(dashed-dotted, blue), 0.795(long-dashed-dotted, magenta) and other four parameters are fixed *i.e.*, $x_{\rm A}^2 = 0.75, \theta_{\rm A} = 50, \psi_{\rm A} = 55, q = 500, \xi = 1$. (a) Projected streamline, (b) logM^2, (c) $v_{\rm p}$, (d) v_ϕ, (e) $\mu_{\rm S} = -\varpi\Omega B_\phi/\Psi_{\rm A}c^2$ and $\mu_{\rm M} = \gamma h$, (f) $L_{\rm B}$ and $L_{\rm M}$, (g) γ, (h) log$T$ and (i) Γ, are plotted with log$z$. Here, z is vertical height and x is cylindrical radius in units of light cylinder. Solid circles and triangles represent Alfvén point and fast-point locations (Singh & Chattopadhyay, 2019b).

$\mu_{\rm M}$ (Fig. 5.1 e), therefore there is simultaneous decrease in thermal and kinetic terms. When the magnetic energy ($\mu_{\rm S}$) becomes sufficiently strong, it starts to accelerate the outflow, although the outflow temperature continues to decrease. Hence there is a dip in $v_{\rm p}$. Another very interesting result is that v_ϕ changes sign from negative to positive (Fig. 5.1 d). It means, initially the flow is rotating clockwise and somewhere in between the Alfvén and the fast points, the flow flips to a counter-clockwise direction. In MHD, we have two types of angular momentum, one that is associated with the matter $L_{\rm M} \equiv h\gamma\varpi v_\phi$ and the other associated with the magnetic field $L_{\rm B} \equiv -\varpi B_\phi/\Psi_{\rm A}$. Therefore, only total angular momentum is conserved throughout the flow but not the individual angular momenta (Fig. 5.1 f). Thus, azimuthal velocity v_ϕ changes sign

because of transfer of angular momentum from magnetic field to matter. In Fig. 5.1 (g), the variation of Lorentz factor γ is shown. We can see that higher value of F produces outflows with higher Lorentz factor $\gamma \sim 45$ ($F = 0.795$, long-dashed-dotted). In Fig. 5.1 (h), we plot temperature variation of the outflow with height, for different values of F parameter. We can see that outflow starts with high temperature when it is sub-Alfvénic and temperature drops to very small value when the flow becomes super-fast. Last panel Fig. 5.1 (i) shows that the adiabatic index Γ does not remain constant throughout the solution, it varies from $\Gamma \sim 1.44$ to $5/3$. It is well known that gases with non-relativistic temperatures have $\Gamma = 5/3$ or the polytrpoic index $N = 3/2$. For gases with ultra-relativistic temperatures, $N \to 3$ or $\Gamma \to 4/3$. It may be noted that, N is the temperature gradient of the specific energy of the gas i.e., $\sim df/d\Theta$ (see, equation 2.15). For non- relativistic thermal speed (for $T \lesssim 10^7$K), the energy density of the gas ($\bar{e}$) is dominated by rest-mass energy, so N (therefore Γ) remains constant ($\equiv 5/3$). But for higher temperatures, the thermal speed becomes relativistic, therefore kinetic contribution becomes comparable to rest mass in $\bar{e}$, as a result N increases with rising T. But the upper limit of thermal speed is c, therefore for ultra-relativistic temperature, the kinetic contribution of the gas particles into $\bar{e}$ of the gas becomes maximum and therefore N again becomes temperature independent, where asymptotically $N \to 3$ (or, $\Gamma \to 4/3$). For example, if the temperature of a gas is in between these two extremes ($10^7\text{K} < T < 10^{13}\text{K}$), then the thermal state is described by $3/2 \lesssim N \lesssim 3$ (see Fig. 1 a in Chattopadhyay & Ryu, 2009). In Fig. 5.1 (h), temperature drops from $\sim 10^{10}$ to $\sim 10^4$ the thermal energy decreases as a result, Γ changes from ~ 1.44 (near-relativistic) to $\sim 5/3$ (non-relativistic).

In Fig. 5.2, we plot the streamlines of outflow solution for $x_{\rm A}^2 = 0.75, \theta_{\rm A} = 50, \psi_{\rm A} = 55, F = 0.75, q = 500, \xi = 1$. Figs. 5.2 (a) & (b) are the side and top view of streamlines of the outflow, respectively. Here xy plane represents the equatorial plane and z is the vertical height from the equatorial plane in terms of light cylinder. Two dashed circles, one near to the base ($z \sim 0.73$ i.e., the circle in the inset of both the panels) represents the Aflvén point location. The other at $z \sim 3500$ represents the fast point location. As we discussed before, the transfer of angular momentum from the field to the matter, changes the direction of rotation of the flow. We can also see in Fig. 5.2, that the transfer of angular momentum from field to the matter has twisted the streamlines of the outflow.

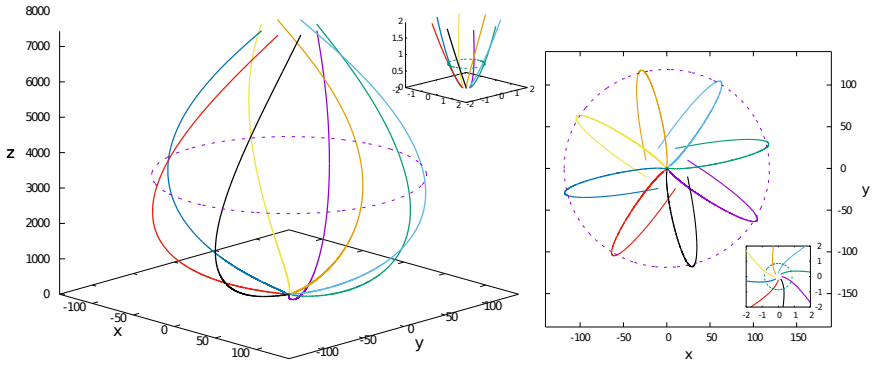

(a) Side view (b) Top view

FIGURE 5.2: Solid curves represent the streamlines of outflow solution for $x_{\rm A}^2 = 0.75, \theta_{\rm A} = 50, \psi_{\rm A} = 55, F = 0.75, q = 500, \xi = 1$. (a) Side view and (b) top view. There are two dashed circles, one near to the center at $z \sim 0.73$ represents the Aflvén point location and second at $z \sim 3500$ represents the fast point location. Here, z is vertical height and x, y are in terms of light cylinder. Inset: Region close to the base is zoomed to show the location of the Alfvén point (dashed circle) (Singh & Chattopadhyay, 2019b).

5.4.2 Solutions for different Alfvén point angle ($\psi_{\rm A}$) with the disc

In Fig. 5.3 we plot outflow solutions for different values of $\psi_{\rm A} = 50$ (solid, black), 52 (dashed, red), 54 (long-dashed, green), 55 (dashed-dotted, blue) and 56 (long-dashed-dotted, magenta). All the curves are for fixed values of $x_{\rm A}^2 = 0.75, \theta_{\rm A} = 50, F = 0.75, q = 500$ and $\xi = 1$. In Fig. 5.3 (a), the solution which has lower values of $\psi_{\rm A}$ are less collimated. Since, centrifugal force also has component in the poloidal direction *i.e.*, $\cos(\psi)$ component of centrifugal force (see equation C.5 in Appendix C), therefore flow which has small Alfvén point angle with the equatorial plane has larger centrifugal force which spreads the outflow over larger x. In general, the solutions with lower $\psi_{\rm A}$, are of lower μ and $\sigma_{\rm M}$ and therefore are slower (i.e., less $v_{\rm p}$). Although μ and L are constants of motion, but respective magnetic and matter components of each are not constants. The azimuthal component of velocity v_ϕ also flips sign. Panels Fig. 5.3 (h-i) show the variation of temperature and adiabatic index (varies from 1.4 to $5/3$) of the flow.

5.4.3 Solutions for different Alfvén point polar angle ($\theta_{\rm A}$)

In Fig. 5.4, we plot outflow solutions for different values of $\theta_{\rm A} = 44$ (solid, black), 46 (dashed, red), 48 (long-dashed, green), 50 (dashed-dotted, blue), 51 (long-dashed-dotted, magenta). Five parameters are fixed $x_{\rm A}^2 = 0.75$, $\psi_{\rm A} = 55$, $F = 0.75$, $q = 500$ and $\xi = 1$ for all the curves. Solutions with smaller $\theta_{\rm A}$ start with a smaller base (small

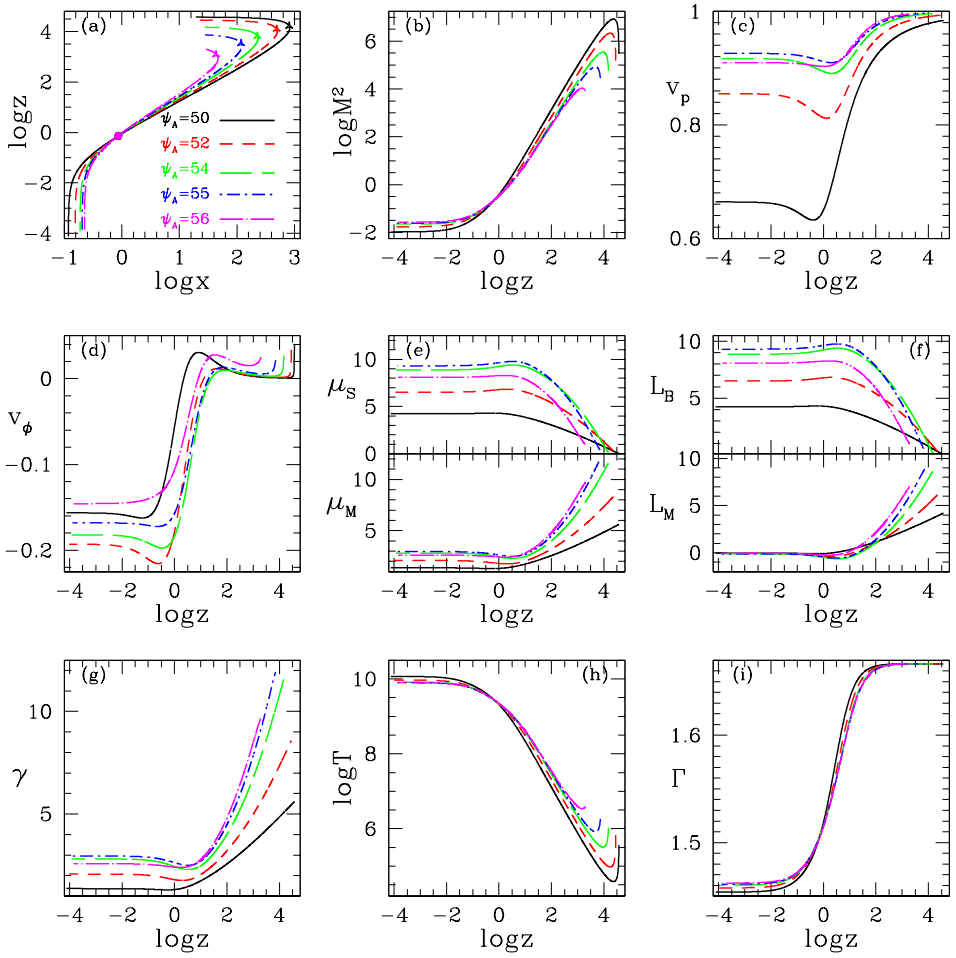

FIGURE 5.3: Outflow solutions are for different values of $\psi_{\rm A} = 50$ (solid, black), 52 (dashed, red), 54 (long-dashed, green), 55 (dashed-dotted, blue), 56 (long-dashed-dotted, magenta). All the curves plotted are for $x_{\rm A}^2 = 0.75$, $\theta_{\rm A} = 50$, $F = 0.75$, $q = 500$, & $\xi = 1$. Panel (a) streamline on the xz-plane, (b) $\log M^2$, (c) $v_{\rm p}$, (d) v_ϕ, (e) $\mu_{\rm S}$ and $\mu_{\rm M}$, (f) $L_{\rm B}$ and $L_{\rm M}$, (g) γ, (h) $\log T$ and (i) Γ versus $\log z$. Here, solid circles and triangles represent Alfvén and fast point locations (Singh & Chattopadhyay, 2019b).

x), but expands to a larger x. While the ones starting with larger $\theta_{\rm A}$ shows exactly the opposite property. This is because the solution with smaller $\theta_{\rm A}$ have larger value of B_ϕ near the base, but at higher z, B_ϕ decreases faster than the one starting with higher values of $\theta_{\rm A}$. In general, $v_{\rm p}$ of outflow solution is higher for higher value of $\theta_{\rm A}$ (= 51, long-dashed-dotted, magenta). The $\mu_{\rm S}$ and $\mu_{\rm M}$ feeds at each other's cost, although the total specific energy μ remains constant along the flow. This is similar to the constancy of the total angular momentum of the flow, but components associated with the field and the matter are not constant. As in the previous cases, here too the adiabatic index is not constant.

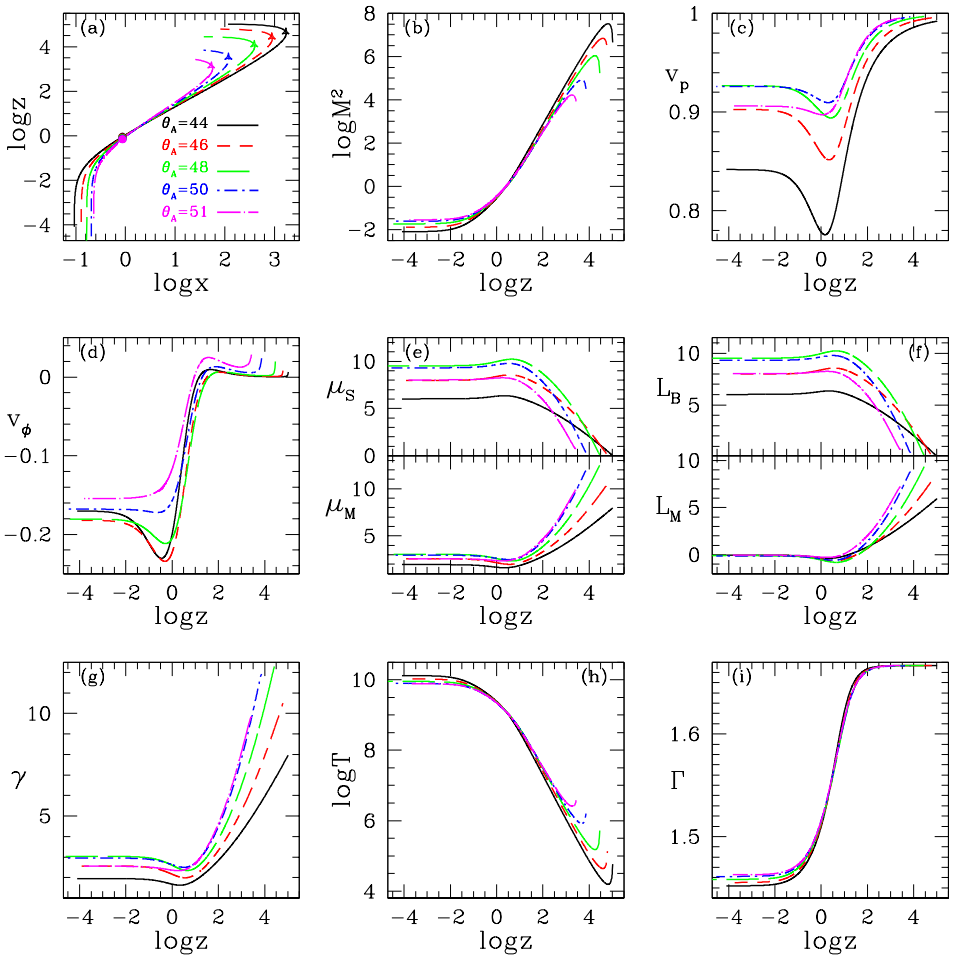

FIGURE 5.4: Outflow solutions for different values of $\theta_A = 44$ (solid, black), 46 (dashed, red), 48 (long-dashed, green), 50 (dashed-dotted, blue), 51 (long- dashed-dotted, magenta) and four parameters are fixed *i.e.*, $x_A^2 = 0.75, \psi_A = 55, F = 0.75, q = 500, \xi = 1$ for all the curves. Panel (a) streamline on the xz-plane, (b) logM^2, (c) v_p, (d) v_ϕ, (e) μ_S and μ_M, (f) L_B and L_M, (g) γ, (h) log$T$ and (i) Γ versus log$z$. Here, solid circles and triangles represent Alfvén and fast point locations (Singh & Chattopadhyay, 2019b).

5.4.4 Solutions for different Alfvén point cylindrical radius (x_A)

In Fig. 5.5, we plot outflow solutions for different values of $x_A^2 = 0.25$ (solid, black), 0.35 (dashed, red), 0.55 (long-dashed, green), 0.70 (dashed-dotted, blue), 0.90 (long-dashed-dotted, magenta). And other parameters which are kept fixed for all the curves are $\theta_A = 50, \psi_A = 55, F = 0.75, q = 500$ and $\xi = 1$. The poloidal (B_p) as well as toroidal magnetic (B_ϕ) fields are higher for flows of higher x_A. However at larger z, both the components of the magnetic field fall faster, compared to that in the flows of lower x_A (see Fig. 5.5 c). Moreover, the component of centrifugal and magnetic forces along the streamline ($F_{C\parallel}$ & $F_{B\parallel}$) are larger for higher values of x_A. On the other hand, collimation is achieved due to the competition between the components of magnetic ($F_{B\perp}$) and

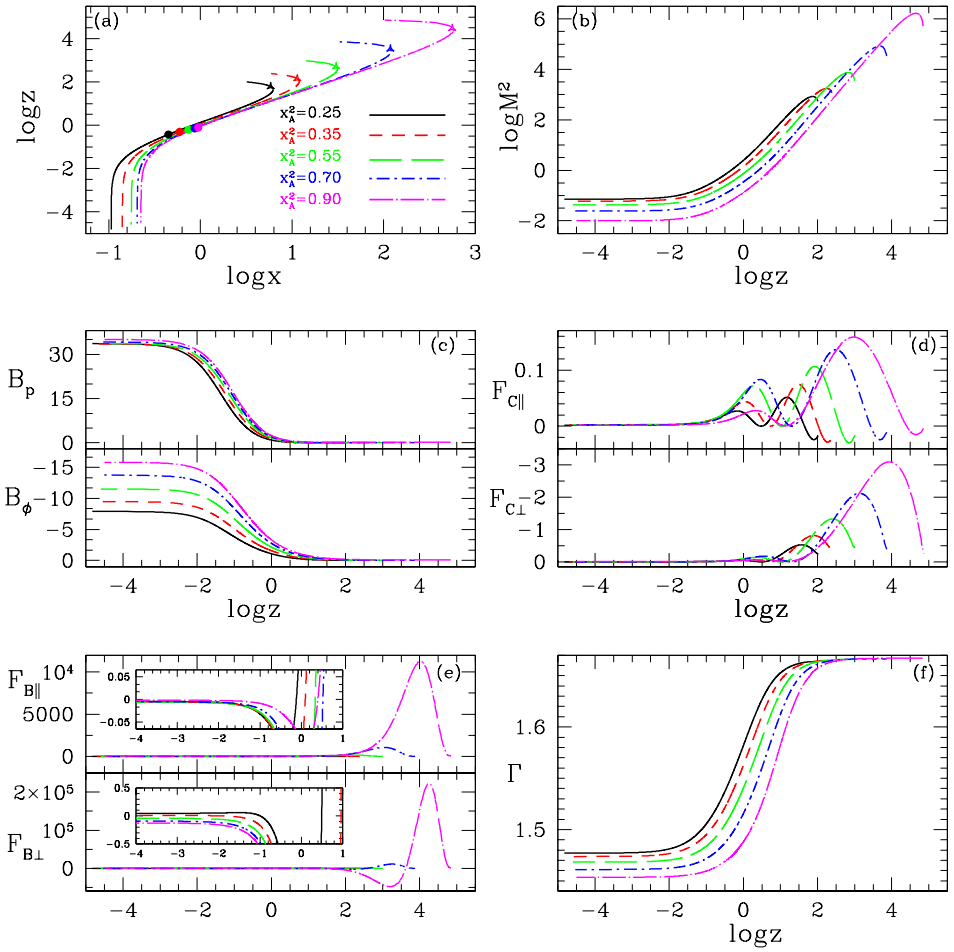

FIGURE 5.5: Outflow solutions are for different values of $x_{\rm A}^2 = 0.25$ (solid, black), 0.35 (dashed, red), 0.55 (long-dashed, green), 0.70 (dashed-dotted, blue), 0.90 (long-dashed-dotted, magenta). All the curves are plotted for fixed values of $\theta_{\rm A} = 50$, $\psi_{\rm A} = 55$, $F = 0.75$, $q = 500$, & $\xi = 1$. Panel (a) streamline on the xz-plane, (b) logM^2, (c) $B_{\rm p}$ and B_ϕ, (d) $F_{\rm C\parallel}$ and $F_{\rm C\perp}$, (e) $F_{\rm B\parallel}$ and $F_{\rm B\perp}$, (f) Γ versus log$z$. Here, solid circles and triangles in panel (a), represent Alfvén and fast point locations. The inset in panel (e) zooms onto various curves corresponding to different values of $x_{\rm A}$. Magnetic field and forces are in arbitrary units (Singh & Chattopadhyay, 2019b).

centrifugal ($F_{\rm C\perp}$) forces orthogonal to the streamline (Fig. 5.5 a, d, e). As a result, solutions corresponding to lower values of $x_{\rm A}$ are more collimated (Fig. 5.5 a), because the resultant of magnetic and centrifugal forces are directed towards the axis, closer to the base than those with larger values of $x_{\rm A}$. This is expected due to the assumption of radial self-symmetry. The Γ distribution along the streamline for different values of $x_{\rm A}$, varies significantly from each other (Fig. 5.5 f). It may be noted that, in almost all the cases, the outflow crosses the light cylinder with impunity.

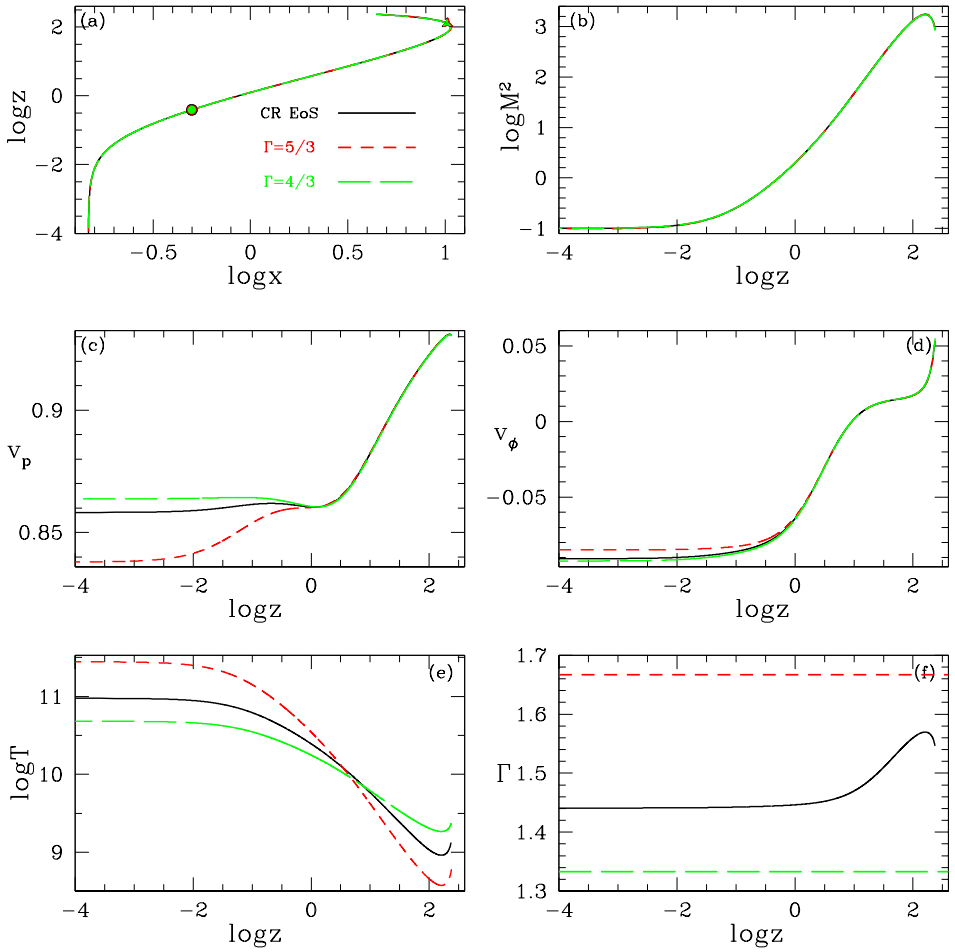

FIGURE 5.6: Outflow solutions with variable adiabatic index CR EoS (solid, black) with $\xi = 1$, fixed adiabatic index EoS with $\Gamma = 5/3$ (dashed, red), and $\Gamma = 4/3$ (long-dashed, green). All curves are plotted for $\mu = 2.82420$, $x_{\rm A}^2 = 0.25$, $\theta_{\rm A} = 52$, $\psi_{\rm A} = 55$, and $F = 0.8$. Panel (a) streamline on the xz-plane, (b) logM^2, (c) $v_{\rm p}$, (d) v_ϕ, (e) log$T$, (f) Γ versus log$z$ (Singh & Chattopadhyay, 2019b).

5.4.5 Comparison of solutions for fixed and variable adiabatic index EoS (CR EoS)

In this section, we compared solutions of fixed adiabatic index EoS (with $\Gamma = 5/3$ and $4/3$) and CR EoS. In Fig. 5.6, we plot outflow solutions for variable adiabatic index EoS or CR EoS (solid, black) with $\xi = 1$ and fixed adiabatic index EoS with $\Gamma = 5/3$ (dashed, red) and $\Gamma = 4/3$ (long-dashed, green). All curves are plotted for $\mu = 2.82420$, $x_{\rm A}^2 = 0.25$, $\theta_{\rm A} = 52$, $\psi_{\rm A} = 55$, and $F = 0.8$. Panel (a) shows the streamline on the xz-plane, (b) logM^2, (c) $v_{\rm p}$, (d) v_ϕ, (e) log$T$, (f) Γ versus log$z$. In Fig. 5.6 (a), the streamlines of all the outflow solutions for different EoS are same. Interestingly, all the solutions also pass through both Alfvén and fast critical points. These solutions also have almost similar Alfvén Mach number distribution (Fig. 5.6 b). However, in Fig. 5.6

(c), we can see that there is significant difference in the poloidal velocity and these solutions also have different values of azimuthal velocity (Fig. 5.6 d). The solutions using CR EoS, cannot be scaled with any particular fixed value of Γ. This has been shown in many papers in the hydrodynamic (radiation hydrodynamic) limit (Chattopadhyay & Ryu, 2009; Chattopadhyay & Kumar, 2016; Kumar & Chattopadhyay, 2017; Vyas & Chattopadhyay, 2019). As is expected, solutions of different EoS have different overall temperature variation (Fig. 5.6 e). In Fig. 5.6 (f), we present the variation of adiabatic index for CR EoS and the comparison with fixed adiabatic index. For solutions with different EoS, $T(r)$ crosses each other at some distance and yet, Γ computed from CR EoS, is neither $5/3$ nor $4/3$. It is clear by comparing Fig. 5.6 (e, f), that, the temperature obtained by using $\Gamma = 4/3$ is less than that obtained by using $\Gamma = 5/3$, which clearly should not be the case. Since, only very hot plasma should be described by $\Gamma = 4/3$ and cold plasma ($T < 10^7$K, i.e., $T << m_{\rm e^-}c^2/\kappa_{\rm B}$) should be described by $\Gamma = 5/3$, therefore, relativistic flows described by fixed Γ EoS clearly has a temperature discrepancy.

5.4.6 Solutions for different plasma compositions (ξ)

In Fig. 5.7 we have presented outflow solutions for different compositions, $\xi = 1.0$ (solid, black) is electron-proton, 0.8 (dashed, red), 0.5 (long-dashed, green), 0.3 (dashed-dotted, blue), 0.1 (long-dashed-dotted, magenta) and other five parameters are fixed *i.e.*, $x_{\rm A}^2 = 0.25, \theta_{\rm A} = 50, \psi_{\rm A} = 55, F = 0.75, q = 500$. In these solutions μ and $\sigma_{\rm M}$ increases slightly with the increase in ξ, if $x_{\rm A}$, $\theta_{\rm A}$, $\psi_{\rm A}$ and q are kept constant. It is also reflected in the plots of $\mu_{\rm S}$ and $\mu_{\rm M}$, as well as $L_{\rm B}$ and $L_{\rm M}$ (Fig. 5.7 e, f). There is very little difference in the streamlines of the jets (Fig. 5.7 a). However, by varying the composition of the flow from electron-proton plasma (*i.e.*, $\xi = 1.0$) to pair dominated flow $\xi = 0.1$, $v_{\rm p}$ and v_ϕ of the flow varies significantly with ξ (Fig. 5.7 b, c). Even $\mu_{\rm S}$, $\mu_{\rm M}$ and $L_{\rm B}$, $L_{\rm M}$ also depend on ξ (Fig. 5.7 d, e). Since ξ also influences the thermodynamics of the flow, the temperature of the jet is also crucially influenced by its composition. As a result the adiabatic index Γ also depends on ξ (Fig. 5.7 f). It may be noted, that the temperature of pair-dominated flow is higher than electron-proton flow and therefore Γ at any given z is lower for flows with lower value of ξ. Since we are comparing flows with same $x_{\rm A}$ (equivalently, $M_{\rm A}$), therefore from equation (5.14), it can be easily shown that the temperature of pair dominated flow will be higher.

In Fig. 5.8, we plot magnetized outflow solutions for different compositions like $\xi = 1.0$ (solid, black), 0.5 (dashed, red) and 0.1 (long-dashed, green), but are for the

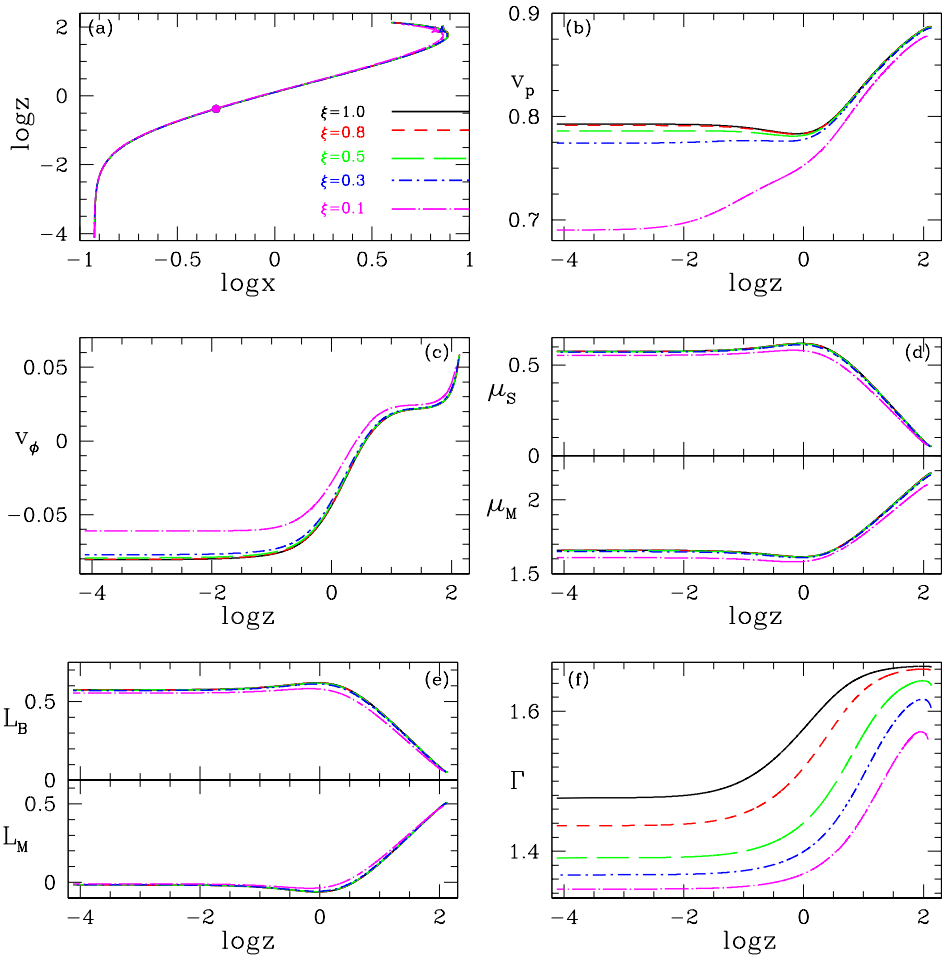

FIGURE 5.7: Outflow solutions for different values of $\xi = 1.0$ (solid, black), 0.8 (dashed, red), 0.5 (long-dashed, green), 0.3 (dashed-dotted, blue), 0.1 (long-dashed-dotted, magenta). All the curves are plotted for $x_{\rm A}^2 = 0.25$, $\theta_{\rm A} = 50$, $\psi_{\rm A} = 55$, $F = 0.75$, and $q = 500$. Panel (a) streamline on the xz-plane, (b) $v_{\rm p}$, (c) v_ϕ, (d) $\mu_{\rm S}$ and $\mu_{\rm M}$, (e) $L_{\rm B}$ and $L_{\rm M}$, (f) Γ versus log$z$. Here, solid circles and triangles represent Alfvén and fast point locations (Singh & Chattopadhyay, 2019b).

same $\mu = 2.23362$, $\theta_{\rm A} = 50$, $\psi_{\rm A} = 55$, $F = 0.75$, and $q = 500$. So all these solutions are for the same Bernoulli parameter μ. Since all other parameters are same, the magnetic field components and streamlines for each are almost the same (Fig. 5.8 a, c), yet $v_{\rm p}$ & v_ϕ (Fig. 5.8 b, d) distribution are completely different for flows with different ξ. Moreover, even the temperature (T) and Γ also depend on the composition parameter (Fig. 5.8 e, f). The baryon poor outflows which have same Bernoulli parameter, are slower and hotter, compared to electron-proton flow. However, the gain in $v_{\rm p}$ is more for pair dominated flow than the electron-proton flow.

In Fig. 5.9, we plot magnetized outflow solutions for different compositions like $\xi = 1.0$ (solid, black), 0.5 (dashed, red) and 0.1 (long-dashed, green), but are for the same $L = 0.55585$, $\theta_{\rm A} = 50$, $\psi_{\rm A} = 55$, $F = 0.75$, and $q = 500$, i. e., we compare outflows

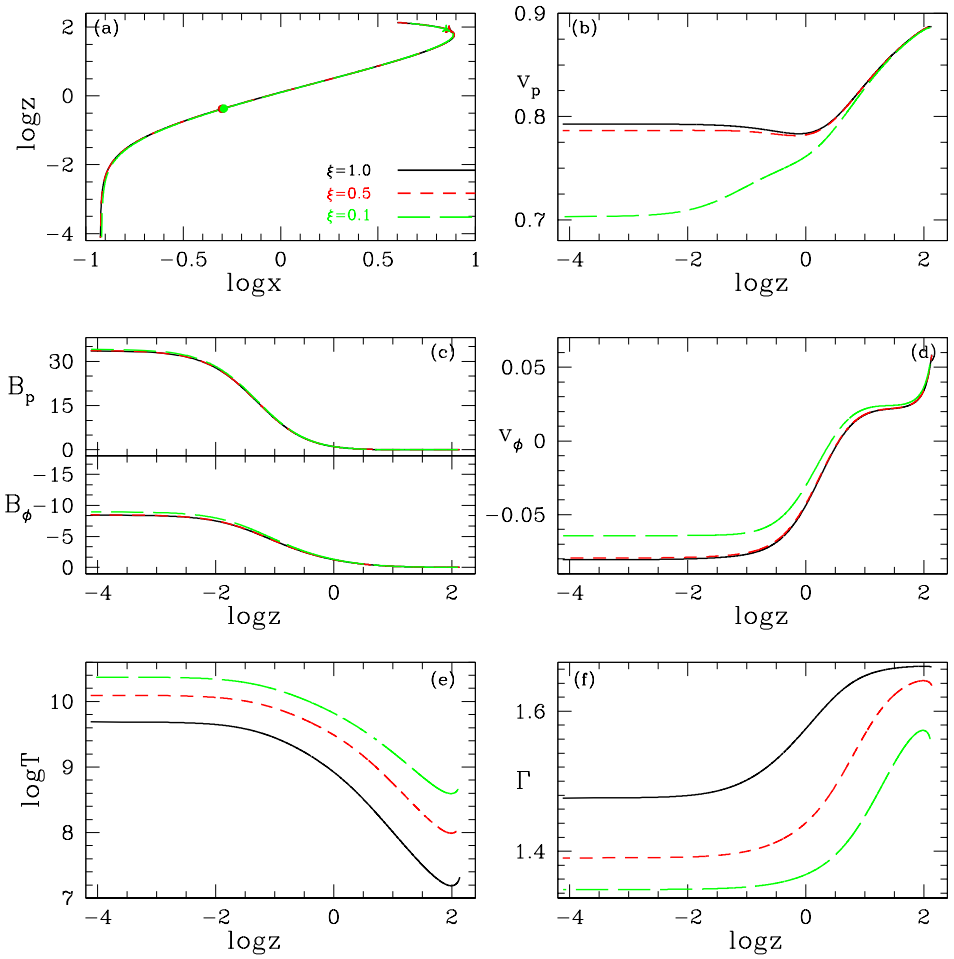

FIGURE 5.8: Outflow solutions for different values of $\xi = 1.0$ (solid, black), 0.5 (dashed, red) and 0.1 (long-dashed, green). All the curves are plotted for $\mu = 2.23362$, $\theta_{\rm A} = 50$, $\psi_{\rm A} = 55$, $F = 0.75$, and $q = 500$. Panel (a) streamline on the xz-plane, (b) $v_{\rm p}$, (c) $B_{\rm p}$ and B_ϕ, (d) v_ϕ, (e) log$T$, (f) Γ versus log$z$ (Singh & Chattopadhyay, 2019b).

launched with the same total angular momentum (or L) but different ξ. The streamlines are again almost the same (Fig. 5.9 a), however, $v_{\rm p}$, v_ϕ, and T or Γ (Fig. 5.9 b-f) are significantly different for flows with different ξ.

It may be remembered that the general expression of constants of motion μ and L in physical units are (see equations 5.12 and 5.11),

$$\mu = h\gamma - \frac{\varpi\Omega B_\phi}{\Psi_{\rm A} c^2};\ L = \varpi\gamma h v_\phi - \frac{\varpi B_\phi}{\Psi_{\rm A}}$$

From equation (2.15), it is also clear that h depends on composition parameter ξ. So, for a given μ or L, if B_ϕ is somewhat similar at the base, then γ (*i.e.*, $v_{\rm p}$, v_ϕ) and Θ will depend on ξ. That is exactly what we see in Figs. 5.8 & 5.9. Dependence of flow velocity and temperature on the composition of the flow, has also been shown in the

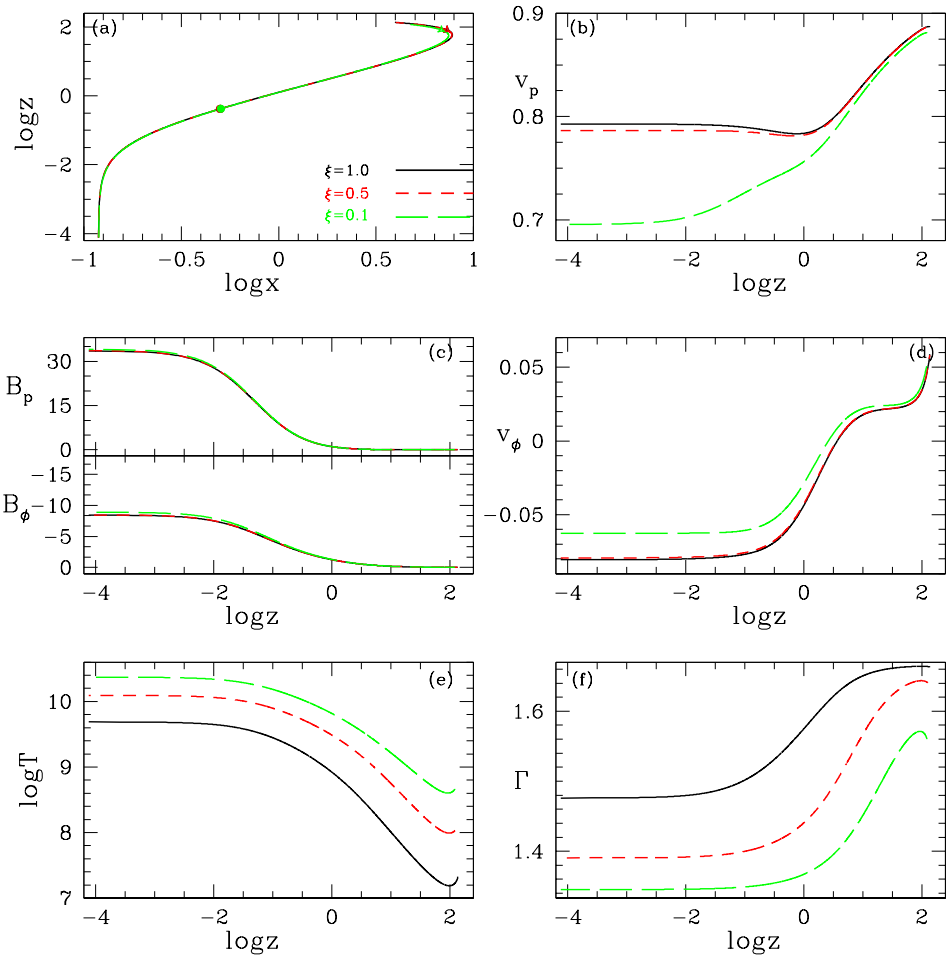

FIGURE 5.9: Outflow solutions for different values of $\xi = 1.0$ (solid, black), 0.5 (dashed, red), 0.1 (long-dashed, green). All the curves are plotted for $L = 0.55585$, $\theta_{\rm A} = 50$, $\psi_{\rm A} = 55$, $F = 0.75$, and $q = 500$. Panel (a) streamline on the xz-plane, (b) $v_{\rm p}$, (c) $B_{\rm p}$ and B_ϕ, (d) v_ϕ, (e) log$T$, (f) Γ versus log$z$ (Singh & Chattopadhyay, 2019b).

hydrodynamic regime recently (Chattopadhyay & Ryu, 2009; Chattopadhyay & Kumar, 2016; Vyas & Chattopadhyay, 2019; Sarkar & Chattopadhyay, 2019). Therefore, it is expected that some imprint of the flow composition should be there in radiative output of the flow.

In Fig. 5.10, we plot an electron-positron outflow solution or flow having $\xi = 0.0$. Other parameters are $x_{\rm A}^2 = 0.75$, $\theta_{\rm A} = 50$, $\psi_{\rm A} = 55$, $F = 0.75$, and $q = 0.05$. From Fig. 5.10 (b), it is clear that pure leptonic flow is also a trans-fast flow and the velocity nature is similar to proton poor flows as plotted in Fig. 5.8 (b). In Fig. 5.10 (d), we plot the forces which control the poloidal acceleration of the flow, for example, parallel inertial force $F_{\rm I\parallel}$, parallel gamma force $F_{\rm G\parallel} \equiv F_{\rm GP\parallel} + F_{\rm G\phi\parallel}$, parallel total thermal gradient force $F_{\rm TP\parallel} \equiv F_{\rm T\parallel} + F_{\rm P\parallel}$, parallel centrifugal force $F_{\rm C\parallel}$, and parallel magnetic force $F_{\rm B\parallel}$ (see equation C.5 in Appendix C). In the inset of Fig. 5.10 (d), we can note that these

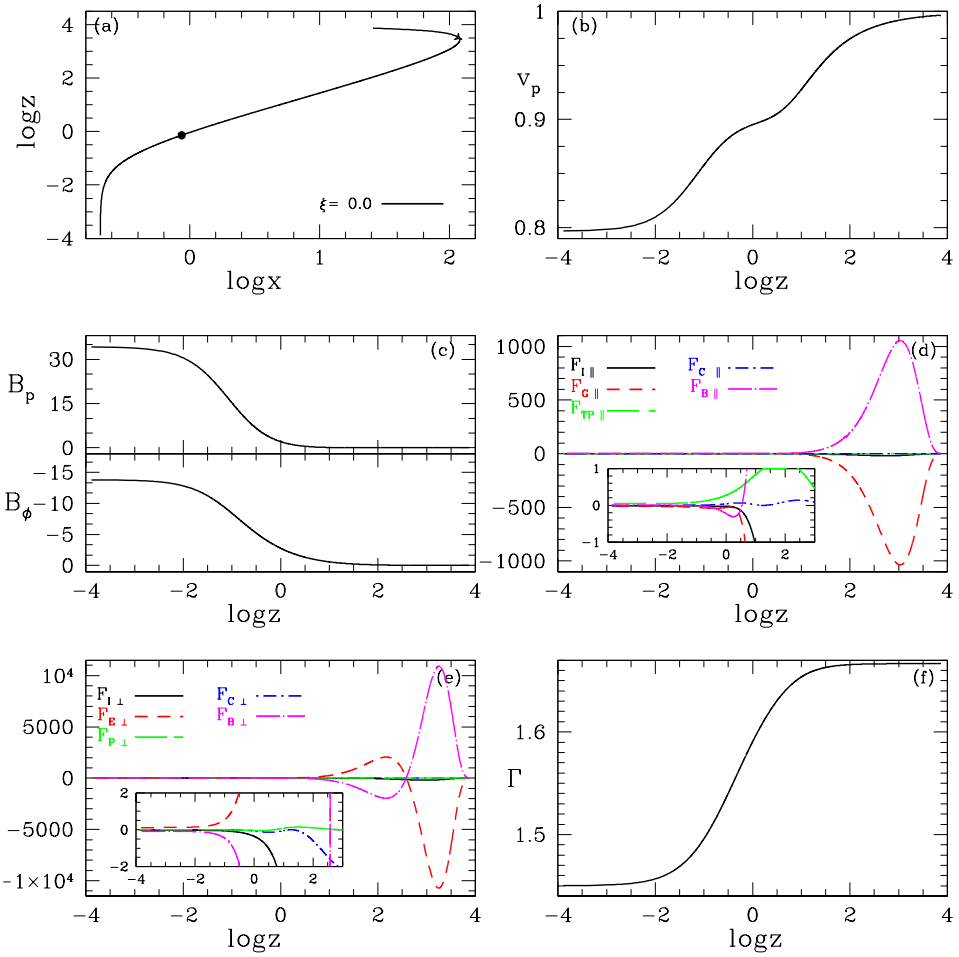

FIGURE 5.10: Outflow solutions for composition $\xi = 0.0$. All the curves are plotted for $x_{\rm A}^2 = 0.75$, $\theta_{\rm A} = 50$, $\psi_{\rm A} = 55$, $F = 0.75$, and $q = 0.05$. Panel (a) streamline on the xz-plane, (b) $v_{\rm p}$, (c) $B_{\rm p}$ and B_ϕ, (d) parallel forces, (e) perpendicular forces, (f) Γ versus log$z$ (Singh & Chattopadhyay, 2019b).

forces are comparable to each other at lower value of z, however for greater value of z, $F_{\rm B\parallel}$ and $F_{\rm G\parallel}$ forces are controlling the poloidal acceleration. In Fig. 5.10 (e), we plot all forces perpendicular (see equation C.6 in Appendix C) to the poloidal magnetic field line, e. g., $F_{\rm I\perp}$ (inertial), $F_{\rm E\perp}$ (electric), $F_{\rm P\perp}$ (pressure gradient), $F_{\rm C\perp}$ (centrifugal), and $F_{\rm B\perp}$ (magnetic). Perpendicular forces have similar nature to parallel forces, however, at a larger distances, $F_{\rm E\perp}$ and $F_{\rm B\perp}$ controls the collimation of the flow. In Fig. 5.10 (f), the adiabatic index for pure lepton flow varies from ~ 1.44 to $\sim 5/3$.

5.5 Discussion and Concluding Remarks

In this analysis, we have solved the relativistic magneto-hydrodynamic equations using the relativistic equation of state, in order to study relativistic outflows. A flow is

relativistic on account of its bulk velocity (i.e., $v_{\rm p} \lesssim c$) and also in terms of its temperature i.e., when $\kappa_{\rm B} T \gtrsim m_i c^2$ (subscript i represents the type of constituent particle). The first condition arises for outflows, far away from a black hole, but the second condition especially arises in the region close to a black hole horizon which acts as the base of an astrophysical jet. A form of an EoS (CR) for a flow which can transit between relativistic to non-relativistic temperatures has been used in this study. As has been discussed throughout this chapter, Γ is a function of temperature in CR EoS and is automatically determined from temperature distribution. There are a few papers in hydrodynamic regime (read in absence of ordered magnetic field) which discusses the application of relativistic EoS in accretion and jets (Chattopadhyay & Kumar, 2016; Kumar & Chattopadhyay, 2017; Vyas & Chattopadhyay, 2019). However, as far as we know, there have been no such previous attempts to solve relativistic, trans-Alfvénic, trans-magneto sonic plasma expressed by relativistic EoS and study the effect of different compositions of the plasma. Since MHD equations are only applicable for fully ionized plasma, therefore, the composition of the flow is likely to either be electron-proton ($\xi = 1$) plasma or electron-positron-proton ($0 < \xi < 1$) plasma. In this chapter, we have studied how various parameters like the Bernoulli constant, current distribution, the location of the Alfvén point, etc. affect the outflow solution but only for electron-proton plasma. And then studied the effect of different EoS and different compositions on outflow solutions.

We investigated the contribution played by all the flow parameters, information of which shapes the final solution of the outflow. We found that the current distribution affects the streamline structure, as well as the flow velocities, especially close to the base. We also found that, not only the current distribution, the angle of the poloidal magnetic field line makes with the equatorial plane also affect the solutions. In particular, the streamlines which are more inclined to the equatorial plane are slower and less collimated. In addition, narrower the polar angle of the Alfvén point with the axis of the flow, slower and less collimated is the outflow. These two angles, namely $\psi_{\rm A}$ and $\theta_{\rm A}$ are independent of each other. For a given composition, the location of the Alfvén point has significant effect on the Bernoulli parameter μ, the streamline and the Lorentz factor of the flow. We found that while the q parameter which depends on the entropy, itself does not affect the outflow solutions significantly except the temperature, but in conjunction with other parameters plays an important role.

We have also compared the outflow solutions using fixed adiabatic index EoS, with

the one using CR EoS for a given value of μ, $x_{\rm A}$, $\theta_{\rm A}$, $\Psi_{\rm A}$ and F. Although the streamlines are similar, but the distribution of flow variables ($v_{\rm p}$, v_ϕ, and T) are significantly different. Interestingly, solutions of all the EoS, are passed through both the critical points (Alfvén and fast magnetosonic). It may be noted, that Vlahakis *et al.* (2003a,b) only obtained trans-Alfvénic outflow using $\Gamma = 4/3$, but Polko *et al.* (2010) obtained trans-Alfvénic, trans-fast outflow solutions using $\Gamma = 5/3$. However, we showed that even with $\Gamma = 4/3$, one can obtain trans-Alfvénic, trans-fast outflow solution (Fig. 5.6 a). It appears that, depending on the values of other parameters, there exists a critical value of F, below which the flow passes through both the critical points, but for higher values of F, the outflow is only trans-Alfvénic in nature. For example for the parameters related to Fig. 5.1, trans-Alfvénic, trans-fast outflow is possible if $F < 0.82$.

We showed that, jets of all composition passes through the Alfvén and the fast point, and get collimated to the axis after crossing the fast point. We compared solutions with different composition, but for the same values of the Alfvén point, or the Bernoulli constant, or the total angular momentum. In all the cases, composition has little effect on the streamlines, but $v_{\rm p}$, v_ϕ and T distributions are significantly different. It means that the electro-magnetic output of such outflows should also depend on the composition. Since pair-plasma have been regularly invoked as the composition of jets, we have also presented one case of pure pair plasma (i. e., $\xi = 0.0$) outflow solution and it nicely passes through both the critical points. The pair plasma outflow accelerates mainly in the sub-Alfvénic region to super-fast region. The effect of composition is quite pronounced in presence of gravity as was seen in the hydrodynamic limit (Chattopadhyay & Ryu, 2009; Kumar & Chattopadhyay, 2013; Chattopadhyay & Kumar, 2016) as well as, in the non-relativistic MHD regime (Singh & Chattopadhyay, 2018a,b, 2019a). So we expect the effect of CR EoS will be more pronounced in the SMHD limit, if gravity is considered. However, consideration of gravity is beyond the scope of this analysis. It may be noted that SMHD equations combined with pseudo-Newtonian gravity have been used to study outflows previously, with very interesting results (Polko *et al.*, 2013, 2014; Ceccobello *et al.*, 2018). In this study, the jet only passes through two critical points (Alfvén and fast) and not the slow. The slow point appears in presence of gravity. The existence of slow-magnetosonic point ensures low velocity and high temperature at the base of jet, or in other words, corrects the boundary condition at the jet base.

In all the solutions, the jet streamlines show that there is a possibility that after crossing the fast point, over collimation/magnetic field pinching can produce shock. Since the flow is moving with super-fast speed, so formation of shock is not going to

affect the flow in the upstream and this shock location can be related to the fast point location. In the case of M87, Asada & Nakamura (2012) showed that jet radius versus jet height nicely fit parabolic curve up to $5 \times 10^5 r_{\rm g}$ height and after this jet radius versus height follows conical structure. There is a dip in jet radius near the HST-1 which is located at $5 \times 10^5 r_{\rm g}$ *i.e.,* jet radius versus height departs from the parabolic structure and this may be due to collimation shock.

Chapter 6

Conclusions

6.1 Major outcomes

In this thesis, a detailed study has been carried out for three astrophysical processes, magnetized accretion, wind outflows, and jets which occurs around astrophysical objects. We treated these systems in magnetohydrodynamic (MHD) as well as special relativistic magnetohydrodynamic (SMHD) regime in Newtonian potential (NP), and in pseudo-Newtonian potential or Paczyński & Wiita (1980) potential (PWP). We also compared our results by using fixed as well as variable adiabatic index EoS (CR EoS). As an example of magnetized accretion, we focused on the accretion process onto magnetized compact object with hard surface like neutron star and white dwarfs. Although we have mentioned the conclusions at the end of each chapter, here we summarize the major results of these studies.

6.1.1 Multiple shocks in magnetized accretion flow onto neutron stars and white dwarfs

In magnetized accretion, we have shown that with the inclusion of cooling (cyclotron and bremsstrahlung processes) using fixed adiabatic index and CR EoS, it is possible to connect the flow from the accretion disc to the star's surface (neutron star and white dwarf) through strong magnetic field lines. When this flow hits the hard surface of the star, it forms a very strong surface shock (compression ratio ~ 6). The cooling process radiates the shock energy and slows down the flow to a negligible velocity. We have found that bremsstrahlung emission dominates far from the star and near the star's

surface, however, cyclotron emission dominates from pre-shock to near post-shock region of primary surface shock (Fig. 3.9). The total luminosity has also been calculated *e.g.,* for NSs, 10^{34-36}erg s^{-1}. For a small parameter range (energy and rotation period), there is also secondary weak shock along with primary surface shock. Even though secondary shock is weak but the oscillations in the secondary shock, in principle, can perturb the primary surface shock and make it time dependent. We have studied magnetized accretion flow onto WD and our results (*e.g.,* shock height, shock temperature, etc.) have a good match with the observation (section 3.4.3.2).

6.1.2 Effect of magnetic field on the dynamics

We have discussed the magnetic field is present everywhere in space and varies for a wide range. Strong magnetic field controls the accretion process in case of NSs and WDs by channelling the flow along with itself. It also affects the cyclotron emission and hence the parameter space (see Figs. 3.3 c & 3.6 c). In the case of wind outflows, the magnetic field highly affects its structure (Fig. 4.6). A low angular momentum wind is blown out radially by the magnetic field and a high angular momentum wind has spiral streamlines close to the central object, as matter moves outward, streamlines become radial. Magnetic field also play a pivotal role in case of jets (shown in Chapter 5). We have found that magnetic field accelerates the flow to a high velocity (some cases $\gamma \sim 40$) and at the same time, magnetic field also collimates the flow along the rotation axis (see Fig. 5.1). This over collimation can produce shock due to magnetic field pinching, because after the fast point, flow is disconnected transonically, therefore if shock is formed after the fast point then it will not be going to affect the flow below it. So we can relate the shock location to the fast point in case of jets.

6.1.3 Effect of plasma composition on astrophysical flows

Plasma composition is very important while studying flows because it directly affects the inertia and thermal energy of the system. We have found that the flow variables (*e.g.,* velocity, temperature, etc.) highly depend on plasma composition. In magnetized accretion, we have shown that for the same set input parameters, electron-proton flow has higher temperature and double shocks as compared to lepton dominated flow (Fig. 3.15). The terminal speed of wind outflow also depends on the plasma composition. The terminal speed of the wind outflow has maximum value for certain plasma composition for given energy (Fig. 4.11). For lower energy winds, the terminal speed

maximizes for plasma composition having higher proton proportion, and for higher energy winds, the terminal speed maximizes for lepton dominated plasma. In case of collimated outflows or jets, it seems that plasma composition has no effect on the jet collimation but it affects the poloidal velocity, azimuthal velocity, and temperature of the flow in sub-Alfvénic to the super-fast regime (see section 5.4.6).

6.1.4 Importance of relativistic EoS

We have mainly used CR EoS in our study of astrophysical flows due to its simplicity and accuracy. CR EoS has temperature dependent Γ (specific heat ratio), therefore it is being calculated throughout the solution. Another important point is, CR EoS allows to control the composition of flow, so we have studied the effect of plasma composition on astrophysical flows. We have shown that fixed adiabatic index EoS gives very different results in systems having broad range of temperatures (section 5.4.5), so EoS having temperature dependent adiabatic index is necessary while studying the dynamics of astrophysical flows.

6.1.5 Nature of critical points in HD and MHD

In the case of HD, a critical point forms due to the balance between thermal pressure gradient and gravity (see section 2.5.1). Presence of angular momentum modifies the gravity to allow the formation of MCP. Usually, a transonic solution only passes through single critical point (inner or outer critical point), however, in the presence of shock, it can pass through multiple critical points. In the case of MHD, a critical point (Alfvén critical point) forms even if gravity is off. Multiple critical points (Alfvén and fast critical point) form if the matter has non-zero angular momentum (see Fig. 5.1). However, the presence of gravity gives rise to slow critical point and we have found a maximum five critical points in wind outflow (see Fig. 4.1). Another thing is, in MHD, a transonic solution passes through three critical points (slow, Alfvèn, fast points) and these critical points have the same entropy (see Fig. 4.2). It means, these three critical points through which a transonic solution passes in MHD is analogous to a transonic solution passing through a single critical point in case of HD.

6.1.6 Significance of strong gravity

In magnetized accretion flow, we have found that accretion solutions in Newtonian gravity are alpha-type for most of the parameter (energy, rotation period) range *i.e.*, they

have two critical points, one is O-type and another is X-type. Only for a small parameter range, we have accretion solutions which reach neutron star radius. However, in string gravity (using PWP), a magnetized accretion solution can have three critical points, one is O-type and two are X-type, and all the solutions of any parameter range reach the star's surface without any problem (section 3.4.1 and Appendix A). The inner X-type critical point occurs due to the presence of strong gravity. These multiple critical point solutions can also harbour multiple shocks. In case of wind outflows, we have found that velocity is very small near the object and terminal velocity is higher in PWP as compared to NP (Fig. 4.8).

6.2 Further implications and limitations

In the work presented in this thesis, we develop a model for magnetized accretion flow onto compact objects which connect the matter from the disc to the object's surface and could explain the hot spot radiation which is usually observed in these kinds of flows. Other crucial results are that plasma composition affects the flow variables in case of magnetized accretion, wind outflows and jets, and the choice of EoS highly affects the behaviour of solutions. These results could help to estimate the plasma composition of astrophysical flows, and would give better insight.

Although this study has wide range of implications in astrophysical flows but it also has some limitations. For example, PWP mimics the Schwarzschild black hole gravity but it blows up at the event horizon, giving rise to high temperatures as compared to general relativity. In magnetized accretion, the strong magnetic field assumption restricts the analysis to poloidal flow but azimuthal flow is also important because it could explain the transport of angular momentum between the star and the flow. In case of collimated outflows or jets, we have ignored the gravity and hence are not able to study the behaviour of outflows near the disc plane. The radially self-similar assumption in jet study gives opposite temperature behaviour for $\Gamma = 5/3$ and $\Gamma = 4/3$. Some recent studies have shown that self-similarity breaks down for outflows in the presence of gravity.

In conclusion, this study shows that the magnetic field highly affects and defines the dynamics of astrophysical flows (accretion, wind outflows, and jets) and the relativistic EoS (which has temperature-dependent Γ and composition parameter *e.g.,* CR EoS) is necessary while studying astrophysical flows. Such conclusions are inspiring

and it points to another set of interesting problems, some of which are enumerated below:

- Study magnetized accretion of neutron star and wind outflows from compact object in GRMHD regime.
- Gravity highly affects jet at the base. We have been working to extend the study of Chapter 5 by including gravity and studying magnetized jets from the base or from near the central object.
- We know the spectrum from the astrophysical objects (*e.g.,* AGN, accreting neutron stars, GRBs, etc.) are time-dependent. We will use the knowledge of steady state semi-analytical solutions to set the initial condition and boundary conditions of MHD simulation codes, to study magnetized astrophysical flow around compact objects.

Appendix A

Comparison between Newtonian and Paczyński-Wiita gravity and the different EoS

Here we compare solutions obtained by assuming (I) Newtonian potential (NP) and fixed Γ EoS of the flow, with those obtained by using (II) Paczyński-Wiita potential (PWP) and CR EoS. It is to be remembered that the solutions of Koldoba *et al.* (2002) is the reference for type I solutions. As has been mentioned in section 3.1, the solutions of Koldoba *et al.* (2002) ignore cooling, so to compare we also ignored cooling for both I and II type solutions. The mathematical structure and solution methodology is exactly the same as those mentioned in the main text. Since the equation (see in section 2.4.2) is quite different than CR EoS, and moreover, does not contain the information of rest mass energy density, therefore, the value of the Bernoulli parameter as well as, the entropy accretion rate is quite different. Moreover, the unit system was chosen by (Koldoba *et al.*, 2002) is also different from this analysis. The unit of velocity chosen in this analysis and type II solutions is c, while that of type I and Koldoba *et al.* (2002) is $\Omega r_{\rm d}$. To convert of $\mathcal{B}$ from Koldoba *et al.* (2002) to ours, we first obtain $\mathcal{B}$ in terms of physical units and then divide that with c^2. Moreover since EoS of type I solutions do not contain the information of rest energy density we added it to make it comparable to the $\mathcal{B}$ of type II solutions. Moreover, similar to Fig. 4 (a) of Koldoba *et al.* (2002), for type I solutions, we choose $\Gamma = 5/3$ as the representative case.

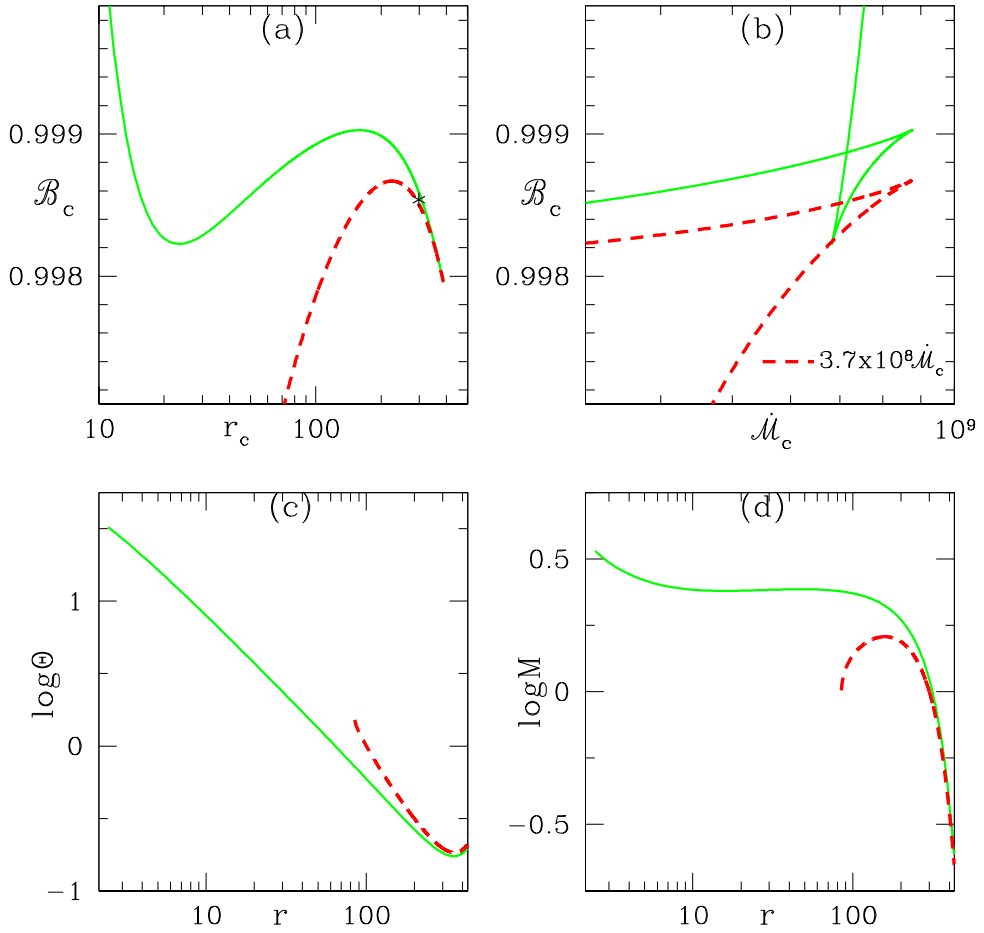

FIGURE A.1: Sonic point properties: (a) $\mathcal{B}_c$—r_c and (b) $\mathcal{B}_c$—$\dot{\mathcal{M}}_c$. Solutions: (c) logΘ, (d) log$M$ as a function of r for flow parameters $\mathcal{B} = 0.9985$ and $P = 1$s (star mark in panel a). Each curve compares type I solution *i.e.,* fixed Γ $(= 5/3)$ EoS and Newtonian potential (dashed, red) and type II or those with CR EoS and PW gravitation potential (solid, green). In both the solutions cooling is ignored. (Singh & Chattopadhyay, 2018b)

In Fig. A.1 (a) we plot $\mathcal{B}_c$ as a function of r_c for an NS of $P = 1$s. For the type I case (dashed, red), there is only a maximum, but for type II (solid, green) case there is a maximum and a minimum. Therefore for a given $\mathcal{B} = \mathcal{B}_c$ within the maximum and the minimum value, there can be three sonic points for type II solution, but only two sonic points for the type I case. This is the effect of PWP over the NP. A stronger gravity ensures the formation of the inner sonic point. The star mark corresponds to the value $\mathcal{B} = 0.9985$. Fig. A.1 (b) reconfirms the same fact that the inner sonic point does not form for type I solutions. In order to make the entropy-accretion rate of type I solutions comparable with that of type II, a large factor is multiplied with the former. Sonic point properties are fundamentally different between type I and II cases. For $P = 1$s, type I solutions have limited range of $\mathcal{B}$ which connect r_d and $R_\circ$. But for type II case, global

solutions connecting $r_{\rm d}$ and $R_\circ$ can be obtained for all available $\mathcal{B}$. In Fig. A.1 (c) we compare logΘ with r for type I (dashed, red) and type II (solid, green) solutions. Type I solution terminates before reaching the star surface. In Fig. A.1 (d) we compare log$M$ with r. Since type I solution has two sonic points, an outer X type, and a middle O-type, therefore the accretion solution does not reach the star ($M \to 1$ at $r > R_\circ$). Type II solution is global. Since Koldoba *et al.* (2002) did not compute shocks, so we just present the transonic solution. The M distribution of type II solution indicates the presence of middle and inner sonic points (regions where $dM/dr \to 0$). Since we have ignored cooling in the results presented in this appendix, therefore, we see the temperature monotonically increases inward.

Appendix B

Combination of forces for magnetized outflow

Here we plot the competing combined forces acting on a magnetized wind/outflow. The thermal force is $F_{\rm T}$, rotational force is $F_{\rm R}$, $F_{\rm G}$ is the gravitational and $F_{\rm M}$ is the

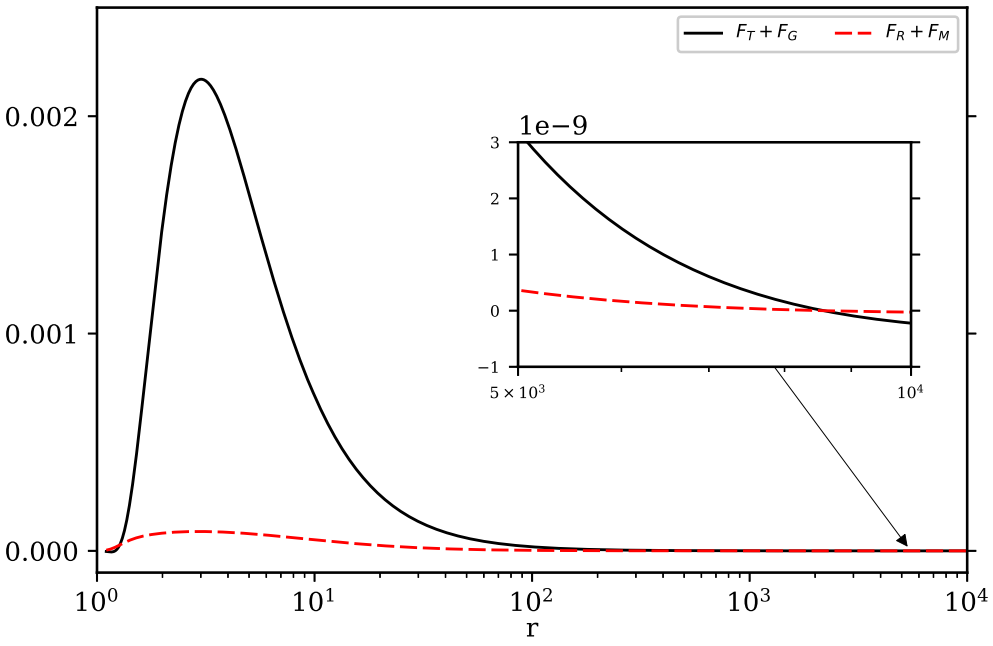

FIGURE B.1: Comparison of combination of forces thermal and gravitational $F_{\rm T} + F_{\rm G}$ (solid, black) and rotational and magnetic forces $F_{\rm R} + F_{\rm M}$ (dashed, red) along the streamline. The flow parameters are $E = 1.03075$, $L = 1.0$ and $\xi = 1.0$ same as Fig. 4.3 (Singh & Chattopadhyay, 2019a).

magnetic force along the streamline, as is described in connection with Fig. 4.3 (d). We plot $F_{\rm T}+F_{\rm G}$ (solid, black) and $F_{\rm R}+F_{\rm M}$ (dashed, red) in Fig. B.1 in order to compare the competing forces. Clearly, $F_{\rm R}+F_{\rm M}$ is comparable $F_{\rm T}+F_{\rm G}$ close to the central object where it is launched, but is larger at very large distances. However, $F_{\rm T}+F_{\rm G}$ dominates over the other combination very close to the central object till unto a hundred $r_{\rm g}$.

Appendix C

Equations of motion for outflows

The Bernoulli equation ($\mu = \gamma h - \varpi \Omega B_\phi / \Psi_{\rm A} c^2$) is obtained from the identity $\gamma^2 \left(1 - v_\phi^2/c^2\right) = 1 + \gamma^2 v_p^2/c^2$ (for more details see Vlahakis *et al.*, 2003a),

$$\mu^2 = \left(h^2 + \frac{F^2 \sigma_{\rm M}^2 M^4 \sin^2(\theta)}{x^4 \cos^2(\theta+\psi)}\right) \times \left(\frac{G^4 (1 - M^2 - x^2)^2}{G^4 (1 - M^2 - x_{\rm A}^2)^2 - x^2 (G^2 - M^2 - x^2)^2}\right). \tag{C.1}$$

Because $\tan(\psi) = \frac{\partial z}{\partial \varpi} = \frac{d(G/\tan(\theta))}{dG}$, therefore we have,

$$\frac{dG^2}{d\theta} = \frac{2G^2 \cos(\psi)}{\sin(\theta)\cos(\theta+\psi)}. \tag{C.2}$$

The momentum balance equation (5.4) is basically sum of forces (see Vlahakis *et al.*, 2003a),

$$\mathbf{F}_{\rm G} + \mathbf{F}_{\rm T} + \mathbf{F}_{\rm C} + \mathbf{F}_{\rm I} + \mathbf{F}_{\rm P} + \mathbf{F}_{\rm E} + \mathbf{F}_{\rm B} = \mathbf{0}, \tag{C.3}$$

where,

$$\begin{aligned}
\mathbf{F}_{\rm G} &= -\gamma \rho h (\mathbf{v}.\boldsymbol{\nabla}_{\rm s} \gamma)\mathbf{v}, \\
\mathbf{F}_{\rm T} &= -\gamma^2 \rho (\mathbf{v}.\boldsymbol{\nabla}_{\rm s} h)\mathbf{v}, \\
\mathbf{F}_{\rm C} &= \frac{\gamma^2 \rho h v_\phi^2}{\varpi}\mathbf{e}_\varpi, \\
\mathbf{F}_{\rm I} &= -\gamma^2 \rho h (\mathbf{v}.\boldsymbol{\nabla}_{\rm s})\mathbf{v} - \mathbf{F}_{\rm C}, \\
\mathbf{F}_{\rm P} &= -\boldsymbol{\nabla}_{\rm s} P, \\
\mathbf{F}_{\rm E} &= \frac{(\boldsymbol{\nabla}_{\rm s}.\mathbf{E})\mathbf{E}}{4\pi}, \\
\mathbf{F}_{\rm B} &= \frac{(\boldsymbol{\nabla}_{\rm s} \times \mathbf{B}) \times \mathbf{B}}{4\pi}.
\end{aligned} \tag{C.4}$$

Here, $\mathbf{F}_{\rm G}$ is force due to Lorentz factor or gamma force, $\mathbf{F}_{\rm T}$ is temperature force, $\mathbf{F}_{\rm C}$ is centrifugal force, $\mathbf{F}_{\rm I}$ is inertial force, $\mathbf{F}_{\rm P}$ is pressure gradient force, $\mathbf{F}_{\rm E}$ is electric force and $\mathbf{F}_{\rm B}$ is magnetic force. By projecting equation (C.3) along the poloidal flow we get an equation which describe poloidal acceleration of the flow,

$$-\frac{\gamma^4\rho h v_{\rm p}^2}{2c^2}\frac{dv_{\rm p}^2}{d\ell}-\frac{\gamma^4\rho h v_{\rm p}^2}{2c^2}\frac{dv_\phi^2}{d\ell}-\gamma^2\rho v_{\rm p}^2\frac{dh}{d\ell}+\gamma^2\rho h\frac{v_\phi^2}{\varpi}\cos\psi-\frac{\gamma^2\rho h}{2}\frac{dv_{\rm p}^2}{d\ell}$$
$$-\rho c^2\frac{dh}{d\ell}-\frac{B_\phi}{4\pi\varpi}\frac{d\left(\varpi B_\phi\right)}{d\ell}=0. \tag{C.5}$$

In the above equation, forces terms[1] from left to right side are recognized as $F_{\rm GP\|}$, $F_{\rm G\phi\|}$, $F_{\rm T\|}$, $F_{\rm C\|}$, $F_{\rm I\|}$, $F_{\rm P\|}$, $F_{\rm B\|}$ and we can note that $F_{\rm E\|}=0$ along the poloidal direction.

The transfield equation is obtained from the equation (C.3) by taking dot product with $-\boldsymbol{\nabla}_{\rm s}A$ and we can write in term of forces like this (see Polko, 2013; Vlahakis *et al.*, 2003a),

$$F_{\rm G\perp}+F_{\rm T\perp}+F_{\rm C\perp}+F_{\rm I\perp}+F_{\rm P\perp}+F_{\rm E\perp}+F_{\rm B\perp}=0, \tag{C.6}$$

so these components of forces are perpendicular to poloidal field line and pointing along the axis $\hat{\mathbf{n}}=-\boldsymbol{\nabla}_{\rm s}A/\mid\boldsymbol{\nabla}_{\rm s}A\mid$. These perpendicular component of forces with common a factor $\frac{B_0^2\alpha^{F-2}}{4\pi\varpi G^4}$ are,

$$\begin{aligned}
F_{\rm G\perp} &= 0,\\
F_{\rm T\perp} &= 0,\\
F_{\rm C\perp} &= -\frac{x_{\rm A}^4\mu^2x^2}{F^2\sigma_{\rm M}^2M^2}\left(\frac{G^2-M^2-x^2}{1-M^2-x^2}\right)^2\sin(\psi),\\
F_{\rm I\perp} &= \frac{\sin(\theta)}{\cos(\psi+\theta)}\left[2M^2\sin^2(\theta)-M^2\frac{\sin(\theta)\cos(\theta)\sin(\psi+\theta)}{\cos(\psi+\theta)}\right.\\
&\quad \left.+M^2\frac{\sin(\psi)\sin(\theta)}{\cos(\psi+\theta)}-M^2\sin^2(\theta)(\frac{d\psi}{d\theta}+1)\right],\\
F_{\rm P\perp} &= \frac{\sin(\theta)}{\cos(\psi+\theta)}\frac{x^4}{F^2\sigma_{\rm M}^2}\left[-2(F-2)\frac{2\Theta h}{KM^2}-\frac{2\sin(\psi+\theta)\cos(\psi+\theta)\Theta h^2\Gamma}{hK-2\Theta\Gamma}\frac{1}{M^4}\frac{dM^2}{d\theta}\right],\\
F_{\rm E\perp} &= \frac{\sin(\theta)}{\cos(\psi+\theta)}\left[Fx^2\frac{\sin^2(\theta)}{\cos^2(\psi+\theta)}-x^2\frac{\cos(\psi)\sin(\theta)\sin(\psi+\theta)}{\cos^2(\psi+\theta)}-\frac{x^2\sin^2(\theta)}{\cos^2(\psi+\theta)}(\frac{d\psi}{d\theta}+1)\right],\\
F_{\rm B\perp} &= \frac{\sin(\theta)}{\cos(\psi+\theta)}\left(\frac{x_{\rm A}^4\mu^2x^2}{F^2\sigma_{\rm M}^2}\left(\frac{1-G^2}{1-M^2-x^2}\right)^2\left\{-(F-1)\right.\right.\\
&\quad \left.+\left[-\frac{1-M^2-x_{\rm A}^2}{1-G^2}\frac{dG^2}{d\theta}+\frac{dM^2}{d\theta}\right]\frac{\sin(\psi+\theta)\cos(\psi+\theta)}{1-M^2-x^2}\right\}\\
&\quad \left.+\left[-F\frac{\sin^2(\theta)}{\cos^2(\psi+\theta)}-\frac{\sin(\psi)\sin(\theta)}{\cos(\psi+\theta)}+\frac{\sin^2(\theta)}{\cos^2(\psi+\theta)}(\frac{d\psi}{d\theta}+1)\right]\right).
\end{aligned} \tag{C.7}$$

[1]The derivative is taken by keeping A and s as constant, $\frac{d}{d\ell}=\frac{\sin(\theta)\cos(\psi+\theta)}{\varpi}\frac{d}{d\theta}$

We simplify the equation (C.6) by using equation (5.16), has the form,

$$
\begin{aligned}
G\sin^2(\theta)\frac{d}{d\theta}\left[\tan(\theta+\psi)\frac{1-M^2-x^2}{G}\right] &= (F-1)\frac{x_{\rm A}^4\mu^2x^2}{F^2\sigma_{\rm M}^2}\left(\frac{1-G^2}{1-M^2-x^2}\right)^2 \\
&\quad -\sin^2(\theta)\left(\frac{M^2+Fx^2-F+1}{\cos^2(\theta+\psi)}\right) \\
&\quad -\frac{x_{\rm A}^4\mu^2x^2}{F^2\sigma_{\rm M}^2M^2}\left(\frac{G^2-M^2-x^2}{1-M^2-x^2}\right)^2 \\
&\quad +2\left(\frac{F-2}{F^2\sigma_{\rm M}^2}\right)\left(\frac{2\Theta hx^4}{KM^2}\right) \qquad \text{(C.8)}
\end{aligned}
$$

By following Vlahakis *et al.* (2003a), the slope of $M_{\rm A}^2$ at the Alfvén point *i.e.*, $p_{\rm A} = dM^2/d\theta|_{x_{\rm A}}$ and Bernoulli equation (C.1) at Alfvén point is given by,

$$
p_{\rm A} = dM^2/d\theta|_{x_{\rm A}} = \frac{2x_{\rm A}^2\cos(\psi_{\rm A})}{\sigma_{\rm A}\sin(\theta_{\rm A})\cos(\theta_{\rm A}+\psi_{\rm A})} \qquad \text{(C.9)}
$$

and

$$
\mu^2 = \left(h_{\rm A}^2 + \frac{F^2\sigma_{\rm M}^2(1-x_{\rm A}^2)^2\sin^2(\theta_{\rm A})}{x_{\rm A}^4\cos^2(\theta_{\rm A}+\psi_{\rm A})}\right)\times\left(\frac{x_{\rm A}^2(\sigma_{\rm A}+1)^2}{x_{\rm A}^2-[x_{\rm A}^2-\sigma_{\rm A}(1-x_{\rm A}^2)]^2}\right) \qquad \text{(C.10)}
$$

The Alfvén point condition is derived from equations (C.8) and (C.10) (see Appendix B in Vlahakis *et al.*, 2003a),

$$
\begin{aligned}
&\frac{F^2\sigma_{\rm M}^2(1-x_{\rm A}^2)(\sigma_{\rm A}+1)^2}{\mu^2\cos^2(\theta_{\rm A}+\psi_{\rm A})}\Bigg[-2(F-2)\frac{2\Theta_{\rm A}}{K}\frac{(1-x_{\rm A}^2)}{h_{\rm A}x_{\rm A}^2}\sin(\theta_{\rm A}) \\
&+\frac{2\cos(\psi_{\rm A})\sin(\theta_{\rm A}+\psi_{\rm A})(\sigma_{\rm A}+1)}{\sigma_{\rm A}}+\frac{\sin(\theta_{\rm A})}{x_{\rm A}^2}\left[(1-x_{\rm A}^2)(F-1)-1\right]\Bigg] = \left[x_{\rm A}^2-(1-x_{\rm A}^2)\sigma_{\rm A}\right]^2 \\
&-(F-1)\sigma_{\rm A}^2(1-x_{\rm A}^2)-2\left(\frac{F-2}{h_{\rm A}}\right)\left(\frac{2\Theta_{\rm A}}{K}\right)\left(x_{\rm A}^2-\left[x_{\rm A}^2-\sigma_{\rm A}(1-x_{\rm A}^2)\right]^2\right) \qquad \text{(C.11)}
\end{aligned}
$$

The coefficients of equation (5.16) are,

$$
\begin{aligned}
A_1 = \frac{\mu^2x_{\rm A}^6}{F^2\sigma_{\rm M}^2}\left(\frac{M^2}{G^2}\right)\frac{(1-G^2)^2}{(1-M^2-x^2)^3}\frac{\cos^3(\theta+\psi)}{\sin^2(\theta)\sin(\theta+\psi)}+\frac{M^2}{G^4}\frac{\cos(\theta+\psi)}{\sin(\theta+\psi)} \\
-\frac{x_{\rm A}^4}{F^2\sigma_{\rm M}^2}\frac{h^2}{M^2}\left(\frac{2\Gamma\Theta}{hK-2\Gamma\Theta}\right)\frac{\cos^3(\theta+\psi)}{\sin^2(\theta)\sin(\theta+\psi)}, \qquad \text{(C.12)}
\end{aligned}
$$

$$
B_1 = \frac{M^4}{G^4} \qquad \text{(C.13)}
$$

$$C_1 = \frac{h^2 x_{\rm A}^4}{F^2\sigma_{\rm M}^2}\frac{\cos(\psi)\cos^2(\theta+\psi)}{\sin^3(\theta)\sin(\theta+\psi)}\left\{\frac{\mu^2 G^4(1-M^2-x_{\rm A}^2)^2}{h^2G^4(1-M^2-x^2)^2}-1 + \frac{2x^2}{1-M^2-x^2}\frac{\mu^2}{h^2}\left[X-Y\right]\right\}. \tag{C.14}$$

Here

$$X = \frac{G^4(1-M^2-x_{\rm A}^2)^2 - x^2(G^2-M^2-x^2)^2}{G^4(1-M^2-x^2)^2}$$

$$Y = \frac{G^2(G^2-M^2-x^2)(1-M^2-x^2)(1-x_{\rm A}^2)}{G^4(1-M^2-x^2)^2}$$

The coefficients of transfield equation (C.8) after simplification using the expressions of A_1, B_1 and C_1,

$$A_2 = -\sin^2(\theta)\tan(\theta+\psi), \tag{C.15}$$

$$B_2 = \frac{\sin^2(\theta)(1-M^2-x^2)}{\cos^2(\theta+\psi)}, \tag{C.16}$$

$$C_2 = -\frac{\sin^2(\theta)(1-M^2-x^2)}{\cos^2(\theta+\psi)} + \sin^2(\theta)\tan(\theta+\psi)\left[x_{\rm A}^2\frac{dG^2}{d\theta} + (1-M^2-x^2)\frac{1}{G}\frac{dG}{d\theta}\right] + (F-1)\frac{x_{\rm A}^4\mu^2x^2}{F^2\sigma_{\rm M}^2}\left(\frac{1-G^2}{1-M^2-x^2}\right)^2 - \sin^2(\theta)\frac{M^2+Fx^2-F+1}{\cos^2(\theta+\psi)} - \frac{x_{\rm A}^4\mu^2x^2}{F^2\sigma_{\rm M}^2M^2}\left(\frac{G^2-M^2-x^2}{1-M^2-x^2}\right)^2 + 2\frac{F-2}{F^2\sigma_{\rm M}^2}\left(\frac{2\Theta h x^4}{KM^2}\right). \tag{C.17}$$

Bibliography

Abramowicz M. A., Czerny B., Lasota J. P., Szuszkiewicz E., 1988, *ApJ*, 332, 646.

Arlen, T. C., Vassilev, V. V., Weisgarber, T., Wakely, S. P., & Yusef Shafi, S., 2014, *ApJ*, 796, 18.

Asada, K., & Nakamura, M., 2012, *ApJ*, 745, L28.

Babcock, H. W., 1963, *ARA & A*, 1, 41.

Beck, R., 2009, *Astrophys. Space Sci. Trans.*, 5, 43.

Blandford, R. D., & Payne, D. G., 1982, *MNRAS*, 199, 883.

Blandford, R. D., & Znajek, R. L., 1977, *MNRAS*, 179, 443.

Bondi, H., 1952, *MNRAS*, 112, 195.

Bu De-Fu, *et al.*, 2016a, *ApJ*, 818, 83.

Bu De-Fu, *et al.*, 2016b, *ApJ*, 823, 90.

Bu De-Fu, Mosallanezhad A., 2018, *A&A*, 615, A35.

Busschaert, C., Falize, E., Michaut, C., Bonnet-Biadaud, J.M., Mouchet, M., 2015, *A&A*, 579 A, 25.

Camenzind M., 1986, *A&A*, 156, 137.

Camenzind M., 1986, *A&A*, 162, 32.

Camenzind, M., 1990, *Rev. Mod. Astron.*, 3, 234.

Camilo, F., Thorsett, S. E., Kulkarni, S. R., 1994, *ApJ*, 421, L15.

Ceccobello C. *et al.*, 2018, *MNRAS*, 473, 4417.

Chakrabarti S. K., 1989, *ApJ*, 347, 365.

Chandrasekhar, S., 1938, *An Introduction to the Study of Stellar Structure (NewYork, Dover).*

Chandrasekhar, S., 1956, *ApJ*, 124, 232.

Chattopadhyay, I., Chakrabarti, S. K., 2002, *MNRAS*, 333, 454.

Chattopadhyay, I., Chakrabarti, S. K., 2011, *Int. J. Mod. Phys. D*, 20, 1597.

Chattopadhyay, I., Ryu, D., 2009, *ApJ*, 694, 492.

Chattopadhyay, I., Kumar, R., 2016, *MNRAS*, 459, 3792.

Choudhuri, A. R., 1998, *The Physics of Fluids and Plasmas: an Introduction forAstrophysicists(Cambridge: Cambridge Univ. Press).*

Das, S., Chattopadhyay, I., 2008, *New. Astron.*, 13, 549.

de Gouveia Dal Pino, E. M., 2005, *AIP Conference Proceedings*, 784, 183.

Daly R. A., 2019, *preprint (arXiv:1905.11319).*

Dermer, C. D., Cavadini, M., Razzaque, S., *et al.*, 2011, *ApJ*, 733, L21.

Ferrario, L., Wickramasinghe, D. T., 2005, *MNRAS*, 356, 615.

Fukue, J., 1987, *PASJ*, 39, 309.

Ghosh, P., Lamb, F. K., 1977, *ApJ*, 217, 578.

Ghosh, P., Lamb, F. K., 1979, *ApJ*, 232, 259.

Gu Wei-Min, 2015, *ApJ*, 799, 71.

Hartmann, L., Hewett, R., & Calvet, N., 1994, *ApJ*, 426, 669.

Heinemann, M., Olbert, S., 1978, *J. Geophys. Res.*, 83, 2457.

Homan D. C., Attridge J. M., Wardle J. F. C., 2001, *ApJ*, 556, 113.

Icke V., 1980, *AJ*, 85, 239.

Karino, S., Kino, M., Miller, J. C., 2008, *ApJ*, 119, 739.

Kennel, C. F., Blandford, R. D., Coppi, P., 1989, *J. Plasma Physics*, rol. 42, part 2. pp. 299- 319.

Koldoba, A. V., Lovelace, R. V. E., Ustyugova, G. V., & Romanova, M. M., 2002, *AJ*, 123, 2019.

Kumar, R., Chattopadhyay, I., 2013, *MNRAS*, 430, 386.

Kumar, R., Chattopadhyay, I., 2014, *MNRAS*, 443, 3444.

Kumar, R., Chattopadhyay, I., 2017, *MNRAS*, 469, 4221.

Lamb, F. K., Pethick, C. J., Pines, D., 1973, *ApJ*, 184, 271L.

Lamb, F. K., Yu, W., 2005, *Binary Radio Pulsars ASP Conference Series*, Vol. 328.

Li, J., Wickramasinghe, D. T., Rudiger G., 1996, *ApJ*, 469, 765.

Li, J., Wilson, G., 1999, *ApJ*, 527, 910.

Li, Z.-Y., Chiueh, T., & Begelman, M. C., 1992, *ApJ*, 394, 459.

Liang, E. P. T., Thompson, K. A., 1980, *ApJ*, 240, 271.

Livio, M., 2001, *in ASP Conf. Ser. 224, Probing the Physics of Active GalacticNuclei by Multiwavelength Monitoring, ed. B. Peterson, R. Pogge, & R.Polidan (San Francisco: ASP)*, 225.

Lovelace, R. V. E., Mehanian, C., Mobarry, C. M., Sulkanen, M. E., 1986, *ApJ*, 62, 1.

Meliani, Z., Sauty, C., Tsinganos, K., Vlahakis, N., 2004, *A&A*, 425, 773.

Mestel, L., 1967, *Plasma Astrophysics, ed. Sturrock, P. A., Academic Press, New York.*

Mestel, L., 1968, *MNRAS*, 138, 359.

Michel, F. C., 1969, *ApJ*, 158, 727.

Mirabel, I.F., and Rodriguez, L. F., 1999, *Ann. Rev. Astron. Astrophys.*, 37, 409.

Mirabel, I.F., and Rodriguez, L. F., 2003, *Science* 300, 1119.

Mobarry, C. M., Lovelace, R. V. E., 1986, *ApJ*, 459, 3792.

Moller A., Sadowski A., 2015, *arXiv:* 1509.06644.

Muzerolle, J., Calvet, N., & Hartmann, L., 2001, *ApJ*, 550, 944.

Narayan, R., Kato, S., Honma, F., 1997, *ApJ*, 476, 49.

Nomura M., Ohsuga K., Takahashi H. R., Wada K., Yoshida T., 2016, *PASJ*, 68, 16.

Nomura M., Ohsuga K., 2017, *MNRAS*, 465, 2873.

Novikov I. D., Thorne K. S., 1973, *in Dewitt C., Dewitt B. S., eds, BlackHoles (Les Astres Occlus), Gordon and Breach, New York.* p. 343.

Paatz, G., Camenzind, M., 1996, *A&A*, 308, 77p.

Paczyński, B., Wiita, P. J., 1980, *A&A*, 88, 23.

Pan, Y. Zhang, C. Wang, N., 2013, *Proceedings of the International Astronomical Union, IAU Symposium*, 290, 291.

Parker, E. N., 1958, *ApJ*, 128, 664.

Polko, P., Meier, D. L., Markoff, S., 2010, *ApJ*, 723, 1343.

Polko P., Meier D. L., Markoff S., 2013, *MNRAS*, 428, 587.

Polko, P., 2013, *Exploring jet properties in magnetohydrodynamics with gravity , University of Amsterdam*.

Polko P., Meier D. L., Markoff S., 2014, *MNRAS*, 438, 959.

Priest, E., 2014, *Magnetohydrodynamics of the Sun(Cambridge: CambridgeUniv. Press)*.

Pringle, J.E., 1993, *in Astrophysical Jets (eds. D. Burgarella, M. Livio, M., and C. OĎea; Cambridge Univ.)*, p. 1.

Pringle, J. E., Rees, M. J., 1972, *A&A*, 21, 1.

Pudritz, R., Hardcastle, M. & Gabuzda, D., 2012, *Space Sci. Rev.*, 169, 27.

Rana, V. R., Singh, K. P., Barrett, P. E., Buckley D. A. H., 2005, *ApJ*, 625, 351.

Reipurth, B., and Bally, J., 2001, *Ann. Rev. Astron. Astrophys*, 39, 403.

Rothstein D. M., Lovelace R. V. E., 2008, *ApJ*, 677, 1221.

Sakurai, T., 1985, *A&A*, 152, 121.

Sakurai, T., 1987, *PASJ*, 39, 821.

Sarkar, S., Chattopadhyay I., 2019, *Int. J. Mod. Phys. D*, 28 (2), 1950037.

Saxton, C. J., Wu K., Pongracic H., Shaviv G., 1998, *MNRAS*, 299, 862.

Schmidt G. *et al.*, 2003, *ApJ*, 595, 1101.

Shakura, N. I., Sunyaev, R. A., 1973, *A&A*, 24, 337S.

Singh, K., Chattopadhyay, I., 2018, *JOAA*, 39:10.

Singh, K., Chattopadhyay, I., 2018, *MNRAS*, 476, 4123.

Singh, K., Chattopadhyay, I., 2019, *MNRAS*, 486, 3506.

Singh, K., Chattopadhyay, I., 2019, *MNRAS*, 488, 5713.

Synge, J. L., 1957, *The Relativistic Gas (Amsterdam: North-Holland)*.

Tajima Y., Fukue J., 1996, *PASJ*, 48, 529.

Tajima Y., Fukue J., 1998, *PASJ*, 50, 483.

Taub, A. H., 1948, *Phys. Rev.*, 74, 328.

Tsinganos, K. C., 1981, *ApJ*, 245, 764.

Tsinganos, K. C., 1982, *ApJ*, 252, 775.

Vlahakis, N., Konigl, A., 2003a, *ApJ*, 596, 1080.

Vlahakis, N., Konigl, A., 2003b, *ApJ*, 596, 1104.

Vyas, M. K., Chattopadhyay, I., 2019, *MNRAS*, 482, 4203.

Vyas, M. K., Kumar, R., Mandal, S., Chattopadhyay, I., 2015, *MNRAS*, 453, 2992.

Ustyugova, G. V., Koldoba, A. V., Romanova, M. M., Chechetkin, V. M., Lovelace, R. V. E., 1999, *ApJ*, 516, 221.

Weber, E. J.,Davis, L., Jr., 1967, *ApJ*, 148, 217-227.

Wardle J. F. C., Homan D. C., 2001, *in Laing R. A., Blundell K. M., eds, ASPConf. Ser. Vol. 250, Particles and Fields in Radio Galaxies ConferenceAstron. Soc. Pac., San Francisco*, p. 152.

Yang X.-H., Bu D.-F., Li Q.-X., 2018, *ApJ*, 867, 100.

Yuan F., *et al.*, 2015, *ApJ*, 804, 101.

Zamaninasab, M., Savolainen, T., Clausen-Brown, E., *et al.*, 2013, *MNRAS*, 436, 3341.